ABSTRACT

Title of dissertation: A PROTOTYPE MINIATURE MASS SPECTROMETER FOR IN SITU ANALYSIS OF TRACE ELEMENTS ON PLANETARY SURFACES

Benjamin J. Farcy, Doctor of Philosophy, 2021

Dissertation directed by: Professor Ricardo D. Arevalo Jr.
University of Maryland Department of Geology

Interrogation of the chemical composition of rocky planets provides a deeper understanding of the history and evolution of the solar system. While laboratory studies of returned samples and remote sensing surveys of planetary surfaces can give insight into planetary history, one technique that has delivered major insights to planetary geology is in situ measurements of a planetary surface via mass spectrometry. Here, a new approach to spaceflight mass spectrometry is discussed, including an overview of the pursued scientific questions, the analytes targeted, and the prototype hardware in development. This effort constitutes the scientific and technological foundation of a landed planetary mission.

This dissertation focuses on the history and evolution of the Earth-Moon system as recorded by trace elements. Specifically, the abundance and distribution of the heat producing elements (HPEs: K, Th, U) and their implications for mantle dynamics is considered. The radiogenic heat produced from K, Th, and U drives mantle convection, volcanism, and planetary dynamos. To understand better the chemical dynamics of radiogenic heat distribution in the Earth, the HPE abundance of a series of oceanic basalts was statistically analyzed. This analysis revealed the K/U ratio of the mantle and how it changes due to

the enrichment or depletion of incompatible elements. The HPE abundance of the lunar interior was also discussed as a target of a future investigation, along with a series of trace element proxies meant to probe the lunar farside mantle. Further, an analysis of lunar far-side craters provides a series of landing sites for an in situ mission, specifically for their surficial exposure of upper mantle material and later emplacement of lunar basalts.

To access the trace element systems discussed in this dissertation, a prototype miniature inductively coupled plasma mass spectrometer (ICPMS) was developed to analyze trace elements in situ for landed planetary missions. First, the capability of the plasma to atomize and ionize input material was investigated. A plasma operating at reduced pressure can achieve 99% ionization efficiency of most elements on the periodic table, with as much as a 50 to 100 times reduction in gas load and forward power compared to commercial systems for both He and Ar based plasma ion sources. The plasma system was integrated with a quadrupole mass spectrometer via a series of DC ion optics and vacuum housing, with its ion current and peak resolution optimized. Quantative data for an analyte spectrum of Kr demonstrates the ability for this instrument to resolve individual mass peaks, which lead to an accuracy and precision measurement of isotope ratios. This effort represents an end-to-end prototype miniature ICPMS, successfully demonstrating a viable instrument for landed planetary missions.

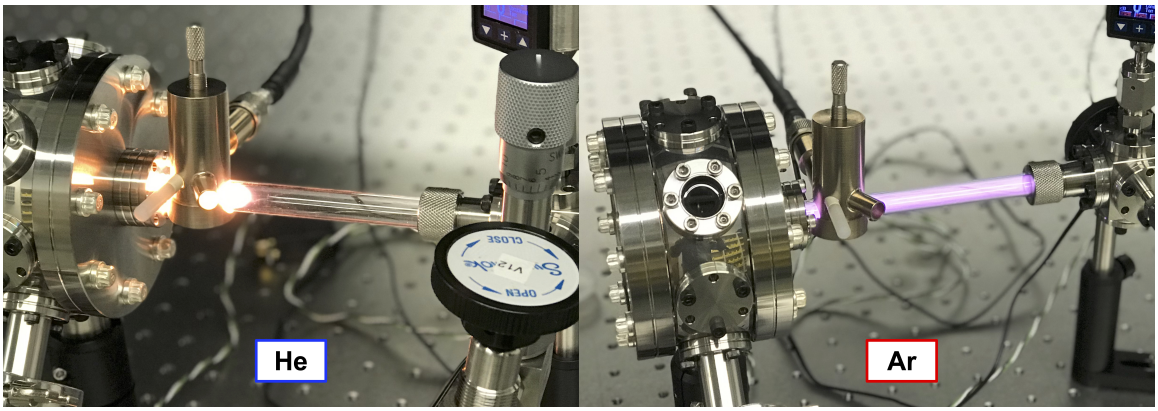

A PROTOTYPE MINIATURE MASS SPECTROMETER FOR IN SITU ANALYSIS OF TRACE ELEMENTS ON PLANETARY SURFACES

by

Benjamin J. Farcy

Dissertation submitted to the Faculty of the Graduate School of the
University of Maryland, College Park in partial fulfillment
of the requirements for the degree of
Doctor of Philosophy
2021

Advisory Committee:
Professor Ricardo D. Arevalo Jr., Chair/Advisor
Professor William F. McDonough, Co-Advisor
Professor Nicholas Schmerr
Dr. William Brinckerhoff

Preface

A majority of this document contains work that has been previously published in peer-reviewed journals. Chapters 2, 3, and 4 are all publications that are freely available via open access, and chapter 5 represents work that will be submitted for publication at a later date. While the author of this dissertation is the lead author of each publication, each chapter represents original work by me in collaboration with my colleagues.

Dedication

Dedicated to my parents, Leslie and Philippe, who have supported me in every endeavor I've ever attempted. Figuring out what you want out of life requires trying a lot of new things and sticking with the few things that speak to you, and you were always encouraging me to try something new. Science was one of those that you encouraged and supported me in, and it changed my life.

And dedicated to the most incredible, loving, and wonderful life partner a person could ask for, my wife Clare. Being able to share every triumph and victory with you, or having you pick me up during every struggle and low, was the biggest gift you could have given me. You got me through this process to the finish line, and it has been such a joy having you by my side at every step.

And to my high school environmental science teacher, Howie Hill. You first taught me to be in awe of nature, which is a gift I still hold to this day.

Acknowledgments

While the work put together here was my own, there are plenty of people who were instrumental (no pun intended) in helping me complete my Ph.D. Of course, I have to credit the constant, diligent, and hard work of the two most incredible advisors I could have asked for, Rick Arevalo and Bill McDonough. You guys have somehow managed to push me to levels I never knew were possible, while at the same time, giving me the latitude to work independently and make this project work on my own accord. You taught me to always pay attention to the details, while at the same time, never losing sight of the big picture. It's truly been a pleasure working with you two.

I would also like to thank Mazdak Taghioskoui for all of his guidance and technical skill. This was his vision from the beginning, and without the parts, knowledge, and guidance, the central portion that this dissertation hinges on would not have come together. I'd also like to thank my previous mentors from NASA Goddard, Andrej Grubisic, William Brinckerhoff, and Mehdi Benna, from whom I learned the hands-on skills needed to complete this work. Thanks to Richard Ash for his healthy and consistent skepticism, and to Tytrice Faison for helping me collect some of my data. And thanks also to the UMD geology staff, namely Michelle Montero for helping me navigate the bureaucracy of a Ph.D., and to Joanna Patterson to handling the constant influx of parts orders I generate.

A grad school experience is nothing without your fellow grad students who are working through the same things you are. I'd like to thank Lori Willhite, for being one of the smartest, kindest, and most talented scientists I've ever had the pleasure of working with. And thanks to the Grace Ni, whose skill and insight is always balanced by the whimsical joy she brings in every day. Thanks to Scott Whipperfurth for helping me through the first couple of years in grad school. Finally, I'd like to acknowledge Laura Sammon, Joe Golella, James Dottin, Sourabh Shubham, Ashley Hanna, and Soumya Ray. I'm a lucky man for getting to call you my colleagues and friends.

Table of Contents

List of Tables

List of plots

Chapter 1: Introduction

1.1 Overview and Scope of this Dissertation

The main goal of geochemistry is to understand better the geologic system at hand, whether it is on a local, regional, or planetary scale. Accomplishing this goal requires both the understanding of the processes that shape planetary surfaces and interiors, and the tools that can quantify the chemistry of a sample and deliver the necessary data. This dissertation is a combination of two separate efforts. The first is based in fundamental planetary science, seeking to understand the history and dynamics of Earth and the Moon through trace element systematics. The second effort is that of the toolmaker, involving the development of a new analytical technique through the miniaturization of an inductively coupled plasma mass spectrometer (ICPMS). These two fields of research form the framework of a landed planetary mission to the Moon, in which I have developed the hardware and the scientific justification for in situ chemical analysis of the lunar surface.

1.2 Defining Planetary Formation and Evolution with Trace Elements

The chemical composition of a rock records the terrestrial processes that produced it. Planetary scale processes, such as initial accretion from the solar nebula or differentiation into distinct reservoirs, or local and regional scale processes, such as magmatism or weathering, can drive sample composition to change over time. But because the high abundances

of major elements (i.e. $>$ 1 wt.%) control sample mineralogy, geological processes typically alter major element composition by a few percent. However, trace elements ($<$1,000 μg/g (parts per million, ppm)) can vary by much wider margins, up to 3 orders of magnitude in some terrestrial magmatic systems, acting as sensitive tracers to major processes. Here, a series of case studies demonstrates the use of trace elements for understanding planetary history. We discuss a series of geochemical systems and their applications to the Earth-Moon system.

1.2.1 Heat Producing Elements in the Bulk Silicate Earth

The heat that drives the Earth's mantle convection comes from two main sources: (1.) primordial heat from the initial accretion of the Earth, and (2.) radiogenic heat from the radioactive decay of the heat-producing elements (HPEs), namely K, Th, and U. The abundances of K, Th, and U in terrestrial reservoirs is influenced by their incompatibility, or their respective affinities for solid and liquid phases during melting or core formation. The HPEs are incompatible elements, so their abundances are higher in reservoirs that represent accumulation of low degrees of partial melting, such as the continental crust [90, 170]. HPE and other incompatible element abundances are depleted in the residual mantle reservoirs that have sourced these melts, leading to areas of enriched or depleted HPE reservoirs [12, 85]. Because mid-ocean ridge basalts (MORBs) are sourced from the upper mantle, the abundance of K, Th, and U in oceanic basalts can directly inform to their abundances throughout the Earth's interior.

One statistical method of estimating the abundance of an element in a reservoir is by using elemental ratios [84]. This method is robust because the ratios change little during geologic processing, contrary to larger variations in element absolute abundance. Considering Earth's HPE ratios, initial estimates of the ratio of potassium to uranium were $\sim 10^4$

[205], which is distinct from the K/U of CI chondrites of $\sim 8 \times 10^4$ [115]. Later studies suggest distinctions between the K/U ratios of major silicate reservoirs, such as the mantle, continental crust, and source region of ocean island basalts (OIBs) [10, 11, 65]. However, the overall K/U ratio of oceanic basalts and their mantle source regions requires further constraints.

In chapter 2 of this dissertation, I have produced an updated model for the abundance and distribution of HPEs in the bulk silicate Earth. The statistical modeling and analysis was performed on previously published K, Th, and U abundance values of MORB and OIB samples, leading to the estimated K/U ratio of the mantle sources of oceanic basalts.

1.2.2 Formation History of the Lunar Farside

The geologic history of the Moon has been inferred through geophysical and geochemical observations enabled by remote sensing, in situ seismic observations, and investigations of samples derived from its surface and interior. The observational techniques include orbital-based measurements of surficial composition using spectroscopy [158, 159, 215], and physical structures using gravitational surveys [207]. The composition of the Moon is also documented by meteorites derived from it [100], and samples returned from landed missions. These multi-faceted surveys of the lunar surface and interior have revealed lunar processes through time, shaping the local, regional, and global structure as it is observed today.

One main defining feature of the Moon that is evident from physical and chemical observations is a lunar global asymmetry. The lunar nearside and farsides are marked by a major structural and compositional dichotomies [79, 96, 98, 150, 174]. Observations of lunar crustal thickness indicate a farside lunar crust that is thicker than the nearside crust [207]. The farside crust is more Mg-rich (mafic) than the nearside crust, with a higher

Mg# (atomic Mg/(Mg+Fe)), and more mafic mineralogy. In contrast, the nearside crust is dominated by more felsic (feldspar and silica-rich), Fe-rich mineralogy [150]. The thinner, more felsic nearside crust has a significantly higher amount of mare basalt than the farside, implying more mantle melting than the nearside [79].

That the farside crust is thicker, compositionally more mafic, and has less surficial basaltic magmatism than the nearside, implies different formation or evolution histories between the two hemispheres. This hemispherical asymmetry implies different crystallization histories for their mantle regions, possibly due to an asymmetric distribution of HPEs [67, 103, 104]. As described in the previous section, the abundance and distribution of HPEs can have a major influence on planetary formation and subsequent processes, and possibly affected the crystallization sequence of each hemisphere of the lunar mantle.

In chapter 3, I outline the scientific case for sending an instrument capable of making in situ measurements of trace element abundances in lunar surface materials to understand the dichotomy between the two lunar hemispheres. I have identified which specific science questions would be addressed, which trace element systems could provide answers to these questions, and the performance needed from the instrument to access these geochemical proxies. Trace element systems as proxies for determining the pressure and temperature of basalt formation, the source mantle composition, and the chronology can be targeted. I outline a novel technology that is currently being developed to measure trace element abundances in situ. Finally, I carried out a landing site analysis of multiple lunar farside targets, identifying the lithologies that would be best suited for an in situ mission.

1.3 Inductively Coupled Plasma Mass Spectrometry for Trace Element Measurement

The analytical technique that has shown the most use and ubiquity in the field of trace element geochemistry has been inductively coupled plasma mass spectrometery (ICPMS), which relies on a high temperature plasma to break down material into its atomic constituents and ionize the atoms. ICPMS has seen a series of improvements over the previous decades, and the work outlined in chapters 4 and 5 will serve as a further change in the design and use of this well-established instrument.

The ICPMS consists of three main subsystems: (1.) The plasma ion source, (2.) the mass analyzer, and (3.) the detector. These three components work in tandem and together process input sample for analysis, allowing quantification of elemental abundances to low levels of detection. The plasma is energetic enough to process input samples for trace element quantification. After sample ionization, the ions are focused, separated by their mass to charge ratios (m/z) using electric or magnetic fields and detected as discrete electrical pulses. The ion detector at the end of the instrument uses either and integrated ion current converter or pulse counter to determine the final signal intensity at a given m/z value.

1.3.1 Spaceflight Mass Spectrometry

Analytical methods like mass spectrometry have been used for a wide range of applications in terrestrial laboratories for almost a century. While the laboratory can provide a controllable environment to produce high quality data, mass spectrometers have been ruggedized, miniaturized, and used for planetary science since the 1960s. Today, mass spectrometers have become indispensable payload instruments for planetary missions. Since the first mass spectrometer was sent into space, various mass spectrometers have been sent to over

a dozen locations throughout the solar system. The use of mass spectrometry in planetary science has led to new insights into the evolution of the solar system and planetary history [13].

While smaller in size, weight, and power, spaceflight mass spectrometers typically use the same fundamental design as laboratory-based instruments, containing an ion source, a mass analyzer, and a detector system. The combination of these three components will depend mainly on the analyte targeted and the abundance of that analyte. The architecture of instrument design during the recent era of planetary exploration has followed this logic, and the work described here is no different. In situ chemical analysis of planetary surfaces have been a mainstay of solar system exploration for decades, and novel analytical methods are needed to answer new questions in planetary science.

I have constructed a miniature ICPMS as a prototype of a spaceflight mass spectrometer. Chapter 4 focuses on the ionization capabilities of the low power plasma, in which I analyzed the fundamental characteristics of the plasma. These data were then used to calculate the ionization efficiency of the plasma, documenting its capability as an ion source for mass spectrometry.

Chapter 5 outlines the construction of an ICPMS instrument, carried out as a proof-of-concept with the goal of integrating a low power plasma ion source with a quadrupole mass analyzer, and demonstrating the ability to analyze input sample. This chapter includes designs for the vacuum housing, ion optics, and sample inlet system. It also includes calculations for chamber conductance to define the design of the differential pumping stages. Chamber construction was followed by a series of ion current optimization experiments to maximize the signal and tune the peak shapes, resulting in a mass spectrum of the ion beam. Finally, a sample was input into the newly constructed system in order to constrain empirically the accuracy, precision, and overall performance.

Chapter 2: K/U ratio of the MORB source and silicate Earth

Note: This chapter has been previously published at the following citation, and is currently available via open access:
Farcy, B., Arevalo Jr, R., & McDonough, W. F. (2020). K/U of the MORB Source and Silicate Earth. Journal of Geophysical Research: Solid Earth, 125(12), e2020JB020245.

2.1 Abstract

Potassium (K) informs on the radiogenic heat production, atmospheric composition, and volatile element depletion of the Earth and other planetary systems. Constraints on the abundance of K in the Earth, Moon, and other rocky bodies have historically hinged on K/U values measured in planetary materials, particularly comparisons of the continental crust and mid-ocean ridge basalts (MORBs), for developing compositional models of the bulk silicate Earth (BSE). However, a consensus on the most representative K/U value for global MORB remains elusive despite numerous studies. Here, we statistically analyze a critical compilation of MORB data to determine the K/U value of the MORB source. Covariations in the log-normal abundances of K and U establish that K is 3–7 times less incompatible than U during melting and/or crystallization processes, enabling inverse modeling to infer the K/U of the MORB source region. These comprehensive data have a mean K/U for global MORB = 13,900 $\pm$ 200 ($2\sigma_m$; n = 4,646), and define a MORB source region with a K/U between 14,000 and 15,500, depending on the modeled melting regime. However, this

range represents strictly a lower limit due to the undefined role of fractional crystallization in these samples and challenges preserving the signatures of depleted components in the MORB mantle source. This MORB source model, when combined with recent metadata analyses of ocean island basalt (OIB) and continental crust, suggests that the BSE has a K/U value >12,100 and contains $>260\times10^{-6}$ kg/kg K, resulting in a global production of $\sim$3.5TW of radiogenic heat today and 1.5×10^{17} kg of ^{40}Ar over the lifetime of the planet.

2.2 Introduction

Potassium (K) is a critical variable in compositional models for the Earth, Moon, and other planetary systems. The rarest isotope of K, ^{40}K (atomic abundance of 0.01167%), which follows a branched decay scheme to ^{40}Ca (89.44%) and ^{40}Ar (10.56%), provides radiogenic heat and produces atmospheric Ar, and ultimately prospects for habitability. As a lithophile element with minimal affinity for metallic iron [41] and an intermediate condensation temperature [114], the abundance of K in the silicate Earth largely defines the bulk planet's depletion in volatile elements relative to chondrites (e.g., [4]; [129]).

Despite the attention K attracts as a multifaceted geochemical proxy, the abundance of K in the silicate Earth, and by extension the bulk planet, remains poorly constrained. Abundances of refractory lithophile elements, such as La, Th, and U, in the bulk silicate Earth (BSE) may be inferred directly from chondritic relative abundances [31, 205], thereby enabling the abundance of K to be extrapolated through empirically observed ratios. Traditionally, the Earth's K content has been estimated from K/La, K/Th, and/or K/U values in terrestrial rocks. Because K, Th, and U are radioactive and concentrated in the crust due to their highly incompatible geochemical behaviors, we can measure K/Th and K/U on the surfaces of other rocky planetary bodies via gamma ray spectroscopy from orbit, enabling comparisons in volatile element depletions across the inner solar system ([157] and refer-

ences therein). The amount of ^{40}Ar in the BSE provides an independent validation on the inferred budget of K; for example, a minimum of 120×10^{-6} kg/kg K is needed to account for the 66×10^{15} kg of ^{40}Ar currently residing in the atmosphere [196]. In contrast, higher levels of K inferred in the BSE (e.g., $>200\times10^{-6}$ kg/kg, as predicted by several models described below) require a deep undegassed reservoir [3].

The earliest attempts to determine the amount of K in the BSE reported only limited variances in K/U measured between felsic and mafic rocks, with most K/U estimates for the BSE falling between 10,000 and 13,000 [95, 198, 205]; although some BSE models suggested K/U values up to 17,000 [31]. However, these findings were based on small sample collections. Later studies have added considerably larger amounts of data and uncovered measurable distinctions between K/U values, as recorded in rocks from the continental crust and oceanic basalts (e.g., [10, 107]). Perhaps more surprisingly, independent surveys that focused exclusively on mid-ocean ridge basalts (MORB) also show statistically significant K/U variations [10, 65, 94]. As a result, a wide range of K/U values for the BSE have been reported, resulting in anywhere from 120 $\times$ 10^{-6} kg/kg to more than 300 $\times$ 10^{-6} kg/kg K in the silicate Earth (assuming $\sim$2.8 CI1 chondrite abundances for the refractory elements; e.g., [129, 155]). The K/La ratio has also been employed to constrain the Earth's K content, given a relatively constant MORB K/La value of $\sim$330 [122, 155]. The problem with this approach is that the relative difference in the incompatibilities (as measured by partition coefficients) of K and La are greater than for K and U; consequently, relying on K/La correlations leads to skewed estimates of the K content of the BSE.

2.3 Attempts to constrain the K/U value of global MORB

Access to fresh samples from reliable curation facilities (e.g., Smithsonian Institute), streamlined acquisition of chemical analyses via *in situ* methods (e.g., laser ablation in-

ductively coupled plasma mass spectrometry, LA-ICPMS), and the emergence of publicly available online databases (e.g., PetDB) provide robust avenues to determine the K/U value for MORB. However, even with a growing number of analyses to interrogate, independent statistical evaluations of the same sample collection and/or data, compilations may derive different "representative" K/U values. For example, the application of means and standard deviations to describe a sample set assumes a normal distribution, which may not reflect the population. Although the distribution of K/U in MORB approximates a Gaussian curve (e.g., [94]), K and U abundances are skewed in mantle-derived materials (e.g., [9]), requiring that log-normal abundances be considered for traditional statistical treatments. Consequently, the composition of the MORB source may be (and has been) inferred from: i) the distribution of K/U values measured in each individual specimen; and/or, ii) log-normal distributions of K and U abundances. The former approach requires that both K and U be measured in each sample under investigation, potentially limiting the size of available data sets, but ensuring a uniform number of samples and an equal global distribution. The latter approach allows for decoupling between sample sets that characterize K and U distributions, supporting larger databases, but are at risk of unequal sample sizes, discrepant geographical coverage, and analytical biases, particularly the under-representation of samples depleted in U due to challenging detection limits and/or counting statistics.

Within the course of only a few years, several studies that attempted to determine a representative K/U value for the source of MORB arrived at statistically distinct answers, albeit through different approaches. [10] analyzed both K and U in a limited but global suite of MORB glasses (n = 75) by high-precision LA-ICPMS within a single laboratory (thereby eliminating the risk of inter-laboratory bias), indicating a mean K/U value $>$18,000 (Table 2.1). Depleted, or "normal-type" MORB (N-MORB; $[La/Sm]_n < 0.63$), were linked to higher K/U values than "enriched-type" MORB (E-MORB; $[La/Sm]_n \geq 0.63$), reflecting multiple source components with distinct compositions, and/or disparate partitioning

Table 2.1: Summary of K, U, and K/U statistics from previous studies

K/U Statistics	Arevalo et al. (2009)[a]	Jenner & O'Neill (2012)[b]	Gale et al. (2013)[c]
Minimum	10,700	5,800	1,600
Quartile 1	15,400	11,300	13,700
Median	18,500	13,800	16,200
Quartile 3	20,600	16,700	19,800
Maximum	43,400	34,400	43,500
Count	75	458	608
K/U Average	**18,300**	**14,000**	**17,000**
σ	4,800	4,000	5,600
$2\sigma_m$	1,100	400	500
Log-Normal Statistics	Arevalo et al. (2009)	Jenner & O'Neill (2012)	Gale et al. (2013)
K Average ($\times$ 10^{-6} kg/kg)	1,100	990	1,300
σ	200	110	100
Count	75	464	746
$2\sigma_m$	40	10	10
U Average ($\times$ 10^{-6} kg/kg)	0.061	0.078	0.087
σ	0.026	0.027	0.027
Count	75	491	693
$2\sigma_m$	0.006	0.002	0.002
K/U Average	**17,700**	**12,800**	**15,300**
σ	7,900	4,700	4,900
$2\sigma_m$	1,800	400	400

[a] Data reported for both "normal-type" and "enriched-type" MORB, as defined in the text.
[b] Data reported for all MORB samples derived from recognized spreading centers.
[c] Data reported for new (i.e. previously unpublished) MORB measurements provided in Gale et al. (2013)

behavior between K and U during mantle melting and fractional crystallization of basalts.

[94] measured the compositions (including both K and U) of more than 600 basaltic glasses collected from the ocean floor, including 497 MORB samples from recognized spreading centers, by similar high-precision LA-ICPMS techniques; these data support a MORB K/U value closer to 14,000 (Table 2.1). Although the variances in K/U determined by these two independent studies are nearly identical, an unpaired Welch's t-test, which conservatively assumes heteroscedasticity, indicates that these distributions are statistically distinct at the $>$99.9% confidence level.

[65] also characterized a limited collection of MORB, but they further combined these data with thousands of published measurements of K and U (including [94], but not limited to high-precision methods) from a global array of MORB glasses and whole rock samples compiled from the PetDB online database and unpublished data from multiple sources. Rather than treating the composite data set as a sub-sampling of a single population, [65] instead employed the data to estimate average compositions of 771 segments of the mid-ocean ridge network, relying on log-normal means to define representative abundances of highly incompatible trace elements, such as K and U. The spreading rate and length of each segment were used to define and apply a weight factor to each segment, leading [65] to argue for a global MORB K/U value closer to 12,000. Interestingly, the new data published in this study (n = 273, primarily from the Mid-Atlantic and Gakkel Ridges), which were collected by LA-ICPMS techniques, indicate: i) a substantively higher mean K/U value of 17,000 (table 2.1); and, ii) a distribution that is statistically indistinguishable from [10], as determined by an unpaired Welch's t-test at the $>$99.9% confidence level.

Although these studies attempted to solve the same problem objectively, variations between their respective compositional models highlight the importance of statistical data treatments as well as potential sources of error, including:

- analytical artifacts (e.g., systematic errors, different approaches in calibration strategy, and/or disproportionate characterization of more enriched samples due to instrument detection limits); and/or

- inequivalent geographical sampling (e.g., asymmetrical spatial coverage between samples with available K and U measurements).

Through a metadata analysis, in this study we attempt to circumvent controversial normalization schemes and weighting functions and simply rely on statistical variances to describe the uncertainties of global MORB chemistry. We explore potential links between

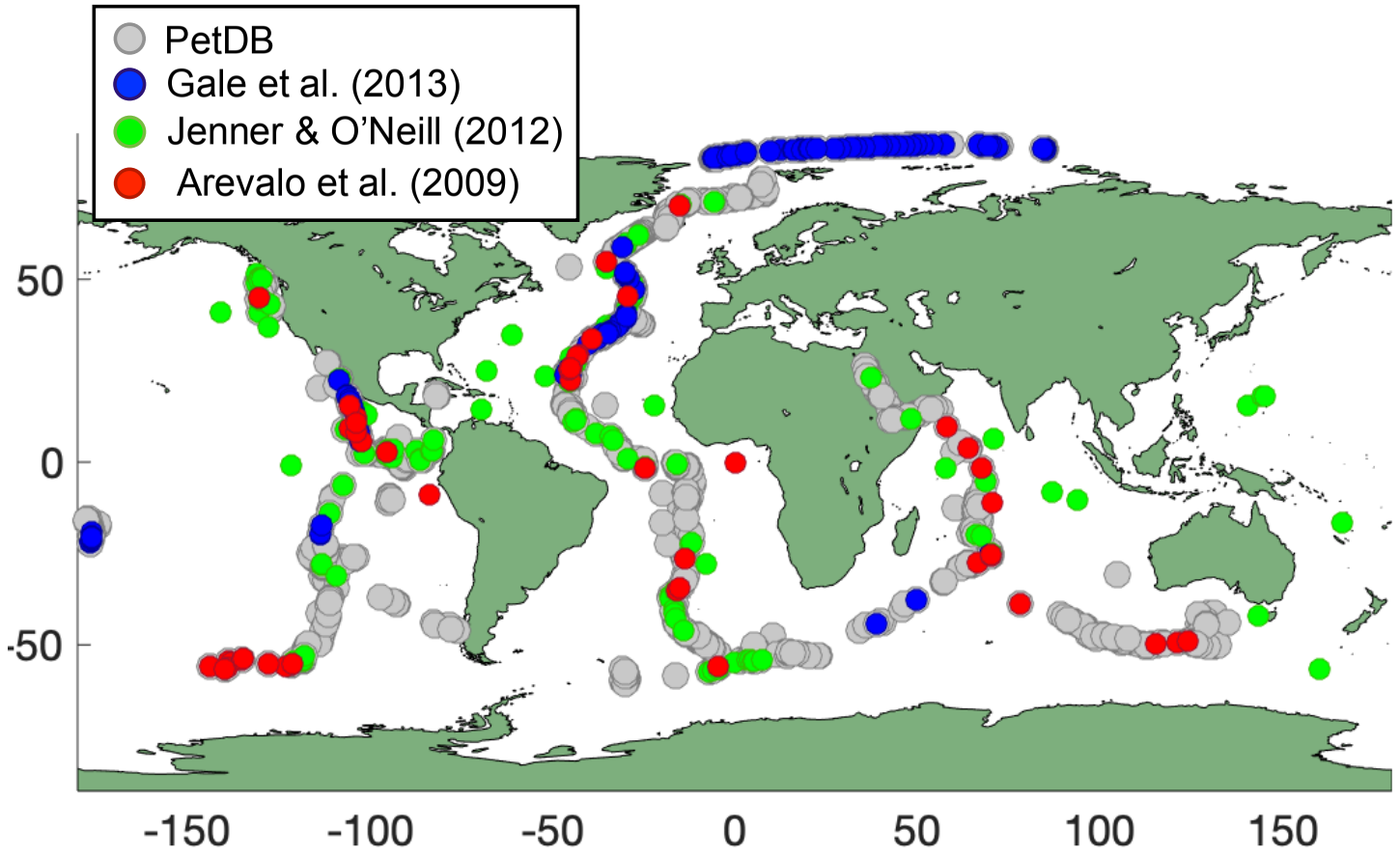

Fig. 2.1: Geographic distribution of MORB samples investigated here and in previous studies. Samples from [65] represent new analyses with both K and U measurements first published in that specific study.

K/U statistics and specific measurement techniques to evaluate critically analytical biases. To limit geographical inequalities, we focus only on samples that have been analyzed for both K and U. We also examine correlations between K/U and other geochemical indices that provide insights into distinct source contributions and partitioning behaviors. Fractionation between K and U is characterized quantitatively as a function of partial melting and/or crystallization processes to build a compositional model of the MORB source region, thereby enabling a reconstruction of the K/U value and K abundance of the BSE.

2.4 Data compilation and analytical methods

We compiled compositional data for $>$ 29,000 MORB samples from the PetDB database. The raw data were filtered to comprise samples with SiO_2 = 41 – 57% to reflect the IUGS classification of basaltic lithologies. Samples indicative of excessive olivine accumulation (i.e., MORB with MgO $>$ 16 wt.%) were extracted, and only samples with $Al_2O_3 < 18$ wt.% were included, encompassing the highest estimates of near-primary melt MgO and Al_2O_3 contents for MORB (e.g., [54]). Only samples with major element oxides summing to 100 $\pm$ 2% were admitted. Of this pared data set, only samples with both K and U measurements were considered in order to enforce an equal spatial distribution across the global ridge system. After applying these chemical filters, 4740 MORB sample analyses remained from the initial compilation. Aqueous alteration is not expected to affect the K/U results reported here because only analyses of fresh MORB glasses were considered, as demonstrated by a cohesive linear correlation between Th and fluid-mobile Ba (r^2 = 0.85) in the data set (see Appendix A).

2.5 A representative K/U value for global MORB

The MORB samples critically evaluated here are globally distributed (Fig. 2.1) and include 2877 glasses, 1545 whole rock samples, and 318 unlabeled rock types. Nearly all samples (n = 4713) have K abundances reported as K_2O, collected primarily via electron probe microanalysis (EPMA), and to a lesser extent x-ray fluorescence (XRF) and/or instrumental neutron activation analysis (INAA). However, 734 samples report K as a trace element (Table 2.2), measured almost exclusively by LA-ICPMS, supporting an investigation into putative biases in reported K abundances determined by different analytical techniques.

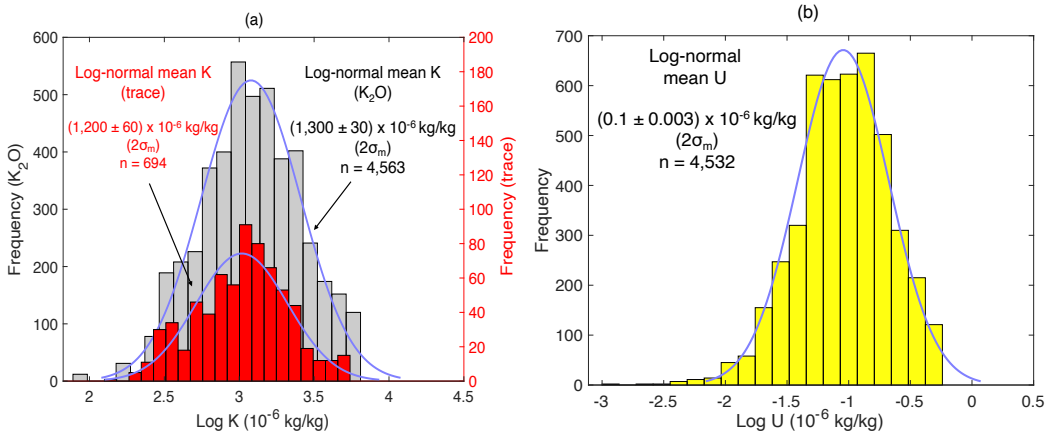

Fig. 2.2: Histograms of log-normal K and U abundances recorded in the MORB data set investigated here. (a) Comparison of log-normal distributions and statistics of K reported as K_2O and as a trace element, reflecting different analytical techniques. (b) Log-normal distribution of U.

Two independent log-normal distributions of K may be defined: 1) K determined as K_2O via EPMA, XRF, and/or INAA techniques; and, 2) K treated as a trace element and measured by LA-ICPMS. Because both distributions are Gaussian in shape (Fig. 2.2), parameterized statistical treatments may be applied. An unpaired t-test with unequal variance indicates that the means of the two distributions are statistically distinct (>99.9% confidence level), with the distribution of K measured as a trace element (via ICPMS) defined

Table 2.2: Statistics of K/U and log-normal K and U abundances determined by different analytical techniques

Statistics	K/U (K from K_2O)[a,b]	K/U (K as trace)[c]	K/U (synthesis)[d]	log K (K from K_2O)[b,e]	log K (K as trace)[c,e]	log K (synthesis)[d,e]	log U abundance[a]
Mean	**14,000**	**13,700**	**13,900**	**3.11**	**3.07**	**3.11**	**-1.00**
StDev	6,300	4,000	6,200	0.37	0.37	0.37	0.42
Count	4,616	733	4,646	4,713	734	4,740	4,732
$2\sigma_m$	200	300	200	0.01	0.03	0.01	0.01
Minimum	33	1300	33	1.92	2.16	1.92	-2.70
Quartile 1	10,000	11,000	10,000	2.87	2.83	2.87	-1.26
Median	13,300	13,700	13,300	3.10	3.07	3.10	-1.00
Quartile 3	17,200	16,300	17,000	3.34	3.27	3.34	-0.74
Maximum	39,400	30,000	39,400	4.60	4.52	4.60	0.55

[a]Outliers with values outside 3x the interquartile range were isolated from the statistical assessment.
[b]K measured as a major element (K_2O) primarily via EPMA, XRF, or INAA methods.
[c]K measured as a trace element almost exclusively via laser ablation ICPMS techniques
[d]Synthesis of K measurements, with trace element analyses treated as a default over major element analyses.
[e]No outliers fell outside 3x the interquartile range, thus no data points were isolated for statistical assessment

by a lower geometric mean.

Unfortunately, we cannot investigate analytical biases in the reported values of U because the specific techniques used to measure U in each sample are not provided. However, an unpaired t-test with unequal variance reveals that the distribution of K/U recorded by global MORB is insensitive to the method used to measure K. Thus, these findings fail to substantiate analytical biases as a root cause of conflicting K/U reported by previous surveys of MORB [10, 65, 94].

As inferred from K/U measured in each individual sample, the inclusive metadata compiled here indicate that global MORB are characterized by a mean K/U value of 13,900 $\pm$ 200 ($2\sigma_m$, Fig. 2.3), most closely aligned with the value previously reported by [94]. Alternatively, using the log normal K and U distributions from the same dataset, global MORB could arguably be represented by a K/U value of 12,800 $\pm$ 500 ($2\sigma_m$), approximating the model MORB composition based on the integration of ridge segment averages [65]. However, the drawbacks to the latter treatment, mainly unequal K and U sample sizes, discrepant geographical coverage, and analytical biases, are discussed above. Although geographical inequalities inevitably persist in MORB data sets due to incomplete and uneven sampling across the entire mid-ocean ridge network, sampling biases may be attenuated by focusing on samples with both K and U measurements (as demonstrated here). Nonetheless, these two distinct K/U values for MORB, derived from the same data set, highlight the sensitivity of statistical treatments to the construction of global compositional models.

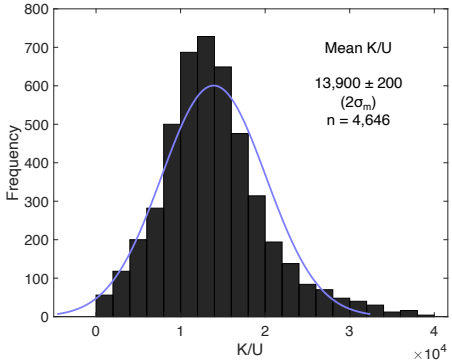

Fig. 2.3: Gaussian distribution of K/U values for the inclusive MORB data set (for samples with K reported as both K_2O and a trace element, the trace element abundance served as the default)

2.6 Fractionation of K and U during magmatic processing

The metadata evaluated here comprise 2961 enriched-type MORB (E-MORB; $[La/Sm]_n \geq 1.0$), 1535 normal-type MORB (N-MORB; $[La/Sm]_n < 1.0$), and 244 samples with unknown chemical enrichment/depletion due to insufficient rare Earth element (REE) analyses. A negative correlation between K/U and $[La/Sm]_n$ (see Appendix A) indicates that U is more incompatible than K during partial melting and/or fractional crystallization, corroborating observations reported previously (e.g., [180]; [77];[10]; [155]). Quantitative constraints on the partitioning behavior of these two elements (i.e., $D_U^{solid/liquid}$ versus $D_K^{solid/liquid}$) may be informed by a log–log co-variation diagram (e.g., [85]; [176]; [10]; [84]) if we assume that silicate differentiation is the primary control on K/U fractionation. Using this diagnostic approach, equal partitioning behavior between two elements would manifest as a slope of unity (m = 1.00). However, the role of different mass contributions from mantle sources with distinct compositions cannot be dismissed (e.g., more melt contribution for an enriched mantle source).

Bivariate linear regression analyses of the log-normal U (ordinate) versus K (abscissa) data presented here confirm that U is more incompatible than K; however, the exact slope (and by extension inferred magnitude of fractionation) is sensitive to the analytical technique used to measure K (Fig. 2.4). The regression best fit to the ICPMS data, which has a lower mean square weighted deviation (MSWD) than the regression for the complete data set, indicates a slope of 1.18 ± 0.04 (95% confidence) in agreement with previous evaluations [9]. Although the dynamics of MORB genesis are complicated by magma replenishment, mixing, extraction, and crystallization (amongst other processes; e.g., [153, 154] [152]), this quantitative log-log relationship can be used to infer $D_K^{solid/liquid}$ based on a given $D_U^{solid/liquid}$, which is more tightly constrained due to studies of Pb isotope systematics and U-series disequilibria. For more details on our calculation of D_K from log-log

regression, see Appendix A.

Here, we assume $D_U^{solid/liquid} = 0.001$, in line with partitioning experiments (e.g., [172]), natural observations of ultramafic systems [77], and previous literature compilations [213]. Given this assumption, if we treat the composition of the most depleted sample in the ICPMS data (i.e., lowest U abundance) as a proxy for the primary melt, and the most enriched sample (i.e., highest U abundance) as the last solid to crystallize, $D_K^{solid/liquid} \approx 0.007$, or $7 \times D_U^{solid/liquid}$, according to the bivariate linear regression. Similarly, if the most depleted sample approximates the composition of the mantle, consistent with a host of previous MORB source models (e.g., [11] and references therein), and the most enriched sample represents the smallest fractional melt of the source, $D_K^{solid/liquid} \approx 0.003$, or $3 \times D_U^{solid/liquid}$, according to the regression (see Appendix A). Although both of these scenarios are inherently oversimplified, such inverse models place quantitative bounds on the inferred $D_K^{solid/liquid}$ based on a statistical analysis of the empirical data set compiled here.

2.7 The K/U of the MORB source and bulk silicate Earth

The quantitative constraints on $D_K^{solid/liquid}$ provided here enable new insights into the K/U value of the MORB source region, and by extension the BSE. The comprehensive database compiled here (not limited to the ICPMS sample set) defines the mean K/U value of global MORB as 13,900 $\pm$ 200 ($2\sigma_m$; Table 2.2). As with the derivation of $D_K^{solid/liquid}$, we need to consider the type(s) of differentiation process(es) involved in the genesis of MORB in order to model the fractionation of K/U between source and melt. For example, if the bulk of the population of MORB samples evaluated here represent 8–20% equilibrium melting of the source, and assuming $D_U^{solid/liquid} \sim 0.001$ and $D_K^{solid/liquid} \sim 0.003$–$0.007$, the mean K/U value of the MORB source region falls between 14,000 and 15,500. Alter-

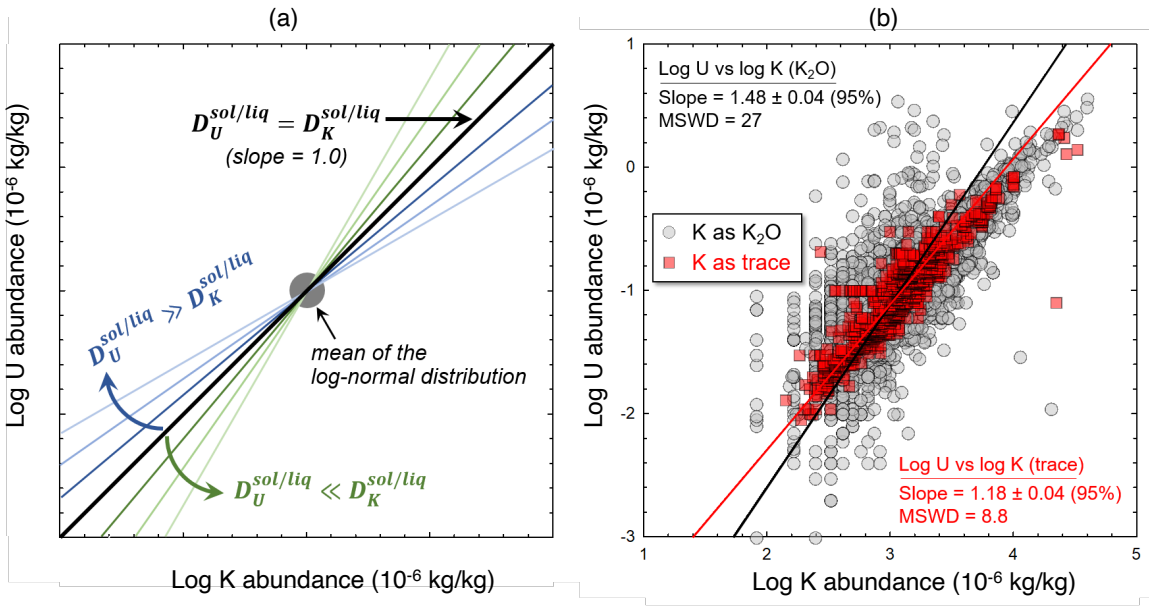

Fig. 2.4: (a) Schematic showing the effect of unequal element incompatibility on the slope of log-log regression analyses. (b) Log-log bivariate linear regressions for K and U abundances, with K measured as an oxide (multiple techniques) compared with K measured as a trace element (primarily via LA-ICPMS) in the data set compiled here. Regression slopes for both sets of data are distinct from 1, indicating an unequal incompatibility between K and U.

natively, models of mantle melts derived from an equivalent range of 8–20% of fractional melting, as opposed to equilibrium melting, would attenuate K/U fractionation, implying a mean MORB source with a K/U value between 14,000 and 14,200. Considering most samples in the compilation have less than 10 wt.% MgO, they have also experienced significant fractional crystallization, which would require an even higher K/U of the MORB source than what is estimated from inverse modeling of low degree melting alone. Equilibrium and fractional melting models and data on K/U fractionation due to fractional crystallization are found in Appendix A.

Although the K/U value of the MORB source is thus shown to be model dependent, the empirical data compiled here highlight that the MORB source region must be characterized by a K/U value higher than that preserved in the global MORB population. Further, because melts derived from the most depleted source components contributing to MORB genesis

are unequivocally overprinted by more enriched domains (e.g., [179]), the K/U value of the composite MORB source likely falls even higher than these simple model calculations suggest. If the enriched domains in the MORB source contain a higher proportion of pyroxenite [214], which has a lower solidus than peridotite (e.g., [131]), they may be preferentially melted at mid-ocean ridges and thus introduce a sampling bias [83], further implicating a higher source K/U value than that defined by global MORB. Nonetheless, the range of MORB source compositions defined here may be used to corroborate previous studies (e.g., [94]) and contradict the higher [10] and lower values proposed by others (e.g., [95]; [65]).

To evaluate how the MORB source model constrained here impacts the inferred heat production and noble gas budget of the BSE, we need to consider other appreciable sources of K and U; in the simplest scenario, the silicate Earth may be reconstructed by the MORB source, the source(s) of ocean island basalts (OIB), and the continental crust. A global compilation of OIB [11], including samples representing "endmembers" defined by extreme radiogenic isotope signatures (e.g., [216]), shows that OIB samples exhibit a significant variance in K/U. In particular, samples from Gough (mean K/U = 18,900 $\pm$ 1800, $2\sigma_m$; n = 23) and Society (mean K/U = 7200 $\pm$ 400, $2\sigma_m$; n = 12) represent the highest and lowest K/U values of this data set, respectively. Taken together, this inclusive OIB data set implies a mean OIB K/U value = 11,000 $\pm$ 500 ($2\sigma_m$; n = 322). Although OIB derive from intraplate volcanic centers and thus reflect melting conditions distinct from MORB, trace element systematics suggest that K is similarly less incompatible than U during the genesis of OIB (e.g., [180]; [9]); therefore, the mean OIB source region should be modeled with a K/U value $>$ 11,000.

Historically, compositional estimates of the bulk continental crust have suggested a K/U value between 7700 [189] and 15,900 [66]; however, a more recent synthesis of these models coupled with a progressive evaluation of new empirical constraints have resulted

in a preferred K/U value of 11,600 for the continental crust ([169] and references therein). Thus, the MORB source is defined by a markedly higher K/U value than both global OIB and the bulk continental crust.

If we combine the K/U values for the MORB and OIB sources and the continental crust, weighted according to the mass fraction of U proposed for each domain (e.g., [11]; [169]; and references therein), the preferred mean K/U value for the BSE falls around 12,100 (assuming a chondritic bulk Earth). Of course, this again represents a lower limit for the silicate Earth, given the potential for chemical overprinting [179], distinct source mineralogies [214], and melt sampling biases [83], resulting in difficulties in characterizing the most depleted components of MORB and OIB sources [179]. Nonetheless, assuming 20×10^{-9} kg/kg U in the bulk silicate Earth [129], this K/U value suggests $>260 \times 10^{-6}$ kg/kg K in the BSE, indicating $\sim$3.5 TW of radiogenic heat production from K today (10% lower than previous estimates; [10]), contributing to 20 TW of total radiogenic power produced globally. This K content would produce 1.5×10^{17} kg of ^{40}Ar over the lifetime of the planet.

Chapter 3: Understanding the Lunar Nearside–Farside Dichotomy via In Situ Trace Element Measurements: The Scientific Framework of a Prospective Landed Mission

Note: This chapter has been previously published at the following citation, and is currently available via open access:
Farcy, B., Arevalo, R., McDonough, W. F. (2021). Understanding the Lunar Nearside–Farside Dichotomy via In Situ Trace Element Measurements: The Scientific Framework of a Prospective Landed Mission. The Planetary Science Journal, 2(2), 80.

3.1 Abstract

Trace elements, distinguished by their low abundances (parts per million by weight (ppmw) track local, regional, and planetary scale processes in samples sourced from throughout the Solar System. Such analyses of lunar samples have provided insights on its surface rocks and interpretations of its deep interior. However, returned samples, sourced from the lunar nearside, cannot be used to address processes responsible for the morphological dichotomy between the lunar nearside and farside. This hemispherical dichotomy points to distinct evolutionary histories of these two domains, rendering our understanding of lunar history as incomplete. We outline the scientific justification for a landed, in situ investigation of lunar farside lithologies, focusing on chemical analyses that will constrain the Moon's bi-hemispherical chemical evolution. Newly developed and heritage spaceflight

instruments, capable of measuring low element abundances (limits of detection $<$10 ppmw $\pm$20%) can be deployed on the lunar farside and provide constraints on: (1) the temperature and pressure of mare basalt crystallization, (2) depth dependent mineralogical and compositional changes in the lunar mantle, (3) the chronology of major geologic events, and (4) abundances and distributions of refractory and heat producing element abundance of the lunar farside mantle. The science return and logistical challenges of targeting four specific landing sites on the lunar farside are identified: Moscoviense, Apollo, Von Kármán, and Leibnitz craters. These sites maximize impact melt basin lithologies and later mare magmatism, and minimize terrain hazards.

3.2 Introduction

The chemistry of the Moon holds the key to understanding the early history of the Earth-Moon system, as well as the sequence of formative events in the timelines of other planetary objects. In particular, the composition of the lunar interior provides a window into the chemical and isotopic fractionation provoked by the Moon-forming event. The Moon's surface additionally informs on the dynamics of lunar differentiation, calibrates crater counting chronologies, and provides access to mission-enabling resources. Thus, exploration of the lunar crust and mantle-derived materials is important to constraining the evolution of the Earth-Moon system and supporting human exploration objectives. The Planetary Science Decadal Survey 2013 – 2022 (NRC, 2011) and Lunar Exploration Roadmap (LEAG, 2016) highlight the need to characterize the stratigraphy and structure of the Moon as a means to resolve the initial conditions of solar system formation and inform on the accretion, differentiation, and impact history of the inner planets.

The bulk compositions of the inner solar system can be described to $>$90% with only four elements, namely Fe, O, Mg, and Si, which govern the primary mineralogies of these

bodies. In contrast, trace element abundances (<1000 ppmw, parts per million by weight) are not "buffered" by sample mineralogy; rather, distributions of trace elements are controlled by mineral-melt partitioning behaviors that reflect the temperature, pressure, and redox conditions of the system. Consequently, trace element abundances can vary by orders of magnitude in cogenetic geological samples, and serve as sensitive tracers of planetary processes.

Here we provide details of a potential lunar landed missions that can deliver key chemical and isotopic information, giving insights into lunar stratigraphy, chronology, and differentiation. We outline the scientific justification for such a mission in which heritage or developing spaceflight analytical techniques can be used to determine the absolute and relative abundances of a wide range of trace elements and isotopic systems. Our landing site recommendations focus on lunar farside targets, as these would be best suited to deliver the greatest scientific returns.

3.3 Science Objectives

The morphological and lithological dichotomy between the lunar nearside and farside is well documented [79, 96, 98, 150, 174], implying distinct formation histories of the crust and mantle of each hemisphere. Further constraints are needed to understand better the composition and formational history of the lunar farside, and thus the Moon as a whole. Models explaining the crystallization sequence of the Lunar Magma Ocean (LMO) depend on accurate predictions of the temperature and composition of the crystallizing liquid, which has robust constraints from nearside sampling, but little information for the farside. Here, we identify measurements that will constrain (1) the temperature and pressure of formation of farside mare basalts, (2) the mineralogical composition of the lunar farside mantle, (3) the chronology of major geologic events in the Moon's past, and (4)

the refractory element enrichment and volatile element depletion of the bulk Moon relative to the Earth. A landed in situ investigation is propsed to make these measurements, as orbital-based instrumentation can only measure the distribution of major and trace elements on a regional scale, hemispherical source locations of lunar meteorites are not well established, and return samples from Apollo and Luna missions sample only the nearside, biasing our view of lunar evolution. Taken together, the four science objectives described here will help define the temperature-dependent crystallization sequence of the LMO for farside mantle material, and provide further compositional and temporal constraints for its subsequent melt products.

3.3.1 Temperature and Pressure of Mare Basalt Formation

Crystallization of the LMO leads to a characteristic stratigraphy of cumulate mineralogy, defining a bottom-up petrologic evolution to the lunar mantle [53]. However, the Moon likely formed with an asymmetric distribution of heat producing elements [67, 103, 104], possibly leading to a different crystallization sequence on the lunar farside [52]. Because of this thermal asymmetry, the temperatures and pressures at which mare basalts melt and crystallize are likely different for farside basalts than for nearside basalts, leading to petrologic differences between melt products from the two hemispheres. Here, we outline analyses that will help constrain the temperature and depth of farside mare basalt formation in order to better understand farside lunar mantle petrology and global heat distribution.

Estimates of the depth and temperature of source region melting are based on analyses of returned mare basalts and picritic glasses, both of which are derived from isotopically distinct source regions [184, 185]. Whereas mare sources are modeled with minimum melting depths of 100-250 km [120], picritic glasses indicate melting depths from 360-520 km in a garnet-bearing lithology, possibly forming below the depth of LMO cumulate forma-

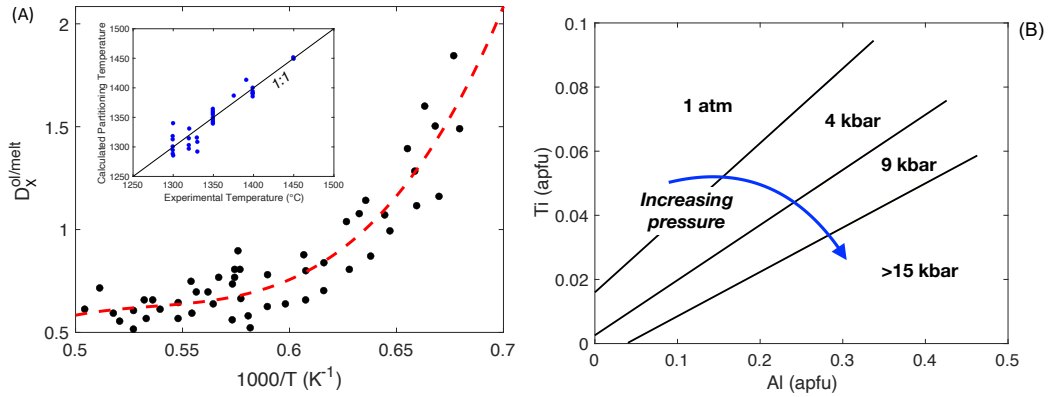

Fig. 3.1: (A) Example of calibrated geothermometer, using the temperature-sensitive partitioning of a given element between two phases during controlled melting experiments. In situ measurements of specific elements occurring in a given mineral and matrix can be used to estimate the temperature of melting. Inset shows an example calibration between controlled experimental temperature and temperature derived from a partitioning-based geothermometer. Figure modified from [45], with inset figure modified from [200]. (B) Geobarometer calibrated using pressure-sensitive partitioning of Al and Ti in clinopyroxene, calibrated via controlled high pressure experiments from [144]. Measurements of Al and Ti in pyroxene grains from mare basalts can be used to constrain the depth of the mantle source of melts. Al and Ti abundance calculated as atoms per formula unit (apfu).

tion and instead sampling primitive unmelted lunar mantle material [49, 117, 120, 140, 175]. Picritic glasses also likely form at greater temperature, with melting temperatures estimated at 1,410 - 1,500 ^{o}C as compared to 1,200 - 1,380 ^{o}C for mare basalts [118, 120]. Despite constraints on the temperature and pressure of melt generation from the lunar nearside, similar estimates are lacking for the farside. Temperature and pressure estimates from farside mare basalts can help constrain the farside mantle solidus, and by extension farside mineralogy and petrology, enabling comparisons to compositional models of the lunar nearside. Key measurements of trace element abundances can provide an indirect gauge of the temperature profile of the lunar farside mantle.

Crystallization temperatures and pressures can be inferred through the observed distribution of specific trace elements between two (or more) phases, calculated as $D_X^{phase1/phase2} = \frac{C_1}{C_2}$, where $D_X^{phase1/phase2}$ is the partition coefficient of element X, which is sensitive to temperature and/or pressure, and C_1 and C_2 are the element concentration in each phase.

Geothermometers are commonly calibrated via controlled high temperature and pressure melting experiments, in which synthetic oxide mixtures or natural basalts are melted at varying temperatures and the partitioning of temperature-sensitive elements is measured between phases as a function of experimental temperature. For example, the temperature-sensitive partitioning of Al and Cr between olivine, Cr-spinel, and melt [40, 48], Mg# in olivine [82], Ni between olivine and melt, [168, 201], and Na_2O between clinopyroxene and melt [161, 162], can all be used as indirect gauges of crystallization or equilibration temperature (Fig. 3.1A). These thermometers can be applied to a variety of mantle-derived lithologies (e.g. kimberlites, mantle xenoliths, and basaltic mantle melts) from across a range of compositions and temperatures (e.g. olivine Fo# 89-93, T = 750 – 1450 °C).

Measurements of crystallization pressure can produce a depth profile of lunar mantle melting, revealing changes in composition and temperature as a function of depth. Pyroxene can serve as an example of a geobarometer, and can be used to infer local pressure of melt systems. As elements with 3+ cation charges substitute for 2+ cations in the M1 site of the mineral, lattice strain theory predicts that this site becomes smaller at high pressure. Al is more likely to be accepted into the mineral than Ti due to its smaller ionic radius (Al^{3+} = 67.5 pm, Ti^{3+} = 81 pm) thus allowing less Ti into the site and lowering the Ti/Al ratio at higher pressure. Thus, the Ti/Al ratio in pyroxenes can be used to measure the pressure of sample crystallization. This barometer has been calibrated by [142] and [61] from atmospheric pressure to $>$ 1.5 GPa (Fig. 3.1B), and has been applied to Martian shergottites [37, 144].

The trace elements targeted for this investigation occur over a range of abundances in lunar and terrestrial rocks, so instrumentation with a large dynamic range is needed to carry out these analyses. For the Earth, the range of olivine-mineral equilibration temperatures produces olivine Al and Cr abundances of tens of ppmw. This is in contrast to the more efficient partitioning of Ni in olivine, which can yield concentrations as high as 3,500 ppmw

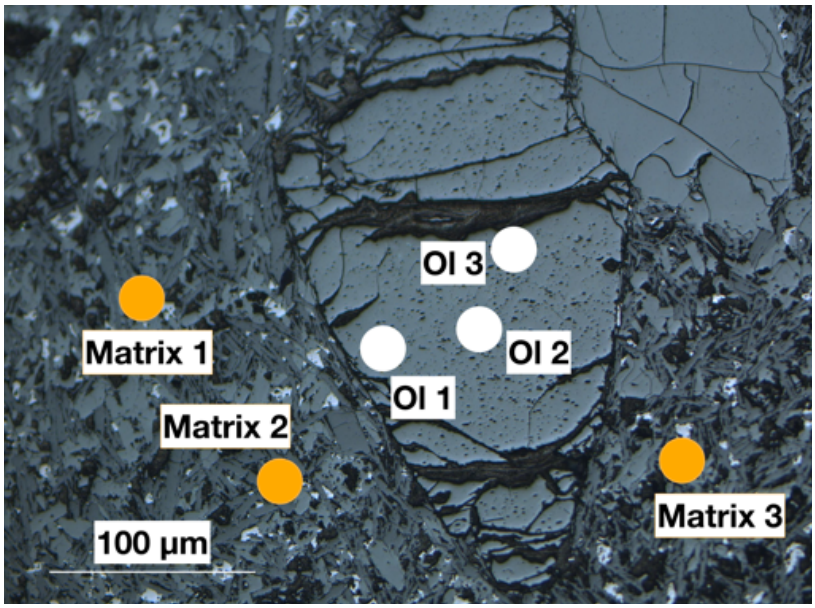

Fig. 3.2: Olivine phenocryst in fine-grained matrix in basalt from St. Helena island. White and orange dots show example measurement spots needed to calculate partitioning ($D_X^{ol/melt}$) value. Photo taken using JEOL 8900R electron probe microanalyzer at the University of Maryland, College Park

[177], although lunar bulk rock and olivine Ni abundances are typically $<$ 200 ppmw and $<$ 600 ppmw, respectively [121, 173]. An in situ analysis would require measurements of specific trace elements (e.g. Ni, Cr, or Al) in multiple phases in the sample (e.g. Fig. 3.2). Therefore, spaceflight instrumentation designed for trace element measurement with a range of limits of detection and high-resolution optical cameras for mineral-specific analyses could provide access to these proxies.

3.3.2 Lunar Mantle Mineralogy

Trace element systematics of returned lunar basalts and glasses help constrain the mineralogy and composition of the lunar nearside mantle. The LMO crystallization sequence and subsequent mantle overturn event produced a mixed stratigraphy of cumulate ultramafic minerals and oxides in the lunar mantle, which is sampled by magmatism. Samples of nearside mare basalts and glasses show a mantle source that is likely pyroxenitic to

lhzerolitic in composition, with composition becoming more mafic with increasing depth. Heavy REE abundances in picritic glasses also indicate the possibility of sampling undifferentiated, garnet-bearing "primitive" lunar material [140] at greater depth. The change in mantle composition as a function of depth is further supported by geophysical evidence from the Apollo seismic network, which indicates a pyroxenitic upper mantle from 238 - 488 km and and ultramafic lower mantle $<$ 488 km, with increasing Mg# with depth [64].

The trace element content of the mantle source regions reveals the extent of geochemical processing as well. Low-Ti basalts are depleted in incompatible elements, and contain chondritic ratios of refractory elements (e.g. Zr/Hf, Nb/Ta), while high-Ti basalts contain non-chondritic ratios and incompatible element enrichments [140]. This indicates that source differentiation likely lead to separate chondritic and non-chondritic upper mantle sources [206]. But while the composition of mare and picritic glasses provide constraints on their respective source regions, similar constraints for the lunar farside mantle are needed. If the lunar mantle cumulate overturn event was caused by the buildup of high density oxide phases, and an asymmetric distribution of heat caused a heterogeneous mantle crystallization, then the cumulate overturn event may have proceeded differently on the farside compared to the nearside.

During mantle melting, certain trace element ratios fractionate little relative to each other due to their similar partition coefficients, and instead retain the trace element ratios of the mantle sources. For example, concentrations and ratios of first row transition elements (FRTEs) in mantle-derived materials (e.g., basalts) can be used to infer the ratio of olivine to pyroxene in their respective mantle sources [109]. For the Earth, whole rock Ni/Co ratios $<$ 6 indicate a pyroxenitic mantle source, while Zn/Fe ($\times$10,000) ratios $<$ 12 and Mn/Fe ($\times$100) ratios $>$ 1.4 indicate melting of peridotite sources (Fig. 3.3). In addition to whole rock abundances, source lithology can further be inferred using FRTE ratios in specific minerals (e.g. olivine, pyroxenes). Ni, Mn, and Ca partitioning between

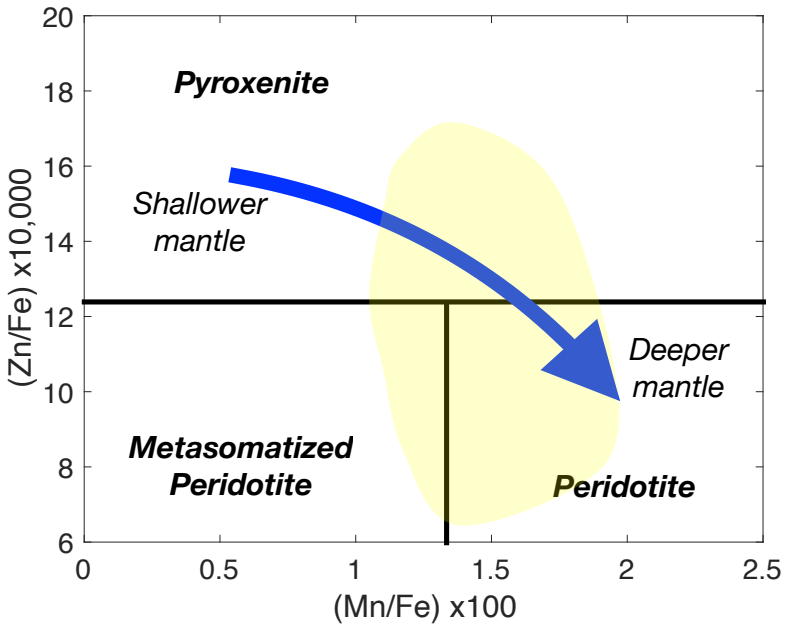

Fig. 3.3: Example of first row transition element (FRTE) ratios being used to estimate mantle source composition. Yellow area represents range of values for ocean island basalts (OIB). Figure modified from [109]

olivine is controlled by the extent of peridotite or pyroxenite melting, and correlates with long lived radiogenic isotopes (e.g. Sr, Nd, Pb, [73, 127]). Ratios of Ge to FRTEs or other elements can be an important indicator of source composition, due to the different partitioning behavior of Ge between peridotite and pyroxenite during partial melting ($D_{Ge}^{ol/melt}$ = 0.42, $D_{Ge}^{cpx/melt}$ = 0.87, [45, 78]). Analysis of MORB and OIB samples suggests Ge/Si ratios $> 7.5\times10^{-6}$ are common for peridotite mantle sources with minimal pyroxenitic influence, while ratios $< 6\times10^{-6}$ are indicative of the addition of pyroxenite to the mantle source [214]. Ge can also be leveraged as Ge can also be leveraged as an indicator of source lithology using the Ga/Ge ratio, as differences in this ratio are observed between MORB and Hawaiian OIB, reflecting differences in mantle source composition [8]. Ge is also an indicator of mantle metasomatism in the Moon, as higher abundances of Ge are typically found in conjunction with fluid-mobile volatile elements [50].

Measurements of FRTE ratios, such as Zn/Fe, Mn/Zn, Co/Fe, or Ni/Co, as well as

Ge/Si or Ga/Ge, can deliver insight into the relative proportion of peridotite and pyroxenite in the farside mantle. The FRTEs discussed here occur in lunar basalts in abundances of 1 ppmw to hundreds of ppmw, although Ge ranges from 1 ppbw to 1 ppmw, which could prove challenging for future analyses [204]. While the framework to determine source composition through FRTE ratios has been established for the terrestrial mantle, further modeling and empirical observations are required to apply these ratios to lunar samples. For example, the Zn/Fe ($\times$10,000) ratio typically ranges from 4-20 in MORB samples, while this ratio is typically $<$1 in lunar mare basalts, likely due to the volatile depletion of Zn in the BSM. Regardless, these proxies can be leveraged to estimate lunar mantle mineralogy from common surficial mare basalt flows. The analyses proposed here, in conjunction with estimates of pressure and temperature, will act as a petrologic cross section of the lunar mantle, revealing changes in lunar farside mantle composition with depth.

3.3.3 Geochronology

Chronology of major geologic events throughout the solar system is a critical aspect of our understanding of planetary formation, history, and evolution. Significant effort has been employed to constrain the timing of major events in lunar history, such as the initial formation of the Moon, LMO crystallization and differentiation, and the history of impact cratering. Chronological constraints have traditionally been placed on these events by radiometric age determination via long-lived radioisotopes (e.g. Rb-Sr, U-Pb, Sm-Nd, K-Ar) in returned samples and meteorites, or by crater counting statistics. However, sampling bias from the nearside and large uncertainties associated with crater counting chronology make accurate timing of global lunar events difficult.

Constraints on early lunar history are derived from geochronology of returned lunar material. U-Pb and Hf-W isotope systematics of lunar and terrestrial samples indicate a

	Thermobarometry	Source Mineralogy	Geochronology	Refractory/Volatile + HPEs
Elements to be measured	Al, Cr, Ni, Mg, Ti, Na	Ca, Ni, Co, Mn, Fe, Zn, Ga, Ge	K, Ar, Rb, Sr	K, Th, U, Al, Ca, Zn, Li
Minerals target for analyses	Olivine, clinopyroxene, ± spinel oxide	Olivine, clinopyroxene, orthopyroxene, bulk rock	bulk rock, multiple phases	Bulk Rock
Range of abundances	10^1 ppm (Al in olivine) to wt.% (Mg)	10^2 ppbw (Ge) to 10^3 ppmw (Ni)	10^1 - 10^2 ppmw (Rb + Sr) to wt.% (K)	10^2 - 10^3 ppb (Th and U) to wt.% (K, Al, Ca)
Landing site lithology targeted	Basalt flow	Basalt flow	Impact melt, basalt flow	Impact melt

Table 3.1: Summary of elements, geologic phases, and abundances targeted for trace element analysis in the investigations prioritized here.

Moon-forming impact age of 4.50 – 4.51 Ga, implying early lunar formation [15, 125, 192], while other estimates also using U-Pb ages in zircons derived from lunar breccias place the age of the impactor later at ∼4.42 Ga [38, 128, 145]. Rb-Sr and Sm-Nd isotope systematics of samples representing the latest stages of LMO crystallization indicate that Mg-suite, ferroan anorthosite, urKREEP, and a mare basalt source formed concordantly with each other at ∼4.35 Ga within a 40 Myr span, indicating a common reservoir source for those samples [18, 19]. These ages of late LMO crystallization are concordant with the ∼4.34 Ga age determined from meteorite MIL 13317, which is possibly derived from the lunar farside [43]. These U-Pb age constraints have been used in conjunction with thermals models of LMO crystallization, and indicate that the final 10% of highly-enriched KREEP material possibly existed in its molten state for 100-200 Myr due to an insulating anorthositic crust and high concentration of heat producing elements [128, 145]. Thus, geochronology of returned samples outlines the sequence of events from lunar impact origin to LMO crystallization.

Despite the constraints discussed here, lunar crustal formation possibly proceeded asymmetrically between the farside and nearside due to the thermal difference between hemispheres during LMO crystallization, leading to differences in the timing of farside crust and mantle formation. The farside crust likely crystallized first due to the lower temperature of the farside magma ocean, forming greater amounts of anorthositic material from a more mafic melt [7]. This is supported by orbital-based measurements of farside anorthosite, which is thicker [151, 207], and more Mg-rich [42, 149] than nearside anorthositic crustal material. Because of the nearside sampling bias and uncertainties associated with crater counting statistics, our understanding of the chronology of farside crust and mantle crystallization, and thus of the LMO as a whole, is limited. Here, we discuss chronological constraints on samples representing lunar farside LMO crystallization, anorthositic crust formation, and early magmatism. In situ geochronology measurements can provide a more

complete picture of the formation of the two lunar hemispheres.

In situ geochronology can be carried out using radioactive isotope parent/daughter ratios, mainly Rb-Sr and K-Ar. K-Ar systematics are a useful tool for lunar chronometry and history, due to its sensitivity to impact events, surficial exposure, and solar wind implantation. However, a main issue in measuring these isotopes through mass spectrometry is borne from the overlapping mass peak from ^{87}Rb on ^{87}Sr. To circumvent this challenge, steps are typically taken to separate the signals from the two isotopes either by signal correction or through physical separation of Rb from Sr. This isotope system has been used extensively to identify distinctions in terrestrial sources of MORB and OIBs, as well as planetary material from the Moon, Mars, and chondritic meteorites.

In situ measurements of K, Ar, Rb, and Sr in samples representing late-stage LMO cumulates could be targeted to make chronological constraints analogous to those previously discussed. Data from the Clementine and Kaguya-GRS missions show K dabundances on the lunar surface as high as 1-2 wt.% in the nearside mare deposits, with 600-1,100 ppmw K in the SPA basin and 100-250 ppmw in the anorthositic highlands [68, 215]. Measurements of the ^{87}Rb/^{86}Sr and ^{87}Sr/^{86}Sr ratios are more accessible to terrestrial and spaceflight analytical techniques than other geochronometers (e.g. U-Pb), Sr exist in typical lunar and terrestrial rocks in abundances from tens to hundreds of ppmw as opposed to ppbw-level concentrations. However, Rb abundances in lunar rocks are typically between 1-40 ppmw due to the depleted nature of moderately volatile elements in the BSM [204].

In addition to the previous discussion, in situ geochronlolgy on the lunar farside can constrain the timing and flux rate of the period referred to as the late heavy bombardment (LHB), with implications for the cratering history of the early solar system and the emergence of life on Earth. A discussion of this history is beyond the scope of this paper, for more information on in situ geochronology for the LHB, see [34], this issue.

3.3.4 Refractory and Volatile Element Content of the Moon

The compositions of terrestrial planets depend on their source materials, as well as the processes associated with accretion, including (but not limited to) incomplete condensation and evaporative loss of volatile elements. Planetary formation processes could have resulted in the enrichment of refractory elements and depletion in moderately volatile elements (elements with half mass condensation temperature of $<$1,250 K at 10^2 Pa). Mass balance estimates of the composition of the silicate portion of the Moon reveal a possible enrichment in refractory lithophile elements (e.g. Ca, Al, Th, U) by a factor of up to 1.5$\times$ relative to the bulk silicate Earth [64, 102, 136, 188, 190]. However, others suggest no such enrichment, resulting in terrestrial absolute abundances of refractory lithophile elements in the BSM [119, 186, 202, 203]. The Moon also is depleted in volatile and moderately volatile elements, (e.g. K, Li, Rb, Zn), relative to the Earth, leaving even more uncertainty in BSM abundance and distribution of lithophile elements [26, 44, 46, 97, 212]. This depletion of volatiles has major implications for the lunar thermal history, as the relative and absolute abundances of K, Th, and U, the heat producing elements, in the BSM are partially controlled by their volatility.

The estimates of lunar refractory and volatile element abundances are based on analyses of returned samples, meteorites, and oribital-based measurements of the lunar surface. Due to the nearside sampling bias of returned samples and the limitations of orbital-based measurements (e.g. limits of detection, large spatial scale, sampling depth), our understanding of the relative or absolute abundances of refractory and volatile element abundances requires more constraints. Here, we discuss measurements proposed to better constrain the refractory and volatile element abundances in the lunar farside mantle.

Element volatility in the Moon controls the abundance of the heat producing elements: K, Th, and U (K is volatile, Th and U are refractory). The K/U and K/Th ratio, derived from

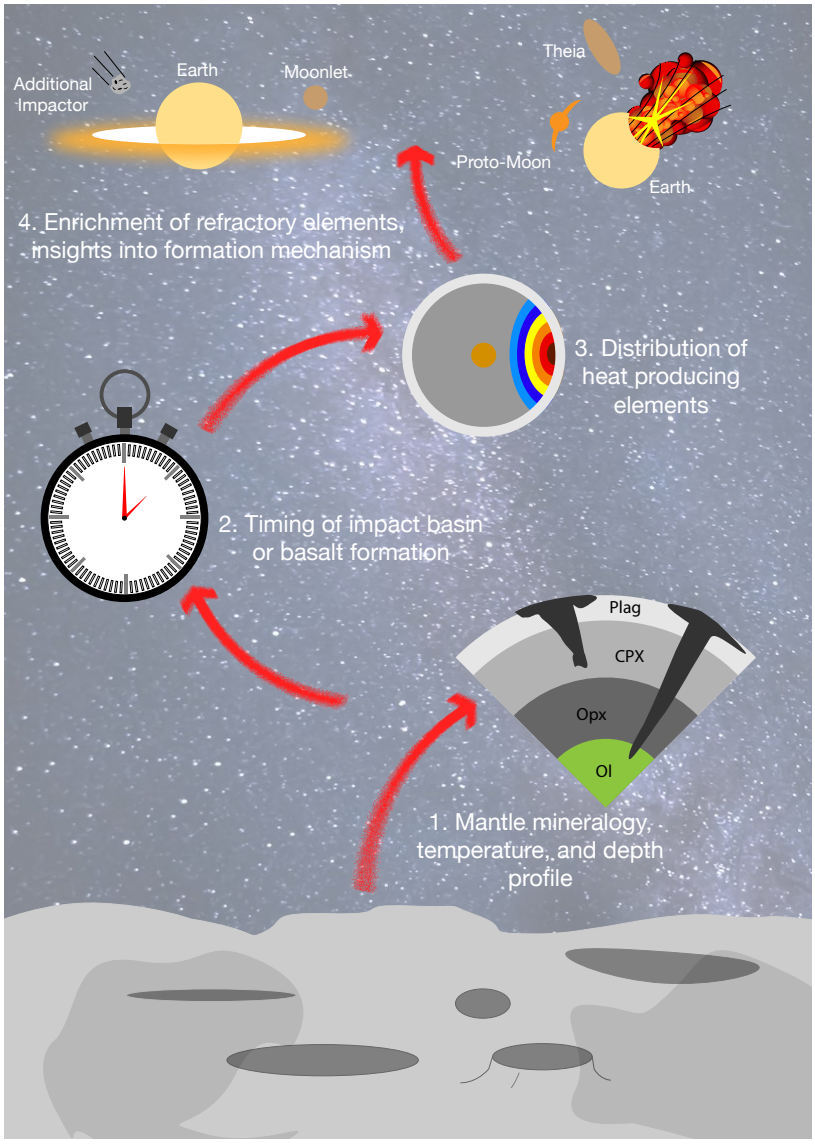

Fig. 3.4: Cartoon diagram of science objectives for a landed farside lunar mission, with a focus on trace element geochemistry. Measurements of FRTE ratios and partition coefficients of temperature and pressure-sensitive elements (e.g. Ni) between mineral phases in basaltic melts can provide insight into the formation history and composition of the farside mantle source region. K-Ar and Rb-Sr radiometric systems can then be used to estimate the timing of mare basalt emplacement and impact melt events. Determining refractory element abundances of impact melts will help constrain the farside mantle abundance of heat producing elements, giving insight into the thermal evolution of the lunar farside and formation mechanisms of the Moon.

lunar samples and γ-ray spectroscopy measurements of the surface, indicate a lunar K/U of 1,500 – 3,000 [74, 178, 187] and K/Th of 360-460 [103, 160]. This is significantly lower than terrestrial (K/U = 14,000 $\pm$ 1300, K/Th = 3,000 $\pm$ 750) and chondritic (K/U = 66,000 $\pm$ 5,000, K/Th = 18,000 $\pm$ 1,200) values [12, 56, 115, 130]. The K/U ratio fractionates, albiet slightly, due to magmatic processing [9, 12, 56, 107]. Thus, if the lunar farside mantle evolved with a different crystallization sequence than the nearside, then ratios of HPEs may be fractionated in the lunar farside mantle relative to the nearside.

The distribution of heat producing elements within the lunar interior may also be asymmetric between the nearside and farside, as uneven crystallization of the LMO and tidally-driven gravitational harmonics possibly trapped HPE-rich liquid preferentially on the nearside [67]. An asymmetric distribution of HPEs would lead to uneven heating of the lunar interior, driving mare volcanism preferentially on the nearside and altering the late-stage crystallization of the cumulate mantle [103, 104]. The asymmetric distribution of HPEs is evident on the surface via orbital-based γ-ray spectroscopy, although further analyses are required to constrain this asymmetry for mantle material in addition to surficial deposits. Therefore, more information is needed about the HPE absolute abundance, distribution, and relative enrichment/depletion in the lunar farside mantle.

Measuring the HPE relative and absolute abundance in the lunar farside interior would require instrumentation capable of measuring a wide range of elemental concentrations. K is typically found on the lunar surface in abundances from hundreds of ppmw to 1-2 wt.%, and Th and U are observed in hundreds of ppbw to low ppmw abundances [160], although the absolute abundance in the lunar mantle may be as low as $<$10 ppbw. A landed mission would likely require the ability to measure K, Th, and U at low limits of detection, smaller spatial scales, and greater surface depth. Further, analyses of HPEs should preferably be carried out on surficial deposits that are reflective of the lunar farside mantle. Specifically, large-scale impacts produce basins that melt and homogenize the upper mantle, exposing

upper mantle material to the surface. Farside basins that contain norite and troctolite impact melts are thought to be representative of the lunar upper mantle and would be ideal targets for the measurements proposed here [91].

Here, we have identified a series of chemical analyses of minor and trace elements in the surface materials of the lunar farside in order to better characterize lunar formation history and evolution. These measurements, taken together, are designed to constrain the formation mechanism and composition of the bulk Moon, the thermal distribution of the farside, a compositional depth profile of the lunar farside mantle, and the timing of major geologic events. These measurements can collectively produce a geologic cross section of the lunar farside mantle, with the added context of initial chemistry and time. While the analyses outlined here would collect data critical to our understanding of lunar history, in situ trace element analyses is not limited to these four proxies. Instead, analyses of trace elements can provide significantly more insights into lunar mantle processes and history than what has been outlined.

3.4 Instrumentation for chemical analysis

The physical characteristics of the elements, such as their mass or spectroscopic emission patterns, have been historically exploited to detect and quantify the composition of geologic material from orbit or ground-based facilities. Analytical techniques developed for terrestrial labs continue to be miniaturized, enabling new applications for trace element measurements for planetary exploration. Here, we provide an overview the various techniques previously applied to major and trace element characterization of planetary environments, as well as novel developments of future in situ detection techniques.

3.4.1 Spaceflight-Heritage Instrumentation

Landed missions extending as far back as the Viking era have enabled in situ elemental analyses of planetary surface materials. One of the most common analytical techniques, flown on a range of missions from the Viking landers [16] to the Curiosity rover [123], is pyrolysis gas chromatography mass spectrometry (pyr/GCMS). This method, which will also be exploited by the Mars Organic Molecule Analyzer (MOMA) onboard the ExoMars Rosalind Franklin Rover [69], provides access to volatile elements and organic compounds, particularly those associated with minerals that breakdown at temperatures $\leq$900 °C (e.g., phyllosilicates). To measure minor and trace elements specifically, the payloads of the Viking 1 and 2 landers also included X-ray fluorescence spectrometers with detection limits below 100 ppmw for select elements (e.g., Rb and Sr), albeit with significant analytical uncertainties [30]. XRF instrumentation has also characterized the composition of the surface of Venus via Venera 13 [182], and other sites on Mars via Curiosity [17]; a micro-XRF instrument also launched recently onboard the Mars 2020 rover [5].

Continuing with the exploration of Mars as a case study for technology development, the Mars Exploration Rovers, Spirit and Opportunity, incorporated miniaturized thermal emission spectrometers to characterize local mineralogy, and Mossbauer spectrometers to specifically identify iron-bearing phases. To access low abundance trace elements, Spirit and Opportunity also carried an Alpha Particle X-Ray Spectrometer (APXS; [166]), similar to previous versions operated on the Moon via Surveyors 5 – 7 [156] and on Mars Pathfinder [62], and more recent iterations flown on Curiosity [25] and Rosetta's Philae lander [99]. The detection limits of alpha particle scattering extend below 100 ppmw for some elements, comparable to XRF techniques.

ChemCam, a Laser Induced Breakdown Spectrometer (LIBS) onboard Curiosity, enables spatially-resolved minor and trace element measurements at standoff distances up

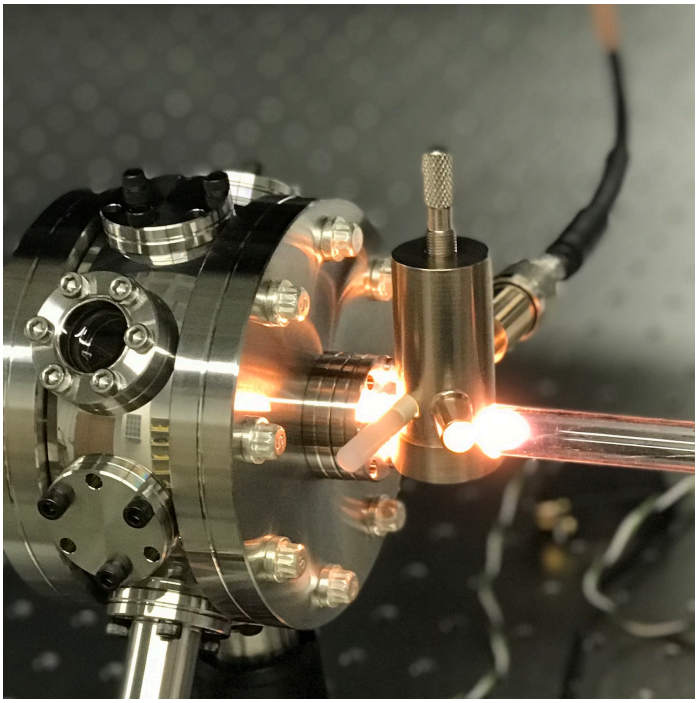

Fig. 3.5: Photo of low power He plasma, generated at 14 W of power and 200 mL/min of gas flow, developed at the University of Maryland, College Park.

to 7 m away from the source [210]; an analogous LIBS instrument augmented to support remote Raman spectroscopy was recently launched onboard the Mars 2020 rover [209]. Such LIBS techniques promise detection limits as low as $<$100 ppmw for many alkali and alkaline earth metals [208]. Onboard the Rosalind Franklin rover, the MOMA instrument's laser desorption/ionization mode can also determine the elemental chemistry of martian materials with fine spatial resolution, but analyses are limited to samples that are physically collected by the rover, and detection limits have yet to be defined for minor and trace elements.

3.4.2 Developing Technology

Significant time and research dollars have been invested to develop advanced in situ analytical techniques for emerging planetary science objectives. Novel technologies de-

signed to achieve enhanced performance metrics, such as lower limits of detection, and/or reduce resource requirements, such as power consumption, may enable measurements of trace element abundances and isotopic ratios previously considered inaccessible for landed missions. Particular interest has centered on the advancement of instrumentation capable of establishing chronological constraints via K-Ar and Rb-Sr radiometric dating. The K-Ar Laser Experiment (KArLE) uses a LIBS instrument to measure the K abundance of a sample, and a quadrupole mass analyzer to determine the absolute amount of radiogenic ^{40}Ar released during laser processing [35]; the analysis of other noble gas isotopes, including ^{36,38}Ar and ^{20,21,22}Ne, provide constraints on exposure ages [57]. The Rb-Sr isotope system can be accessed through the Chemistry, Organics, and Dating EXperiment (CODEX), which relies on multiple laser systems that generate light at specific wavelengths to resonantly desorb and ionize Rb and Sr separately, avoiding the isobaric interference between 87Rb and 87Sr during mass analysis [6]. Both of these investigations have demonstrated the ability to meet or exceed the NASA goal of determining absolute ages of planetary materials with a minimum precision better than $\pm 5\%$ (2σ; 2015 ROADMAP).

The progressive development of high-powered laser systems and a variety of mass analyzers that can be interfaced to such sources indicates that chemical imaging of trace elements and isotopic ratios is within the reach of near-term mission opportunities. Laser desorption/ablation mass spectrometry techniques, as enabled by miniaturized instruments that have a direct path to a spaceflight, have been shown to deliver 2D chemical maps of planetary analog samples [146], 3D depth profiles of solid substrates [71], and contemporaneous measurements of organic compounds and their host matrix [14]. However, in the laboratory, inductively coupled plasma mass spectrometer (ICPMS) systems serve as the gold standard for measuring trace and ultratrace element abundances down to sub-ppbw levels in natural samples. A commercial ICPMS typically requires between 1200 – 1600 W and 14-18 L/min Ar gas to generate a high temperature plasma that effectively atomizes

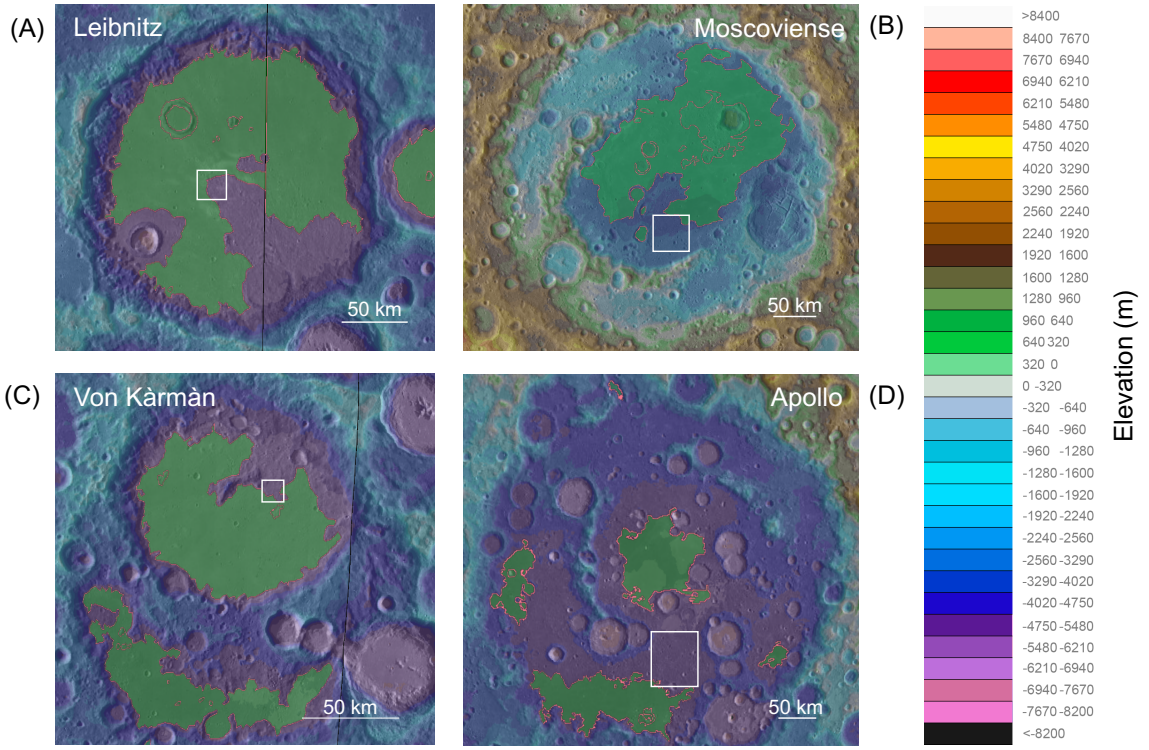

Fig. 3.6: Composite maps of four potential landing sites selected at (A) Leibnitz, (B) Moscoviense, (C) Von Kármán, and (D) Apollo craters. Images compiled using *LRO Quickmap* mapping tool, with topography data overlay from the LRO LOLA instrument and topography scalebar to the right. Locations of mare basalt units are infilled with green, and the area targeted as the primary landing site marked by a white square.

and ionizes geologic materials introduced by laser ablation (e.g., [148]). However, recent work has demonstrated the feasibility of using less power (<25 W) and reduced gas flow rates (<0.2 L/min) to produce a plasma capable of atomizing and ionizing geologic material at similar efficiencies to a commercial instrument (Fig. 3.5; [55]), albeit with higher detection limits due to a limited capacity to support mass loading. Thus, in the near future emerging technologies may enable measurements of trace elements and isotopic systems with lower detection thresholds, higher precision/accuracy, and spatially-resolved sampling to further support the science objectives outlined in this work.

3.5 Landing Site Analysis

The goal of the proposed investigation is to better understand the petrology and formation history of the BSM by characterizing the composition of and placing temporal constraints on the evolution of the lunar farside. In order to achieve the science goals outlined above, trace element analyses will need to be carried out in lithologies representing the upper mantle and melting of lower mantle mare source regions. To maximize science return, the specific landing sites that would provide the most valuable samples for this investigation samples should be considered carefully. Modeling of the impact origin of the South Pole Aitken (SPA) basin indicates that the large impactor on the lunar farside produced an impact melt reaching 400-600 km in depth, which homogenized into norite and troctolite in the valley floors of impact basins [91]. This impact melt resulted in anomalously thin crust in impact basins, ranging in thickness from $<$1-10 km. Thin crust resulting from impacts preferentially allows melt to puncture through the crust, causing later stage mare basalts to accumulate in impact basins [211]. Thus, impact basins containing both norite/troctolite impact melts and later stage mare emplacement are ideal candidates for the outlined analyses.

We assessed potential landing sites on the lunar farside using orbital-based spectroscopic and geophysical measurements, with data overlays compiled using the *LRO Quickmap* mapping tool. TiO_2 measurements are derived from the Lunar Reconnaissance Orbiter Camera (LROC) Wide-Angle Camera (WAC), using 321/415 nm band ratios, crustal thickness is derived from the GRAIL mission Bougier gravity anomaly map. Surficial mineralogy is derived from the Kaguya Mineral Mapper instrument, and slope measurements generated using the LRO LOLA laser altimeter. Landing site analyses were carried out to minimize mission risk and maximize science return. Sites were selected based on four main criteria:

- Low crustal thickness anomalies
- Norite or troctolite exposed on the impact basin floor
- Later-stage mare deposits within the impact basin
- Landing site hazards (e.g. slope, temperature, rock/fine fraction)

Based on these criteria, we have identified Moscoviense, Apollo, Von Kármán, and Leibnitz craters as potential landing sites (Fig. 3.6). A potential landed mission could baseline a mobile platform such as a rover or a secondary launch vehicle, to sample both basement impact melt and mare deposits. A summary of each landing site analysis is found in Table 3.2.

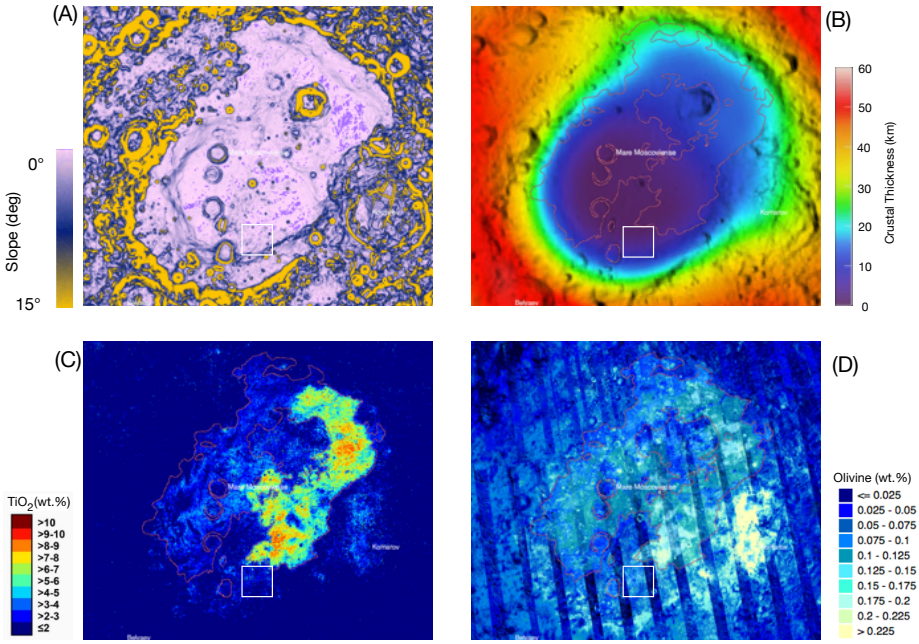

Fig. 3.7: (A) Slope, (B) crustal thickness, (C) TiO_2 abundance, and (D) olivine abundance maps of Moscoviense crater. White square identifies proposed landing site.

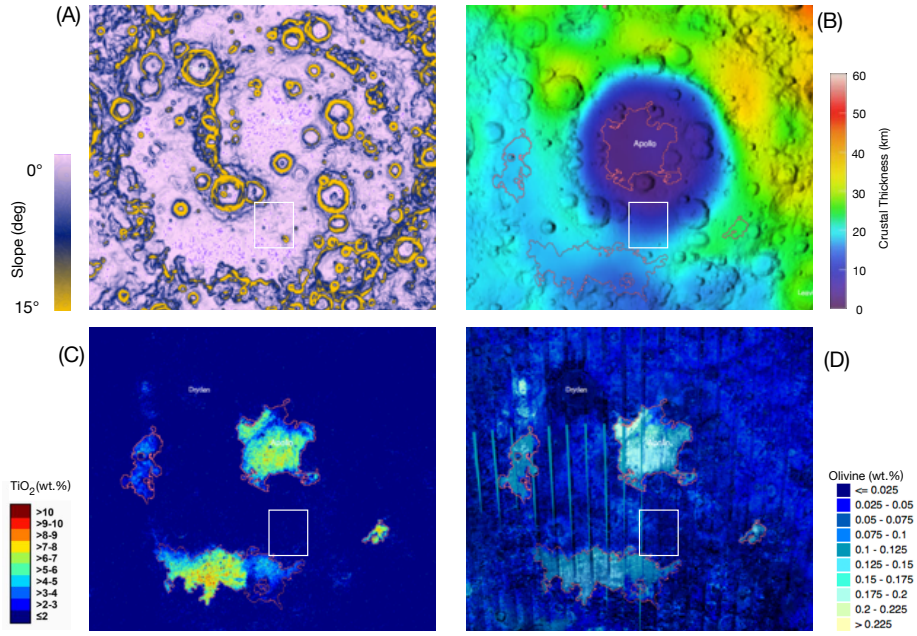

Fig. 3.8: (A) Slope, (B) crustal thickness, (C) TiO_2 abundance, and (D) olivine abundance maps of Apollo crater. White square identifies proposed landing site.

3.5.1 Moscoviense Crater

Moscoviense is a Nectarian-age impact basin with a series of concentric ring impact structures and multiple Imbrium and Erasthothenian-aged mare units [191]. It is the northernmost impact basin considered as a landing site on the lunar farside, and thus not associated with the impact formation of the SPA basin. Despite the impact structures, the valley of the basin contains limited topographical features and near zero slope, providing a relatively hazard-free terrain to traverse. This landing site could provide a window into the lunar mantle as the crust beneath Moscoviense is the thinnest part of the lunar surface, with crustal thickness estimates from 400-500 m based on measurements from the Kaguya and GRAIL missions [93, 207]. TiO_2 measurements and crater counting estimates of the later-emplaced mare basalts show a time and compositional discrepancy between basalt units, with older mare units to the northwest having a distinctly lower TiO_2 abundance ($<$2 wt.%), and younger units to the east having a significantly higher (5-10 wt.%) TiO_2

abundance (Fig. 3.7). This suggests that the mare emplaced in Moscoviense reflects multiple mantle source regions, allowing a multi-faceted investigation into the composition and formation history of the lunar mantle.

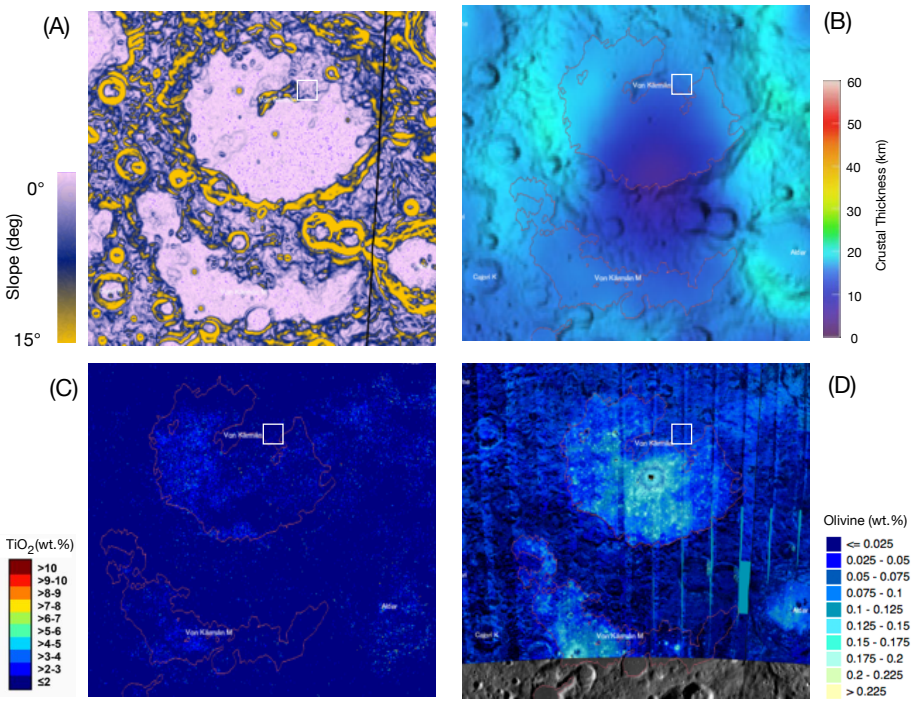

Fig. 3.9: (A) Slope, (B) crustal thickness, (C) TiO_2 abundance, and (D) olivine abundance maps of Von Kármán crater. White square identifies proposed landing site.

3.5.2 Apollo Crater

Apollo crater is the largest impact structure in the SPA basin, with its formation age estimated as pre-Nectarian based on crater counting measurements. The SPA basin is an important target for understanding lunar history, as crater ages from this region can help explain the timing and intensity of the impactor flux during this period of time, enabling a critical evaluation of the putative Late Heavy Bombardment (LHB). Further, the region itself represents portions of the lunar upper mantle exposed through impact melts; the valley floor of Apollo crater represents one such exposure. Norite and troctolite in the

	Moscoviense	Apollo	Von Káramán	Leibnitz
Coordinates (lat)	23.32° - 24.7°	−38.62° - −40.91°	−43.32° - −44.33°	−37.94° - −39.16°
Coordinates (long)	146.83° - 148.00°	−149.51° - −151.53°	176.81° - 177.84°	−-178.26° - −179.79 °
Crustal Thickness	< 500 m	< 1 km - ∼5 km	10 - 20 km	5 - 10 km
Slope	2° - 7°	<1° - 5°	1° - 10°	<1° - 2°
Temperature Anomaly	+5 K	+2 K - +3 K	−3 K - 3 K	−3 K - 3 K
Olivine (wt.%)	2.5 - 7.5	7.5 - 12.5	2.5 - 5	<2.5 - 7.5
Orthopyroxene (wt.%)	21 - 28	28 - 35	21 - 28	21 - 35
Clinopyroxene (wt.%)	25 - 30	7 - 14	14 - 28	14 - 28
Plagioclase (wt.%)	10 - 15	30 - 50	15 - 25	25 - 40
FeO (wt.%)	12.5 - 15	10 - 15	10 - 12.5	10 - 15
TiO_2 (wt.%)	2 - 3	<2	<2 - 3	<2
Stratigraphic Age	Nectarian	Pre-Nectarian	Pre-Imbrium	Pre-Nectarian

Table 3.2: Overview of assessment of four landing sites proposed for trace element analyses. Data for each site taken from LRO - Quickmap mapping tool. Crustal thickness measurements from GRAIL mission, slope measurements from LRO - LOLA instrument, Temperature anomalies from LRO - DIVINER instrument, mineralogy from SELENE/Kaguya measurements, and TiO_2 measurements from LROC - WAC 321/415 nm band ratio.

crater valley floor likely formed as impact melt, and the low crustal thickness ($\sim$5 km) reinforces that Apollo is an ideal candidate for measuring the lunar upper mantle and constraining the impact age of the SPA basin. Apollo crater also contains up to 8 distinct mare basalt units, separated spatially, chronologically, and compositionally (Fig. 3.8). Similar to Moscoviense, mare units to the southwest show compositional differences, with older units having significantly lower TiO_2 than younger units, suggesting a shift in the mantle source of mare basalts in Apollo crater as well.

3.5.3 Von Kármán Crater

Von Kármán crater is pre-Nectarian in age and lies to the southwest of Leibnitz crater, thus is compositionally similar both in basement rock lithology and later emplacement of mare basalts. Von Kármán is comprised of multiple ring structures with mare units infilling the ringed units. Measurements from the M^3 spacecraft on the Chandryaan-1 mission show the area surrounding Leibnitz and Von Kármán crater contains abundant pyroxene [137], mainly Ca- and Fe- rich pyroxene in the north and northwest region of the SPA basin. The northernmost rim of the crater is characterized by norite and troctolite basement rock with mare basalt infilling the majority of the basin. The northern rim is also marked by multiple smaller craters and slightly sloped areas of 2°-7°. Crustal thickness measurements show the northern rim with 15-20 km crustal thickness, but a crustal thickness $<$5km on the southern portion of the largest mare unit (Fig. 3.9). Von Kármán crater is also the landing site of the Change-4 Yutu rover, although basement impact melt units cannot be accessed by this mission.

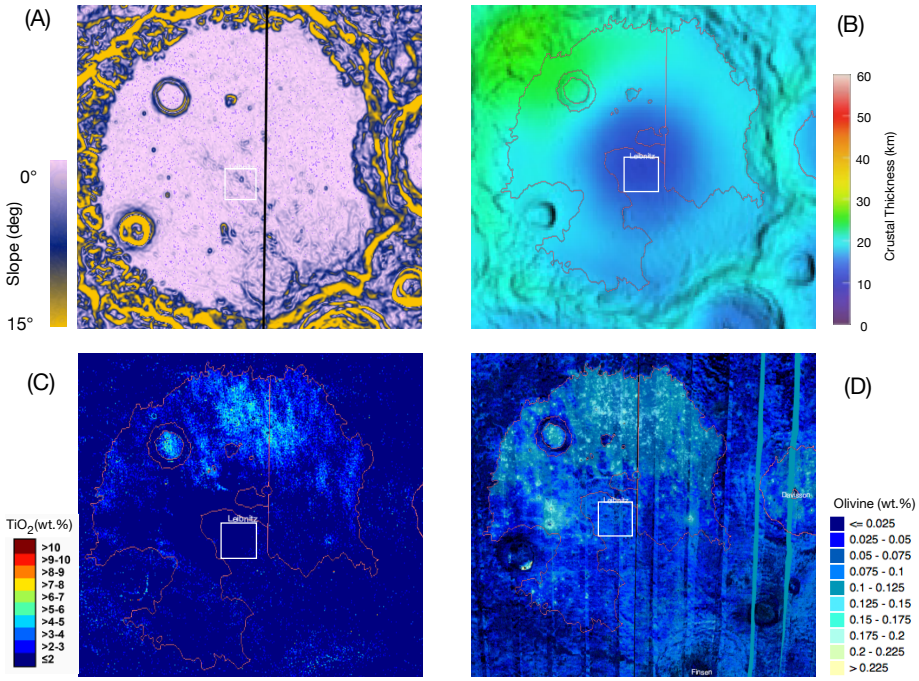

Fig. 3.10: (A) Slope, (B) crustal thickness, (C) TiO_2 abundance, and (D) olivine abundance maps of Leibnitz crater. White square identifies proposed landing site.

3.5.4 Leibnitz Crater

Leibnitz crater is found at the northwest corner of the SPA basin, with its stratigraphic age being pre-Imbrium to post-Nectarian. Leibnitz crater is characterized by a larger amount of mare infill as compared to Apollo and Moscoviense, with mare basalts filling in the majority of the crater basin floor, which itself is noritic in composition [20, 91]. The central portion of the crater is also marked by thin crust (5-10 km), meaning the noritic basement unit is likely reflective of the homogenized upper mantle after an impact melt (Fig. 3.10). This area is also a relatively flat region with few large boulders, minimizing the operational hazards of a landed mission. UV/VIS spectroscopy also shows excavated gabbroic ejecta inside the basin from nearby Finsen crater, possibly allowing the analyses of material from multiple impacts [20].

The landing sites identified here can provide a window into the lunar farside interior, with impacts producing thin crust and possibly exposing the upper mantle, and later basaltic melts reflecting previously unsampled mare source regions. Applying the chemical analyses outlined here to both impact melt and mare basalt lithologies can maximize the science return of a landed mission. In situ chemical analyses of trace elements in rocks representing specific processes and eras in lunar history can be a low risk, high reward strategy for future lunar science.

3.6 Conclusions

Here, we show how trace elements are a useful tool for deconvolving the lunar past. Analysis of trace elements has been demonstrated on previous missions to a range of other planetary environments. Heritage instruments and emerging technologies will allow measurements of elemental abundances to lower limits of detection and higher degrees of accuracy and precision than realized historically. These technologies can be used to redefine evolutionary models of the Moon at specific landing sites on its farside, namely impact melts and later basaltic magmatism, as well as provide insights into the distribution of valuable trace elements in local surface materials. Trace element analyses on lunar farside rocks could provide significant science return for less risk than a crewed mission or sample return, and should be one of the major focus areas for future landed lunar science.

Chapter 4: A Prospective Microwave Plasma Source for In Situ Spaceflight Applications

Note: This chapter has been previously published at the following citation, and is currently available via open access:

Farcy, B. J., Arevalo, R. D., Taghioskoui, M., McDonough, W. F., Benna, M., & Brinckerhoff, W. B. (2020). A prospective microwave plasma source for in situ spaceflight applications. Journal of Analytical Atomic Spectrometry, 35(11), 2740-2747.

4.1 Abstract

Noble gas plasmas are commonly used as ion and excitation sources in inductively coupled plasma (ICP) optical emission and mass spectrometry for organic and inorganic chemical analysis. However, the high power ($\sim$kW) and voluminous gas flow rate ($\sim$15 L/min) of commercial plasmas limit their potential deployment in remote terrestrial and planetary environments. Here, using argon and helium gas supplies, we investigate the fundamental characteristics of low power and reduced-pressure microwave plasmas for organic and elemental analysis. These plasmas require a fraction of the power ($<$25W) and gas ($<$0.2 L/min) compared to conventional ICP systems. Langmuir probe measurements were used to determine electron temperatures and electron densities for both helium and argon plasmas under a range of forward of powers and gas flow rates. Ionization efficiencies for select organic compounds and elemental species were estimated from these results using

the Saha equation. Our findings show that at 23 W of forward power and 0.2 L/min gas flow rate, an argon plasma can fully ionize (<99%) organic molecules or elements with high ionization potentials (e.g. glycine, 8.9 eV, or S, 10.4 eV); in comparison, helium can achieve similar performance metrics with as little as 5 W of forward power.

4.2 Introduction

Constraints on planetary surface composition are obtained through various analytical techniques, including ground-based telescopes, remote sensing from orbiting spacecraft, and in situ measurements from landed platforms. In situ spectroscopic techniques provide particularly valuable information across a range of spatial scales, such as correlated measurements of mineralogy, elemental composition, and biomarker detection, as demonstrated by the Sample Analysis at Mars (SAM) instrument onboard the Curiosity rover [51, 63, 110]. Advances in laser desorption/ablation mass spectrometry target the unambiguous identification of potential biosignatures, and contextualize geological relationships that inform on molecular provenance and formation mechanisms [14]. However, such techniques are challenged to meet the figures of merit (e.g., accuracy, precision, and detect limits) required to provide quantitative bounds on elemental composition and/or organic inventory, particularly for refractory elements and macromolecular compounds.

In the commercial realm, plasmas are routinely applied as robust and reproducible sources for optical emission spectra [88, 197], as well as ionized organic compounds and monoatomic ions for mass spectrometry [2, 32, 33, 76, 126, 138, 164, 183]. Commercial inductively coupled plasmas (ICPs) operate at high power output (>1 kW) and ionize desolvated solutions or ablated geologic material. Recent advances in plasma technology demonstrate that low power plasma sources, operating at ambient or reduced pressure, perform direct desorption and ionization of molecular compounds or geologic materials

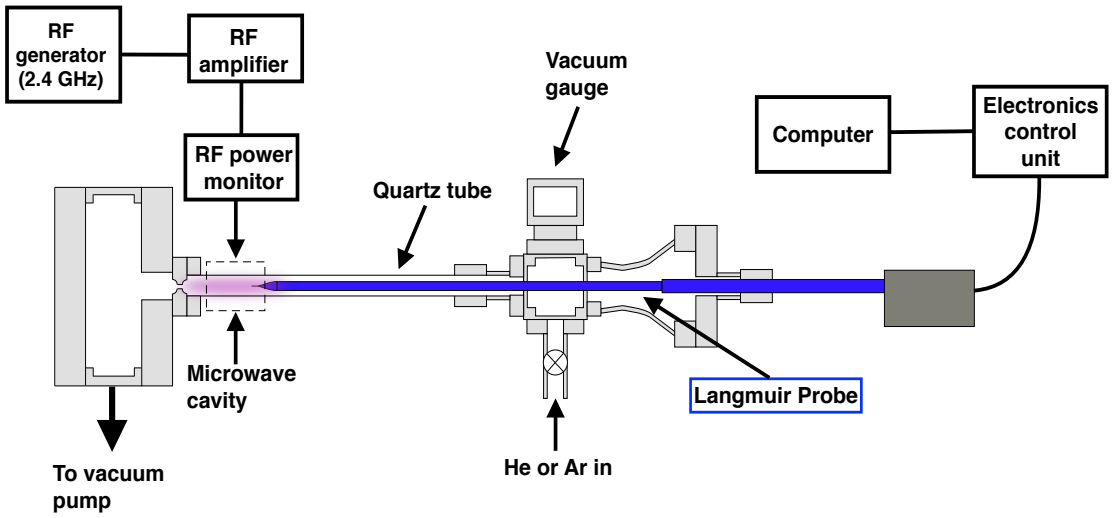

Fig. 4.1: Schematic diagram a low power (¡30 W), low gas flow rate (¡200 SCCM, or 0.2 L/min), plasma ion source operated at 10 torr (∼1300 Pa). Langmuir probe (in blue) has been inserted in the setup to characterize the ionization properties of the plasma. The dashed box with pink color identifies the site of plasma generation and sampling by the Langmuir probe.

in their native state, although the potential to atomize large particles remains poorly constrained. [126] These sources typically operate at low power (3-30 W) and low gas flow rates ($<$ 1L/min), opening the potential for them to be used as in situ instruments for spaceflight. Despite this progress, the ionization capabilities of these low power plasma sources for organic or elemental analysis require further characterization.

Here, we document the capability of microwave induced plasmas (MIPs), operating at low power and low pressure with argon and helium, to ionize refractory elements and macromolecular organics. We measured the fundamental parameters of the plasma via Langmuir probe over a range of forward powers and gas flow rates: Specifically, electron temperatures, electron densities, and ion currents were recorded under each set of analytical conditions. These data are used in conjunction with the Saha equation to estimate the first ionization capabilities of these plasmas for molecular and elemental analyses and can be applied to any specific analyzer. We define the performance capabilities of the plasma source, highlighting the potential for this subsystem to serve as an effective spaceflight ion-

ization source. Applications of this plasma source extend from the ionization and controlled fragmentation (to derive structural information) of organic compounds on ocean worlds, to the quantitative analysis of trace elements on the surfaces of rocky planetary bodies, to the derivation of radiometric ages via the Rb-Sr and/or U-Th-Pb systems.

4.3 Methods

4.3.1 Experimental Setup

Fig. 1 presents a schematic of our vacuum chamber to generate a low pressure, low power plasma that can operate as an ion source for a prototype spaceflight chemical analyzer. The setup in Fig. 1 is coupled to a Langmuir probe to characterize the the fundamental properties of the plasma, enabling quantitative insights into the ionization efficiencies of different analytes.

We use a resonance cavity to produce a microwave plasma, which is generated within a quartz tube (12.5 mm outer diameter and 1.25 mm wall thickness) passing through the cavity. [111] A signal generator (Hewlett Packard, 8648C) produces a radio frequency (RF) between 2.3 - 2.45 GHz, enhanced by a RF amplifier (Mini-Circuits, ZHL-30-252-s+) that provides improvements in linear performance and gain. The amplifed RF signal is then fed into an Evanson microwave cavity [58] (Opthos Instruments) via a bi-directional coupler. Two power meters (ImmersionRC, 8452) are connected to the coupler to monitor the forward and reflected power in real-time.

In contrast to the Evanson microwave cavity employed here, commercial inductively coupled plasma optical emission spectroscopy (ICPOES) or mass spectrometry (ICPMS) instruments typically use a coil wrapped around a quartz tube. In these systems, the frequency of RF frequency is generally 13.56, 27.12 or 40.68 MHz, and a capacitive network matches the impedance of the coil to the impedance of the RF power supply. Lower fre-

quency atmospheric pressure argon plasmas can be advantageous, producing higher signal to noise ratios and analyte excitation temperatures. [133] However, high frequency microwave plasmas ($>$ 100 MHz) generally produce greater ion beam currents, lower beam energy dispersion, and better frequency coupling to the plasma. [23, 133, 193] Here, we use a high frequency plasma for its enhanced coupling efficiency at lower power outputs.

In order to maximize the forward power of the microwave, the resonance frequency of the cavity is tuned using the cavity's tuning rod to minimize the reflected power, and then the output frequency was further optimized to match the resonance frequency of the cavity. A second resistive tuning element allowed impedance matching to minimize reflected power. This tuning procedure is performed in all experiments to maintain a reflected power of $< 5\%$.

The quartz tube connects two vacuum chambers and argon or helium is introduced via a mass flow controller (Alicat, MC-500SCCM-D) into the first chamber and subsequently pumped downstream through the chamber using an oil-free roughing pump. A 1 mm ($\pm$ 25 μm) laser-drilled conductance limiting orifice (Lenox Laser, SS-CF-2-1000) separates the pumping chamber and the quartz tube in order to restrict gas flow and enable differential pumping between the two chambers. The plasma chamber is evacuated to a pressure of ¡ 100 millitorr (10 Pa) and back-filled with a controlled flow of plasma gas, ranging from 200 to 10 standard cubic centimeters per minute (SCCM), and supporting the characterization of plasma across a range of pressures from 1-10 torr ($\sim$ 100 - 1000 Pa). The power is adjusted from 5 - 23 W to maintain a stable plasma across these flow rate and pressure parameters. A commercial Langmuir probe (Impedans Inc.) having a 0.25 mm diameter and a 10 mm long tungsten probe tip was inserted into the quartz tube to measure plasma characteristics. Voltage on the probe was swept over a range of -50 to 50 V and the resulting I-V curves were recorded using the Impedans Langmuir probe software.

4.3.2 Langmuir Probe Data Processing

The Langmuir probe is a diagnostic tool used to measure the fundamental characteristics of a plasma. The probe is a conducting wire that is inserted into a plasma. An I-V curve is generated by measuring the current resulting from an applied or bias voltage. The values for plasma potential (V_p), floating potential (V_f), electron temperature (T_e), electron density (N_e), and electron energy distribution function (EEDF) are calculated from I-V curve measurements. [27, 92, 132] V_p describes the electric field potential in the space in between the ions or electrons in the plasma, and thus the potential of the plasma relative to ground. V_p is defined by the voltage value at which the I-V curve shows the greatest change in slope ($\frac{d^2I}{dV^2}$), and V_f is defined as the voltage value at which the ion and electron current are equal, resulting in a net zero current.

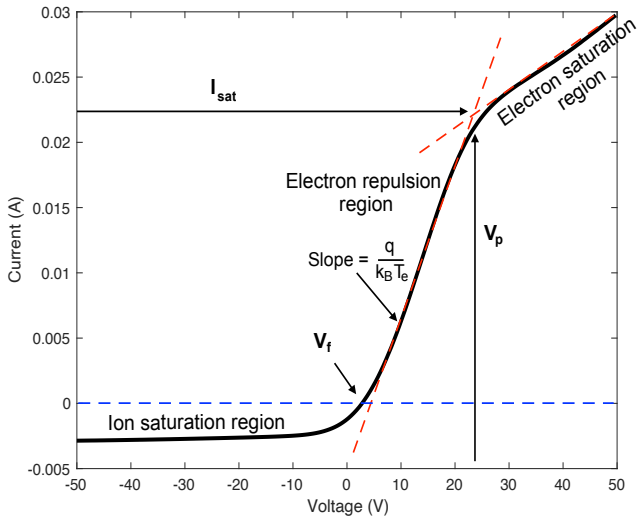

Fig. 4.2: Example of relevant regions of an I-V curve as measured from a He plasma at 11 W and 200 SCCM gas flow rate. Values for V_p, V_f, T_e, and I_{sat}, as well as distinct regions of the curve, are identified. Terms identified in the main text.

V_p is determined by taking the natural log of the measured current and fitting a line to the region above and below the change in slope, or the "knee" of the curve. The intersection of these two lines identifies V_p (Fig. 2).

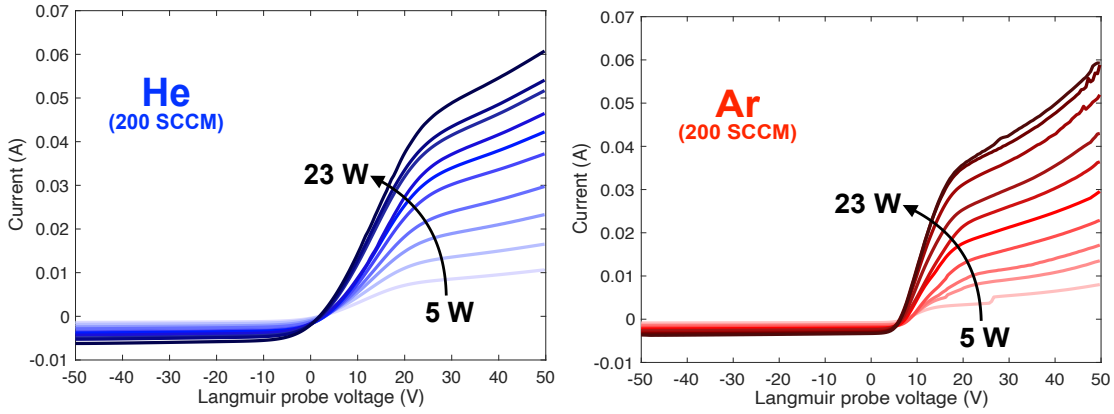

Fig. 4.3: Composite of I-V curves taken over a range of plasma powers for helium (a) and argon (b) plasmas at a constant gas flow rate.

The slope of the electron repulsion region can be used to calculate electron temperature (T_e) as:

$$\frac{q}{k_B T_e} = \frac{ln|I_{probe} - I_{sat}|}{\varepsilon} \tag{4.1}$$

where q is the electron charge, k_B is the Boltzmann constant, I_{probe} is the probe current at V_p ¿ V_{probe} ¿ V_f, and I_{sat} is the saturation current (defined as current at V_p), and ε is the energy given by $V_p - V_f$. T_e is in units of electron volts (eV). Electron density is subsequently calculated as:

$$N_e = \frac{I_{sat}}{qA_{probe}e^{-\frac{1}{2}}}\sqrt{\frac{m_e}{k_B T_e}} \tag{4.2}$$

where A_{probe} is the surface area of the probe and m_e is the electron mass. N_e is in units of m^{-3}.

The electron energy distribution function (EEDF), for this type of low temperature plasma, approximates a single Maxwellian distribution of electron temperatures that are higher than the bulk plasma temperature. The EEDF was calculated using the second

derivative of the I-V curve, with the ion current subtracted, as:

$$n(\varepsilon) = \frac{2I''}{qA_{probe}}\sqrt{\frac{2m_e\varepsilon}{q}} \tag{4.3}$$

where I'' is the second derivative of the current.

In addition to T_e and N_e measurements, a static potential is applied to the Langmuir probe and the ion current is measured in the center of the plasma. The ion current is proportional to ion density, so it is used to calculate changes in plasma ion/neutral ratio with changing plasma input parameters. The experiments are conducted for both argon and helium gases to compare performance under a range of conditions. While the physical characteristics of the plasma change laterally on either side of the microwave cavity, the three dimensional nature of the plasma was not investigated here. Instead, because the probe is measuring the plasma at its hottest position, the ion current, T_e, and N_e values measured represent upper bounds of the plasma state and we assume a drop off in values as the probe position changes.

4.4 Langmuir probe measurements

4.4.1 The Effects of Plasma Power on T_e and N_e

A compilation of measured I-V curves taken over a range of forward plasma powers is shown in Fig. 3. The gas flow rate was maintained at 200 SCCM while power was varied in order to study the effects of plasma power on T_e and N_e. Ramping up the plasma power (5-23 W) resulted in an increase in N_e by a factor of 3 for helium and a factor of 5 for argon, as indicated by increasing I_{sat}, and only slight increases (a few percent) in T_e (Fig. 4a), due to a minimal change in V_p (Fig. 3a & b). The trend in electron density with changing plasma power (Fig. 4b) is due to a greater number of high-energy

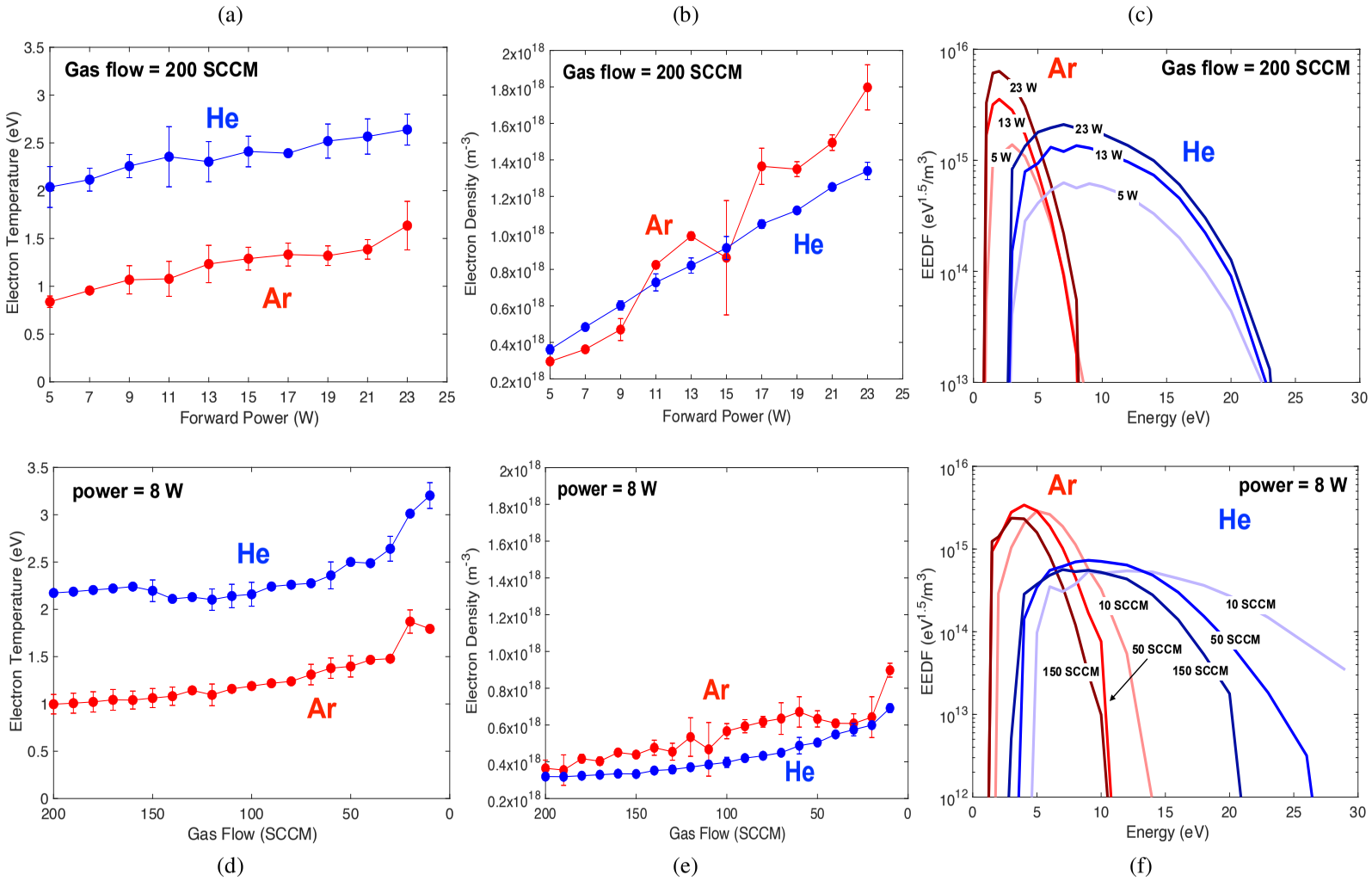

Fig. 4.4: Electron temperature (T_e) and electron density (N_e) results of Langmuir probe measurements as a function of plasma power (a-c) and gas flow rate (d-f), as well as electron energy distribution (EEDF) measured for select values for plasma power and gas flow rate. Plasma power measurements taken at a constant gas flow rate of 200 SCCM, and gas flow rate measurements taken at a constant plasma power of 8 W. Data points are averages of 3 consecutive measurements, and uncertainties are calculated as $2\sigma_m$. Observed differences in the electron density of Ar, relative to He, at low forward power is attributed to minor variations in operational conditions following gas changes.

inelastic collisions occurring with increasing forward plasma power. Increasing power produces an increase in the amplitude of oscillations, thus more energy per electron per oscillation. Unlike low mass electrons, large atoms/molecules have insufficient time to respond to changes in polarity in the resonance cavity (which control directional changes in the plasma magnetic field) at microwave frequencies. This is corroborated by similar increases in ion current (more below, Fig. 5).

This weak relationship between T_e and plasma power is consistent with measurements from other studies of inductively coupled RF plasmas [24, 29, 139]. The higher T_e for helium, as compared to an argon plasma, is likely due to helium having a higher thermal conductivity than argon (0.151 and 0.018 W/mK at 25 °C and 0.1 MPa, respectively). [108] However, the response difference in N_e follows from the differences in ionization potential of argon versus helium (15.8 eV and 24.6 eV, respectively) and ionization cross section (3×10^{-16} and 0.4×10^{-16} cm^2, respectively). [165]

The plasma gas temperature (T_{gas}) was measured using a hand held IR thermal imager (Keysight Technologies, U5850 series). The argon gas temperature measured over the range of forward power increased from 340 to 380 K, while the helium gas temperature increased from 380 to 510 K.

4.4.2 The Effects of Gas Flow Rate on T_e and N_e

The plasma gas flow rate in the system also affects the physical characteristics and ionization capabilities of the plasma. To assess these responses, the plasma power was kept constant at 8 W while the flow rate of plasma gas was changed from 200 to 10 SCCM. Changes in T_e and N_e as a function of gas flow rate is shown in Fig. 4d-e. Both T_e and N_e are inversely proportional to gas flow rate, with their highest values being measured at the lowest gas flow rates.

For both gases there is about a 40% increase in T_e with a factor of 10 decrease in gas flow rate. The relationship between T_e and gas flow rate is driven by the electron collision frequency. If electrons are borne with a set kinetic energy, then inelastic collisions decrease that kinetic energy with each collision. A decrease in gas pressure, and thus a decrease in electron collisions, allows electrons to better retain their initial kinetic energy. [139, 181]

The mean free path of an electron in a plasma can be calculated using the Debye length, or the distance a plasma can shield from external charge.[112] The Debye length is calculated as:

$$\lambda_D = \sqrt{\frac{\varepsilon_o k T_e}{N_e q_e^2}} \tag{4.4}$$

Where q_e is the charge of an electron and ε_o is the permittivity constant. Langmuir probe measurements show Debye lengths from 1-3$\times 10^{-5}$ m from 10 - 200 SCCM gas flow rates. The Debye number (N_D) is the number of electrons within a sphere with a radius of λ_D, calculated as:

$$N_D = \frac{4\pi}{3} N_e \lambda_D^3 \tag{4.5}$$

With the electron mean free path calculated as:

$$\lambda_{MFP} \sim \lambda_D \times N_D \tag{4.6}$$

This results in electron mean free paths of $\sim$tens of cm in Ar plasma and $\sim$1 m in He plasma. A root mean square velocity (V_{RMS}) of the electron is calculated to be tens of km/s, as:

$$V_{RMS} = \sqrt{\frac{3 k_B T_e}{m_e}} \tag{4.7}$$

Thus, decreasing gas pressure decreases mean free path by increasing electron density. The electron - ion collision frequency is calculated as:

$$\nu_{ie} = \frac{V_{RMS}}{\lambda_{MFP}} \tag{4.8}$$

so increasing the gas pressure increases collision frequency, which reduces the initial kinetic energy of the electron.

The N_e increases by less than a factor of 2 over the range of observed gas flow rate. Similar to the trends of plasma power, argon N_e increases at a steeper slope than helium, suggesting a sensitivity to the lower first ionization potential or larger ionization cross section. Because higher energy collisions result in greater electron density, and reducing the gas flow rate increases collision energy, then the increase in electron density is due to the increase in electron energy with lower gas flow rates. The order of magnitude greater ionization cross section of argon leads it to have a greater number of collision events than helium, and thus a greater electron density as well. However, N_e increases twice as fast over the range of observed forward power than with changes in gas flow rates, which suggests that plasma power has a stronger affect on electron density.

Changes in electron temperature and density are reflected in the calculated EEDF, where T_e and N_e both affect the distribution of electron energy in the plasma. Based on their calculated EEDFs, helium has a wider energy distribution and a greater population of high energy electrons than an argon plasma (Fig. 4c & 4f). This ”hot tail” of electrons has been previously documented, and is generated from elastic collisions of helium in metastable states.[70] The mean energy of each distribution shows little variation with changing plasma power, but shows a systematic increase in energy distribution with decreasing gas flow rate.

4.4.3 Ion Current Measurements

The measured ion current reflects the overall population densities, with changes in plasma power or gas flow rate manipulating the plasma's ion and electron populations. Fig. 5 shows plasma ion current versus forward power for two different gas flow rates and gases with a static potential of -20 V applied to the Langmuir probe.

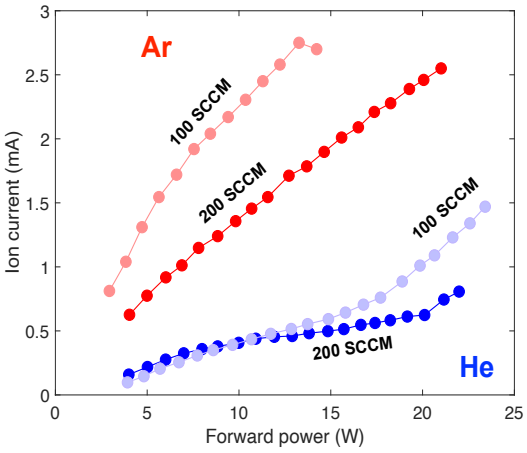

Fig. 4.5: Ion current versus forward power taken with a -20 V static voltage potential applied to the Langmuir probe for 200 and 100 SCCM gas flow rates.

The measured ion currents for argon and helium show markedly different behaviors. Regardless of the specific set of conditions, argon plasmas have higher ion currents than helium plasmas; further, argon ionization is more sensitive to changes in gas flow rate. Thus, argon is more easily ionized by a change in both pressure and power, which is again reflective of its lower first ionization potential and greater ionization cross section relative to helium. The different curves of ion current for 200 and 100 SCCM are consistent with N_e measurements, where electron density is inversely proportional to gas flow rate.

The ion density of the plasma is related to the electron density, assuming plasma quasineutrality and negligible contributions from 2+ ions ($N_e = N_i$, see Appendix C). Thus, the previously measured electron density can be used to estimate the ion/neutral ratio of the plasma. We calculate the neutral gas density (N_{gas}) using the ideal gas law ($PV = nRT$). The plasma gas pressure was 10 torr (1300 Pa), the chamber volume was 3.3 cm^3, and the maximum values for T_{gas} were 360 K for argon and 510 K for helium. From this, the total gas density within the volume of the quartz tube is 7×10^{17} atoms. Assuming a measured

N_e value of 10^{17} - 10^{18} m^{-3}, this yields an ion/neutral ratio of 10^{-5} - 10^{-6}. This is two to three orders of magnitude lower than commercial, high power plasmas with a typical ion/neutral ratio of 10^{-3}.[147] A comparison of the characteristics of this plasma to those used in commercial systems is found in Table 1.

4.5 Estimates for analyte ionization

The plasma described here is being developed to ionize injected samples for chemical and isotopic analyses. Therefore, steps must be taken to estimate the ionization efficiency of the plasma on individual organic (molecular) and elemental (atomic) species. The ion/neutral ratio calculated in the previous section is specific to the plasma gas itself, but the parameters measured via Langmuir probe, namely T_e and N_e, can inform the ionization efficiencies of other elements using the Saha equation.

The Saha equation [21, 22, 72, 87, 147] is:

$$K_{ion} = \frac{N_i N_e}{N_o} = 2\frac{g_i}{g_o}\left(\frac{2\pi m_e k_B T_e}{h^2}\right)^{\frac{3}{2}} e^{\frac{-E_i}{k_B T_e}} \tag{4.9}$$

Where K_{ion} is the ionization constant, N_e, N_i, and N_o are the electron, ion, and neutral population densities, g is the statistical weight of an electron transition, h is Planck's constant, and E_i is the first ionization energy of an element. Values for g for both ion and neutral species were taken from the NIST atomic spectroscopy database. [101] Niu & Houk reduced this version of the Saha equation to eliminate the use of constants, [147] and the log of the equation can be written as:

$$log(K_{ion}) = 1.5log(T_e) - \frac{5040E_i}{T_e} + log\left(\frac{g_i}{g_o}\right) + 15.684 \tag{4.10}$$

Using the ionization constant (K_{ion}), the proportion of input sample ions to neutrals (α_i)

is:

$$\alpha_i = \frac{K_{ion}}{K_{ion} + N_e} \tag{4.11}$$

In order to gain confidence in our use of the Saha equation, we performed an additional experimental check on the Saha ionization of an analyte in a plasma environment. We performed a series of ICP-OES measurements on the ion/neutral ratio of three elemental samples (Mg, La, and Zn), as well as on the T_e and N_e values of the plasma itself. The values for T_e and N_e were input into the Saha equation, and the Saha-predicted ionization efficiency was compared to the directly measured ion/neutral ratio from line emission intensities. Our results show that the Saha equation produces ionization efficiency estimates within 2-5% of measured ratios, validating our use of the Saha equation for these models (see Appendix C. for more details).

Although our Langmuir probe measurements of plasma T_e range from 10,000 - 35,000 K ($\sim$1-3 eV), plasma T_{gas} measurements are much lower, in the range of 340 - 510 K based on measurements taken with the handheld IR thermal imager. Because there is a divergence between gas and electron temperatures, the plasma is not at a local thermal equilibrium (LTE). Non-LTE plasmas are common in low pressure systems. Previous estimates for Saha ionization, carried out by Niu & Houk on a commercial plasma at atmospheric pressure,[147] assumes a plasma at LTE where T = T_i = T_e = T_{gas} = 7500 K. However, Chen & Han assessed the Saha equation for a non-LTE plasma,[28] and found that T_e is the appropriate temperature to use as an input for the non-LTE Saha equation, as electron collisions are the dominant mechanism of ionization. Therefore, we use the framework of the Saha equation established by Niu & Houk, [147] (Eq. 8 & 9) with values of T_e converted to K (1 eV = 11,600 K) input as the plasma temperature.

Because N_e and T_e have been directly measured in the plasma via Langmuir probe,

Operating Condition	Commercial	Experimental
Plasma Gas	Ar	Ar, He
Forward Power	1,000 - 1,300 W	5 - 23 W
Plasma Gas Flow Rate	14 - 16 L/min	0.01 - 0.2 L/min
Frequency	13, 27, or 40 MHz	2400 MHz
Power Coupler	Inductor	Microwave cavity
Max Electron Temp	10,000 K	35,000 K (He)
Max Gas Temp	10,000 K	510 K (He)
Electron Density	10^{21} m^{-3}	10^{18} m^{-3}
Ion/neutral ratio	10^{-3}	10^{-5}*

Table 4.1: Summary of operating conditions and physical properties of a commercial plasma (ICP) and the experimental microwave induced plasma (MIP) investigated in this study. *Experimental plasma ion/neutral ratio at N_e = 10^{18} m^{-3}

we apply this data to the Saha equation to calculate the change in analyte ionization. The curves in Fig. 6 model the degree of ionization as a function of first ionization potential for a range of plasma power inputs. These curves predict the ionization efficiency of an analyte as a function of plasma power.

The estimated ionization models for this low power plasma suggest equal, and in some cases better, ionization efficiencies compared to commercial ICPMS plasmas. [147] Commercial plasmas at atmospheric pressure typically have N_e values of 10^{21} m^{-3}, whereas this plasma is measured to have N_e values of 10^{17} - 10^{18} m^{-3}. This three to four order of magnitude lower electron density, coupled with the higher electron temperature, leads to higher energy collisions and fewer electron-ion recombination events, thus leading to greater analyte ionization efficiency. However, the higher gas temperatures and robust gas flow rates in commercial plasmas can support greater mass loads and more efficient atomization of large particle size distributions than lower power/pressure plasma sources.

We have constructed a thermodynamic model to estimate our low power plasma's efficiency of atomizing ablated geologic materials prior to ionization. Given the measured temperature of the plasma gas and the thermal properties of silica (SiO_2), the dominant

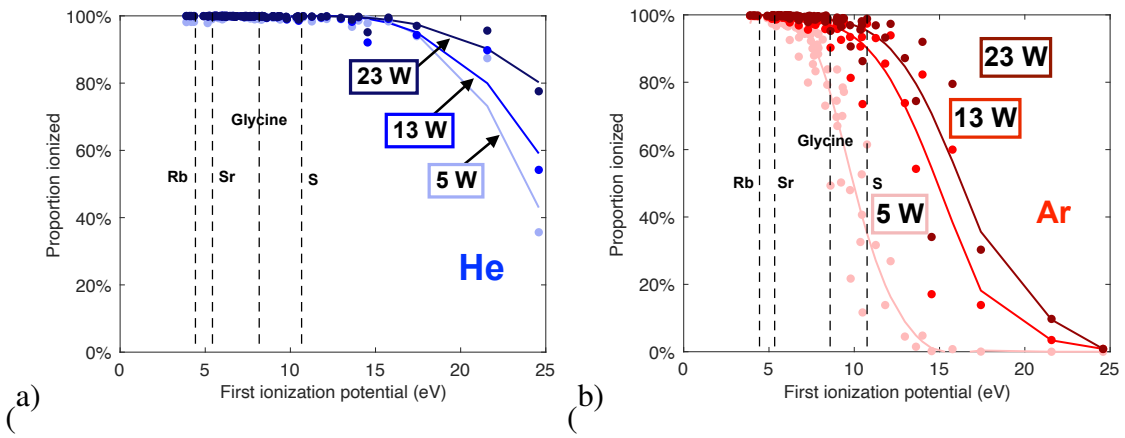

Fig. 4.6: Results of Saha ionization calculations for helium (a) and argon (b) gases at different values of plasma power. Data points are calculated ionization efficiencies for all elements at each forward power condition.

component of most common rocks and minerals, we estimate the maximum mass load a 19 W plasma can support to be on the order of 2×10^{-9} g/s. This flux is similar to that generated by laser ablation with a 40 μm diameter sample spot and a repetition rate of 10 Hz (assuming 50 nm depth removed per shot). The atomization efficiency of the plasma depends on the introduced particle size distribution. We calculate a maximum load capacity of the plasma of 31,000 particles of a 50 nm diameter, or 1,100 particles of a 300 nm diameter (see Appendix C for more details).

The Saha ionization models show that both argon and helium plasma sources can be effective ionizers at low power and gas flow rates. With a gas flow rate of 200 SCCM, organic molecules and atomic species with with a range of first ionization potentials, from radioactive Rb (4.2 eV) and radiogenic Sr (5.7 eV) to prebiotic amino acids (e.g. glycine, 8.9 eV) to biologically and abiologically relevant S (10.4 eV), are calculated to achieve up to 99% sample ionization in a 23 W argon plasma, or a 5 W helium plasma (Fig. 6). Therefore, this plasma could serve as an effective ion source adapted for spaceflight, capable of investigating the organic content, trace element chemistry, and isotopic signatures (including the Rb-Sr chronometer) of geological samples for in situ planetary exploration.

4.6 Conclusion

We have characterized the fundamental parameters of a low power plasma and assessed its performance as an ion source for a mass spectrometer. This plasma is estimated to be an effective ionizer of organic and elemental analytes, with the reduction in power and gas consumption leading to minimal loss in ionization efficiency. Helium is found to be a more efficient ionizing plasma gas than argon, requiring only 5 W of power to ionize fully organic (molecular) and elemental (atomic) species with first ionization potentials $\leq$10 eV, as opposed to 23 W of power for argon. In either case, both of these plasma gases can be used with applications to spaceflight mass spectrometry. Future work will examine possible designs to implement such plasmas onto a prototype spaceflight optical emission or mass spectrometer.

Chapter 5: A Miniature Inductively Coupled Plasma Mass Spectrometer as a Prototype Spaceflight Instrument

5.1 Abstract

Inductively coupled plasma mass spectrometry (ICPMS) is a common laboratory technique for geochemical analysis, but has not yet been miniaturized for applications to in situ planetary exploration. However, low pressure plasma systems are viable ion sources for spaceflight mass spectrometry, given their reduced power and gas flow requirements, and ionization efficiency. Here, a prototype ICPMS has been constructed and demonstrated as an end-to-end system, capable of chemical sample analysis. The prototype consists of a low pressure Ar or He plasma, operating with a 50-100$\times$ reduction of forward power and gas flow relative to commercial systems integrated to a quadrupole mass analyzer (QMA). Computer-assisted design (CAD) modeling was used to plan the mechanical designs of the vacuum housing and ion optics, and conductance calculations were done to ensure low vacuum pressure is maintained throughout the instrument. Chamber construction preceded ion current optimization, leading to measurement of the ion beam by the QMA. Measurements of ion current on the QMA suggest an ion transmission efficiency of 10^{-6} - 10^{-7}, which is a factor of $\sim 10^{-3}\times$ lower than in commercial systems. Kr measured as a sample analyte demonstrates the ability for the instrument to achieve unit resolution, the same standard for legacy systems. The accuracy of measured Kr isotope ratios range from 1% to 57%, all with precision of $\sim \pm 20\%$ (1σ). The ICPMS constructed here represents the successful

integration of a low pressure plasma system, demonstrating the feasibility of this technique as a spaceflight instrument and accomplishing the original goals of this dissertation.

5.2 Introduction

Inductively coupled plasma (ICP) is commonly used as an ion or excitation source for mass spectrometry and atomic spectroscopy. The ICP source in commercial mass spectrometers is typically composed of ionized Ar gas; the plasma is maintained by applying a high power radio frequency (RF) field to a continuous input flow of Ar. The plasma discharge can produce a high temperature environment with a large population of ions and electrons, with temperatures reaching 10,000 K at atmospheric pressure. This plasma is sufficient to volatalize, atomize, and ionize aerosolized solids (e.g. ablated minerals) or liquids (e.g. aspirated solutions), lending it to be an effective ion source for mass spectrometry of planetary materials [148]. The ion source is interfaced with an analyzer and a detector, which separates ions by their mass to charge ratio and measures their abundances. This technique is routinely used in the sciences and medical research [89]. Thus, ICPMS is a robust tool with a long heritage in analytical chemistry.

The process plasma of sample ionization has four main steps that are required for successful input into the mass analyzer:

1. Atomization – The compounds are broken up into their individual atomic components via the high temperature of the plasma. For example, silicate bonds within the rocky material can be broken with a specific amount of energy input into the sample.

2. Volatilization – The broken up atomized sample must then be induced to a high enough temperature that the sample is brought to the vapor phase.

3. Excitation – The high energy of the plasma environment brings valence electrons to

a higher orbital energy. The electrons at this point may either relax back down to a lower energy state and emit a photon, or continue to increase until an electron is removed. Also at the low temperature end of the plasma electrons will re-combined with ions again to form neutrals.

4. Ionization – If a valence electron in an excited state interacts with a free electron, that valence electron could be removed and the atom becomes an ion. Ionization of a sample is required, as ions can be manipulated via electric and/or magnetic fields.

Maintaining the plasma in its high energy state typically relies on a high-power output and a high flow of Ar gas. As the gas system is flowing at $\sim$12-15 L/min, the radio frequency (RF) electric field is generated by a copper coil wrapped around the quartz torch system. The RF operates at high power ranging from 900 – 1,500 W and frequencies of 27 or 40 MHz. The induced electromagnetic field drives initial seed electrons to remove the valence electrons of other Ar atoms, producing a cascade of ionization that is maintained by the strong RF field.

Mass spectrometry has also been applied to spaceflight for decades. Miniaturized spaceflight mass spectrometers have been deployed on a number of missions to planetary surfaces and atmospheres throughout the solar system, and such instruments remain one of the most versatile tools of planetary exploration. While other common laboratory techniques, such as laser desorption/ionization (e.g. MOMA) [69] and gas chromatography mass spectrometry (GCMS, e.g. SAM) [123], have been miniaturized and ruggedized for spaceflight, ICPMS has remained in the commercial realm due to its high power ($>$ 1 kW) and high gas flow ($>$ 15 L/min) to maintain the plasma.

Recently, low pressure plasma has been demonstrated as a viable alternative to atmospheric pressure plasma, as it requires less power and gas flow to achieve comparable ionization efficiency, albiet with a reduced load capacity [55, 183]. In order to demonstrate the

application of ICPMS as a spaceflight technology, I have constructed a prototype ICPMS using a low pressure plasma as an ion source and demonstrated key performance capabilities. This work constitutes the demonstration of low power plasma ICPMS technology as a viable technique for in situ planetary mass spectrometry.

Many conventional mass spectrometers rely on vacuum conditions to allow ions to travel freely with minimal collisions with background gas due to the increased mean-free path of the ions. Additionally, electric fields are used to steer and manipulate ion beams, bringing the sample from the ion source to the mass analyzer. Prior to constructing and optimizing the instrument here, I carried out a full mechanical design of a custom vacuum housing and ion optical elements using SolidWorks computer-assisted design (CAD) modeling. I performed a series of conductance calculations for each differentially pumped chamber, ensuring that the vacuum conditions are sufficiently low to enable ion transmission to the QMA detector. Once the chamber was constructed, I carried out a series of ion current optimization experiments. The experiments involved varying the voltage on each electrode and measuring the ion current delivered through each electrode in the instrument, producing a maximum ion current at each step. The maximum ion current also informed to other aspects of the instrument performance, such as peak shape, collisional losses, and sample introduction.

Here, I discuss the construction, optimization, and validation of a prototype ICPMS, demonstrating its feasibility as a spaceflight instrument.

5.3 Mechanical Design of ICPMS Prototype

The system that was built and designed is required to perform as a mass analyzer, capable of delivering and separating ions produced from the ion source (Fig. 5.1). The mechanics of the chamber were dictated by the ability to transmit ions and maintain a

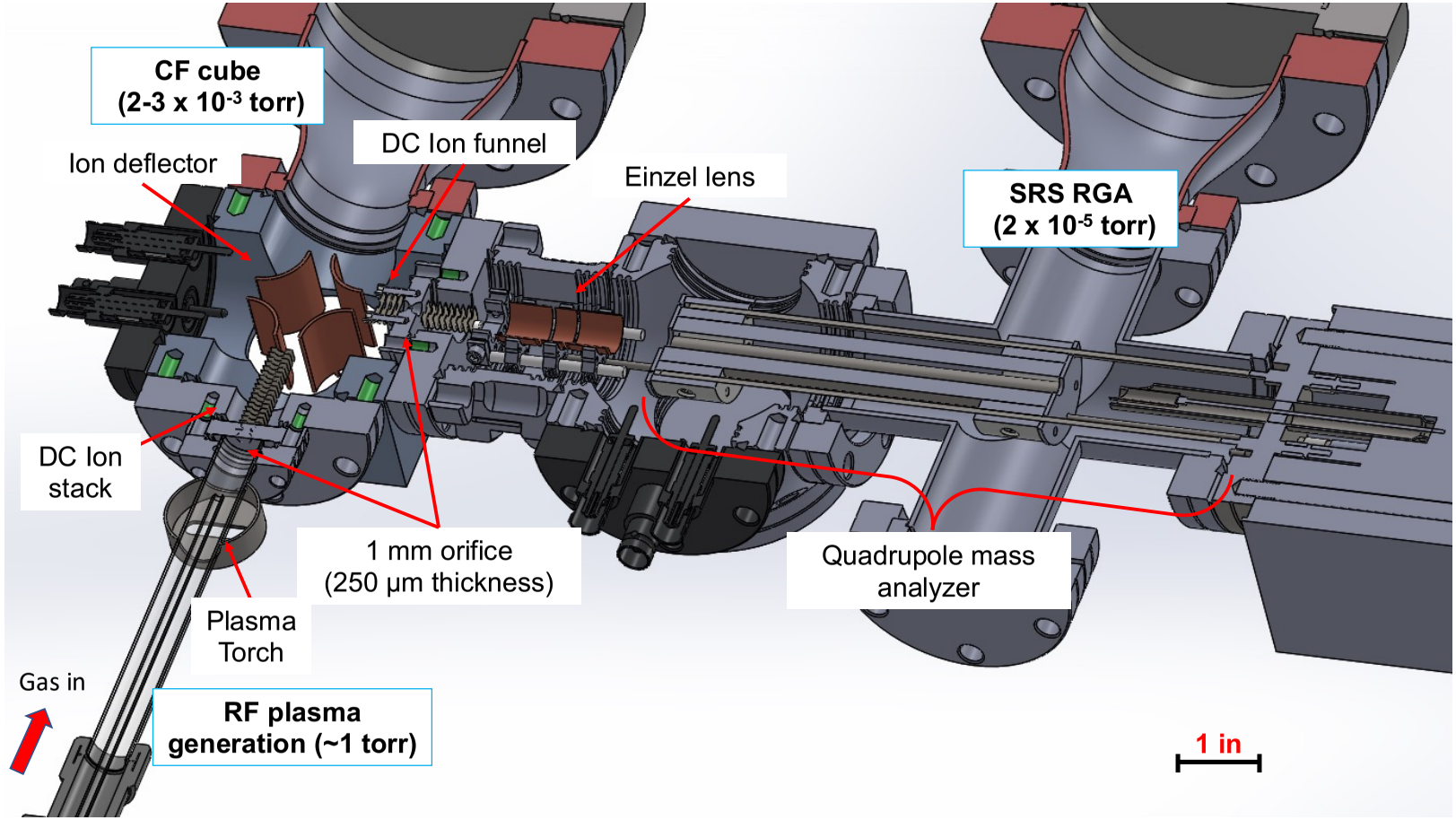

Fig. 5.1: CAD drawing of the full design of the miniature ICPMS prototype. Included is the plasma torch and sample introduction system, interfaced to the mass analyzer via direct current (DC) ion optics and conductance limiting 1-mm apertures. The construction of the prototype instrument followed these initial designs.

differential pressure in the system.

The overall design of the prototype ICPMS uses differential pumping to maintain a pressure gradient across the system, allowing higher gas flow rates into the system while still maintaining vacuum pressure in the mass spectrometer region. Higher gas flow up to 200 mL/min (SCCM, or standard cubic centimeters per minute), is necessary to maintain a torch pressure of <1-13 mbar (1-10 torr, 100-1300 Pa) and deliver ablated geologic material into the plasma system. The instrument is subdivided into three chambers, separated by differential pumping systems and aperture inlets. The main three chambers of the system are as follows:

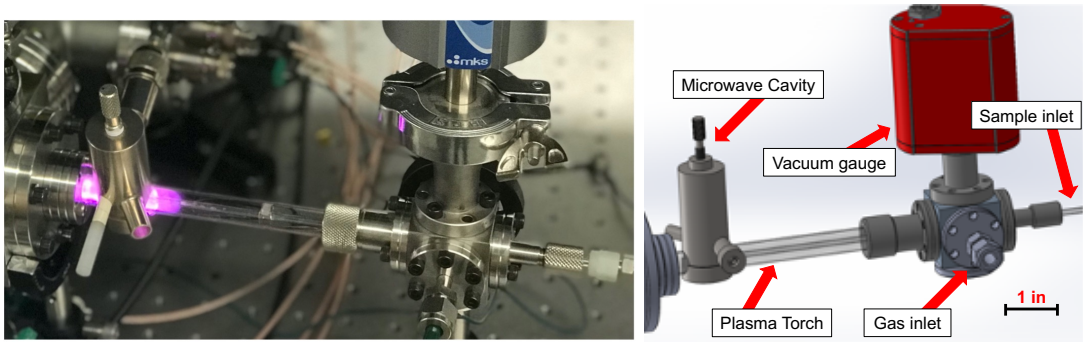

Fig. 5.2: **Left -** Photo of the plasma torch with 10 SCCM of Ar gas flowing, with plasma generated at ∼8 W of forward power. **Right -** CAD model of the plasma front end system, showing similarity between initial design and final product. The torch consists of a series of concentric quartz tubes to constrain the plasma and input sample, a 2.4 GHz microwave cavity to generate the plasma, and a gauge to monitor the pressure in the torch tube.

Plasma torch - The plasma torch consists of a tube of ∼15 cm (6 in) in length, with a 1.25 cm outer diameter (0.5 in) (OD) and a 1 cm inner diameter (ID) (0.375 in), which serve to contain the plasma and sample gas. The torch is constructed of either quartz or alumina for their high temperature tolerance and electrical insulating properties (Fig. 5.2). The torch is interfaced to the following chamber via a 1-mm conductance limiting aperture, producing the pressure gradient between the two chambers. The torch system is not directly interfaced to a pump, but instead the vacuum system on the interface chamber pumps out

the torch through the 1-mm aperture. With gas flow, this maintains a higher pressure in the torch while keeping the pressure lower in the interface.

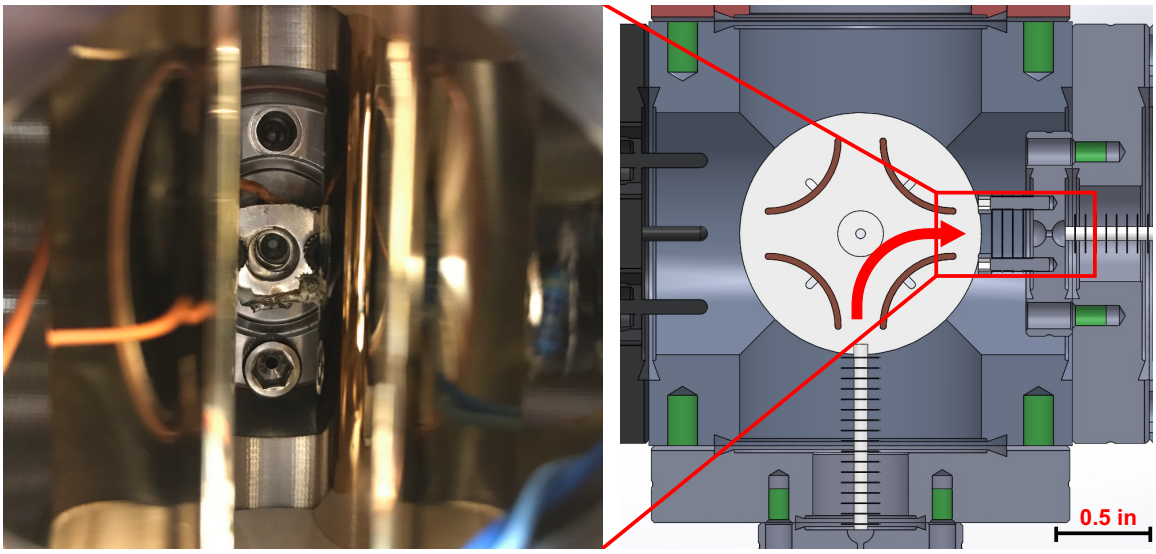

Fig. 5.3: **Left -** Photo of the inside of the interface region looking down the axis of the second 1-mm aperture, orthogonal from the ion source. The 90° deflector plates are seen on either side of the central aperture. **Right -** CAD model birdseye view of the interface region showing the geometry layout of the ion optics and deflector. Ions are deflected from the initial aperture to the right, steering them into the QMA chamber (ion path shown as a curved red line and arrow).

Interface region - The interface region consists of a 7 cm (2.75 in) 6-sided ConFlat^{TM} (CF) cube, which is directly pumped via a turbo pump backed by a roughing pump. The interface region is used to house direct current (DC) ion optics, guiding ions from the torch through the 1-mm aperture into the mass spectrometer. The ions enter into this region via a 1-mm aperture and are immediately columnated by a stack of DC electrodes. A 90° ion deflector is housed after the ion stack, as the photons from a plasma can activate a detector, necessitating an off-axis ion source. This chamber is interfaced to the rest of the mass spectrometer through a DC ion funnel and second 1-mm aperture, limiting conductance and maintaining a differential pressure between this and the final chamber (Fig. 5.3).

Quadrupole mass analyzer region - The quadrupole mass analyzer (Fig. 5.4), capable of separating the ion beam by its mass-to-charge (m/z) ratio of each ion mass, requires low

pressure (10^{-5} - 10^{-6} mbar, 7×10^{-6} – 7×10^{-7} torr, 10^{-3} – 10^{-4} Pa) to operate efficiently and for the detector to avoid saturation. This chamber also consists of ion focusing optics to columnate the beam after exiting the second aperture, followed by an Einzel lens for ion beam focusing. The third chamber which houses the QMA consists of a vacuum cross components 8.9 cm (3.5 in) in length interfaced to another 7 cm (2.75 in) 6-sided ConFlat (CF) cube. The chamber is then interfaced to a second rough pump (0.3 L/s) and turbo pump (60 L/s) system.

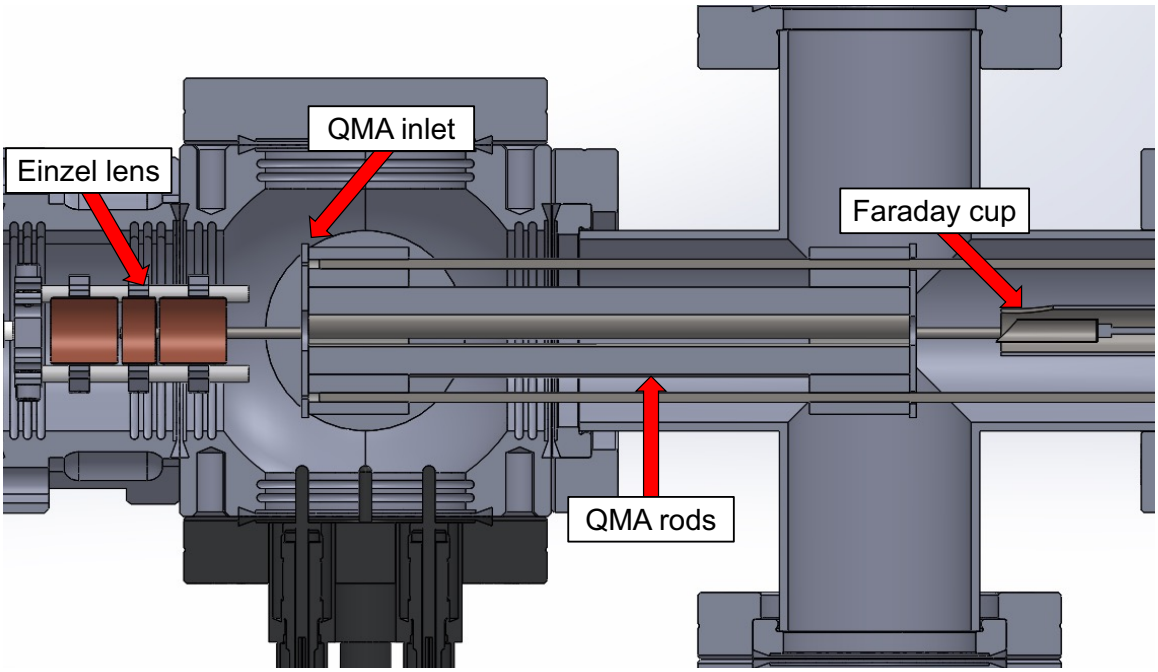

Fig. 5.4: Birdseye view of the CAD model of the QMA region, showing ion optical elements and Einzel lens for focusing ions into the QMA inlet. Ions travel the length of the QMA to the faraday or channel electron multiplier (CEM) detector on the back side of the instrument.

The three components outlined here were tested for their ion transmission efficiency and their ability to hold vacuum under high gas loads.

5.4 Conductance Calculations

Conductance is the ability for gas to flow through a tube with a given length and radius. Conductance calculations are based on two main factors around chamber design: (1.) geometry of vacuum components, and (2.) effective pumping speeds of vacuum pumps. Using these two factors, the final base pressure of the system can be estimated based on chamber conductance with and without input gas flow. To properly estimate the conductance of the chamber as a whole, the calculation strategy is summarized as:

- Determine the conductance of each individual component
- Add all of the conductances depending on the layout of the chamber
- Use the individual chamber conductances to calculate pressure based on effective pumping speed

5.4.1 Individual Component-Level Conductance

Particles entrained in a tube will either travel through the tube unimpeded to the end, collide with other gas molecules, or bounce off of the walls of the tube. The conductance of the tube is dependent on the conductance of the entrance area, which is approximated as an infinitely-thin aperture with the same diameter as the opening of the tube, and the transmission probability through the tube. For a low pressure gas modeled as molecular flow, the conductance (C_{mol}) of a tube is calculated as: [75] and [113]

$$C_{mol} = C_o \cdot P \tag{5.1}$$

where C_o is the conductance of the tube opening (m^3/s) and P is the transmission probability of the gas molecule (*unitless*). C_o is calculated assuming the infinitely thin aperture allows

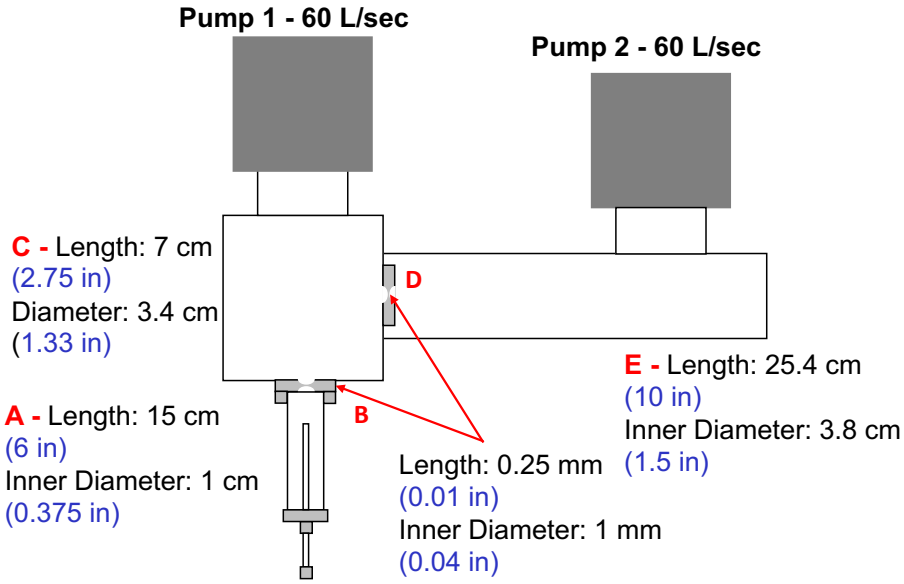

Fig. 5.5: Cartoon diagram showing the dimensions of each chamber component used for conductance calculations.

in gas molecules with a specific efficiency, and is calculated as:

$$C_o = \frac{\nu}{4} A \tag{5.2}$$

Where ν is the average velocity (m/s) of a gas molecule at a certain temperature, and A is the area of the opening (m^2). The probability of a molecule then translating through a tube of a certain length and diameter can be calculated as:

$$P = \frac{4D}{3L} \tag{5.3}$$

Where D and L are the diameter and length of the tube (m), respectively.

Each component of the chamber setup, namely the interface region and the mass spectrometer chamber, are then added together depending on the chamber geometry (Fig. 5.5). The addition of conductances in a vacuum system is analogous to addition of resistors, as the method of addition depends on whether the components are in parallel or series. For

tubes ordered in parallel, the conductances can be added as:

$$C_{tot} = C_1 + C_2 + C_3 + ...C_n \tag{5.4}$$

Where C_n is the total number of individual components in the system. For tubes oriented in series, such as those defining this vacuum chamber, the conductances are added as:

$$\frac{1}{C_{tot}} = \frac{1}{C_1} + \frac{1}{C_2} + \frac{1}{C_3} + ... + \frac{1}{C_n} \tag{5.5}$$

The final addition of all conductances together can then be used to calculate the pressure of each component or of the chamber as a whole.

The plasma torch operates at a higher pressure and gas load than the other chambers, requiring a different approach to the calculation of conductance and pressure in the torch environment. The gradient in pressure leads to a change in gas dynamics, namely a shift from continuum flow to molecular flow. Continuum flow is defined by a high amount of gas particle collisions, where in molecular flow, the mean free path of the gas particle is longer than the chamber diameter. The higher pressure plasma torch chamber is more likely to be in continuous flow than the molecular flow calculations used here, so a different set of relationships is needed to estimate the conductance of the torch environment and are documented at Appendix D. The purpose of this section was to ensure that the QMA and interface chambers would be at sufficiently low pressure to allow ion transmission, thus the torch pressure is ancillary to our considerations in this section.

5.4.2 Results of conductance calculations

Using the framework established above, the conductance of the main components of the instrument were calculated. Each system-level conductance was then used to calculate

the pressure in the system, with consideration of gas flow into each subsystem.

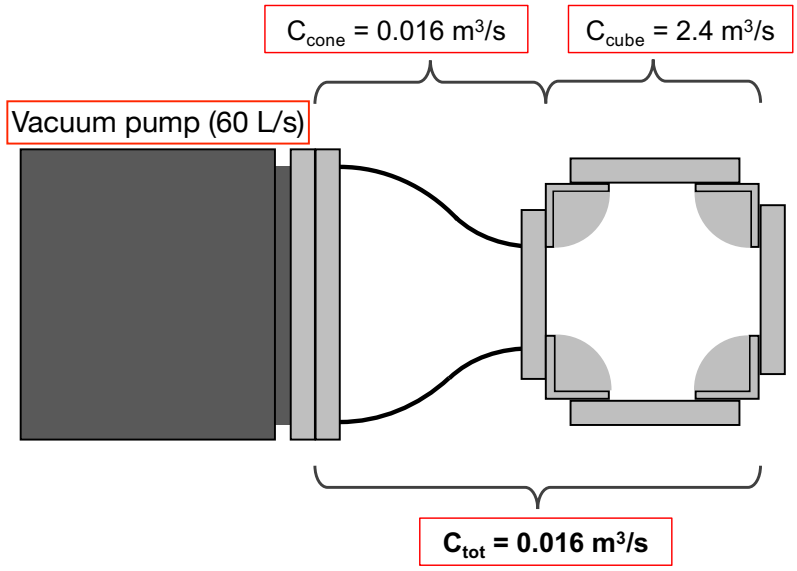

Fig. 5.6: Summary of conductances of individual components comprising the interface region. The conical reducer acts as a conductance limiting component.

The interface region consists of a 7 cm (2.75 in) CF cube, with a 60 L/s turbo pump interfaced via a conical reducer flange (Fig. 5.6). The conductance of the CF cube was calculated assuming a tube-shaped geometry, with a 7.6 cm (3 in) length and a 3.3 cm (1.33 in) inner diameter, giving a conductance of 2.4 m^3/s. The conductance of the conical reducer is dependent on the ratio of both diameters, and is calculated as 0.016 m^3/s. This shows that the conical reducer acts as a conductance limiting component; a larger pump with an increased pumping speed would have minimal effect on the ultimate system pressure. Adding the conductances together in series as $\frac{1}{c_{tot}} = \frac{1}{c_{cone}} + \frac{1}{c_{cube}}$ gives a total conductance of 0.0161 m^3/s or 16 L/s. With a 60 L/s nominal pumping speed and this calculated conductance, this gives an effective pumping speed of 12.7 L/s. See eq. 5.7 for calculation used to estimate effective pumping speed.

The conductance of the QMA system is calculated similarly to the interface region, using a single tube-shaped component interfaced to a 60 L/s turbo pump via a conical

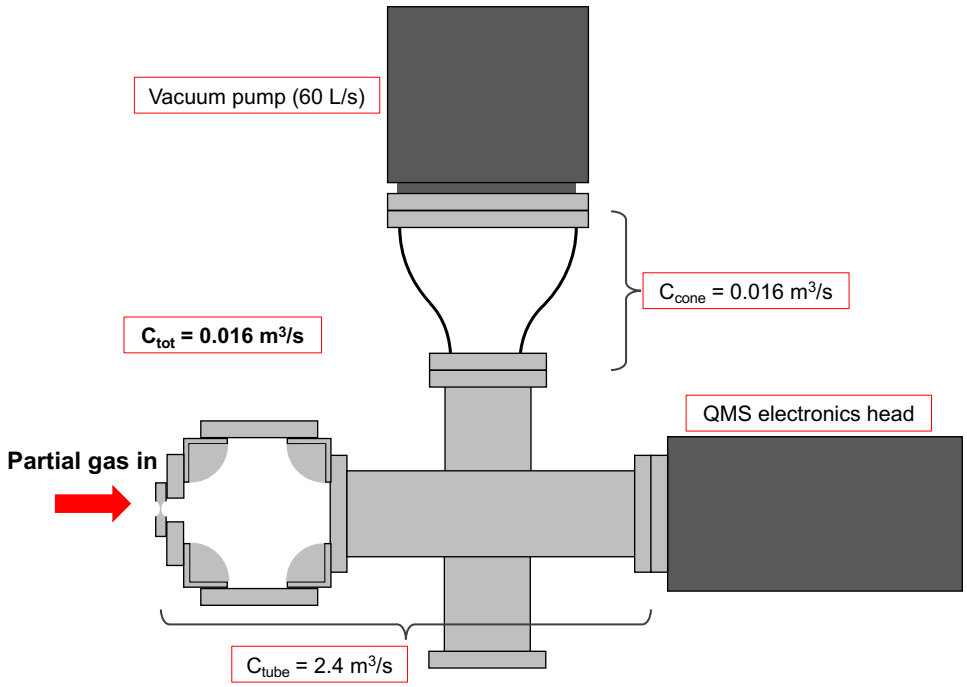

Fig. 5.7: Summary of conductances of individual components comprising the QMA region. The gas inlet is calculated using an estimated pressure in the interface chamber and a 1-mm aperture diameter

reducer (Fig. 5.7). The caveat of this calculation is that gas is being input into the system via the torch, and while some gas is pumped out via the interface turbo, some gas still enters the QMA chamber. If the foreground pressure is already calculated in the interface region, then the flow of gas through an aperture can be estimated as:

$$\text{flow}(\text{cm}^3/\text{s}) = 0.01749 \cdot \frac{P_1}{29.7} \cdot \sqrt{\frac{29}{m_{gas}}} \cdot \sqrt{\frac{528}{T}} \cdot D^2 \tag{5.6}$$

Where P_1 is the pressure in the interface region (PSI), m_{gas} is the atomic weight of the gas molecule (g/mol), T is temperature (K), and D is the aperture diameter (μm) [106]. Using eq. 5.6, with a calculated pressure of 3×10^{-4} mbar (2.2×10^{-4} torr, 3×10^{-2} Pa, 4.4×10^{-6} PSI), an assumed gas temperature of 500 K, an aperture diameter of 1,000 μm, and an Ar molecular weight of 40 g/mol, the flow was estimated to be 0.0023 cm^3/s (0.135 SCCM)

entering through the aperture. The remainder of the gas is pumped away by the first turbo pump. The gas flow calculated here may be used to calculate the final base pressure in the QMA chamber.

As the inner diameter of the tube is the same as that of the CF cube, as well as the same dimensions of the conical reducer, the conductance of the QMA region is effectively the same as the interface region of 0.016 m^3/s with an effective pumping speed of 12.7 L/s.

5.4.3 Chamber Pressure Calculation

The pressure in a system is driven by a balance between gas that is input into the system and gas that leaves the system through pumping. To accurately estimate the system pressure in each chamber, the effective pumping speed in each chamber is calculated as:

$$\frac{1}{S_{eff}} = \frac{1}{S_{nom}} \cdot \frac{1}{C} \tag{5.7}$$

Where S_{eff} is the effective pumping speed in the chamber, S_{nom} is the nominal pumping speed, and C is the conductance of the chamber (L/s). Finally, using the calculated effective pumping speed of each chamber, the pressure in each chamber is calculated as:

$$P_{avg} = \frac{q}{S_{eff}} \cdot \frac{Q_{gas}}{S_{eff}} \tag{5.8}$$

Where q is the internal outgassing rate and Q_{gas} is the input gas flow rate (mbar $\cdot$ L/s).

Given the above calculations for pressure and the individual chamber conductances, the pressure was then calculated in each chamber. These calculations were also carried out with and without Ar gas flow at 10 SCCM to observe the difference in chamber pressure.

With the gas flow off, the base pressure of the chamber was calculated to be high vacuum conditions in the QMA and interface regions at 10^{-6} mbar (1.5×10^{-6} torr, 10^{-4} Pa).

With the gas flow on, the interface region was found to be 10^{-3} mbar (7.5×10^{-4} torr, 0.1 Pa), and 10^{-5} mbar in the QMA region (7.5×10^{-6} torr, 10^{-3} Pa). This pressure gradient is sufficient to deliver ions to the mass spectrometer.

After the CAD models and pumping calculations were carried out, the system was constructed according to the planned system design. Because the calculations were based on the planned design and pumping system, the observed pressures in each subsystem can be compared to the calculated pressure. The system pressures were observed as 5×10^{-3} mbar (3.7×10^{-3} torr, 0.5 Pa) in the interface region, and 3×10^{-5} mbar (2.2×10^{-5} torr, 3×10^{-3} Pa) in the QMA region with gas flow on. With gas flow off, the base pressure of both the QMA and interface region were observed at 2×10^{-7} mbar (1.3×10^{-7} torr, 2×10^{-5} Pa). These observations are close to the calculated values, giving confidence to the approach taken here.

5.5 Ion Current Measurements

The housing and ion optics designed via CAD modeling, shown above (Fig. 5.1), were constructed during a progressive chamber buildup campaign. The RF plasma generated by the ionization of Ar gas was used as the source of ions for the buildup. The effort to construct the instrument was performed as a piecemeal approach, integrating a single new ion optic element and optimizing its ion current throughput before installing, testing, and optimizing the next electrode. The buildup proceeded this way until the ion beam was integrated with the QMA, and ^{40}Ar measurement was observed in a mass spectrum. See Appendix D for photos and more on the chamber construction.

The ion optics shown previously can perform two main functions in developing the ion transmission efficiency of the instrument: (1.) The electrodes can produce an electric field, shaping and bending the trajectory of the ion beam, and (2.) the optics can be connected to

an ammeter, which measures the intensity of ion current directed onto the electrode. These two functions allow tunability of the system, where the voltage applied to each electrode can be optimized to maximize the amount of current delivered.

This section outlines a series of experiments documenting the ion current measured at each electrode throughout the instrument. The ion current in the system was measured using a Keysight B2985A ammeter, with a dynamic range of 1 mA to 0.01 fA. This ammeter was used to measure plasma ion current at each electrode in the instrument, including the plasma, via CF electrical feedthrough ports. As the current at each electrode is dependent on the efficiency of ion transmission, which itself is dependent on the electric field inside the system, the current measured is commonly plotted against the applied voltage of the previous electrode. After the current was maximized on a certain electrode, the ammeter was moved to the next electrode downstream, and the process was repeated until the entire system was optimized. This method used the "follow the ions" approach to optimization, documenting the incremental loss of ions throughout the system while still maximizing transmission.

5.5.1 Front end – Plasma and Aperture

In order to quantify the gain/loss of ions throughout the instrument, an initial characterization of the plasma is necessary. By understanding the plasma environment at its source, a better understanding of the changes in the ion beam further downstream was established. The initial plasma measurements were conducted by connecting the ammeter to a wire inside the plasma. While these measurements were conducted with a single wire inside the plasma environment, a more comprehensive evaluation of the plasma ion current was carried out at chapter 4.

One of the most important first steps of using plasma ion sources is the separation of

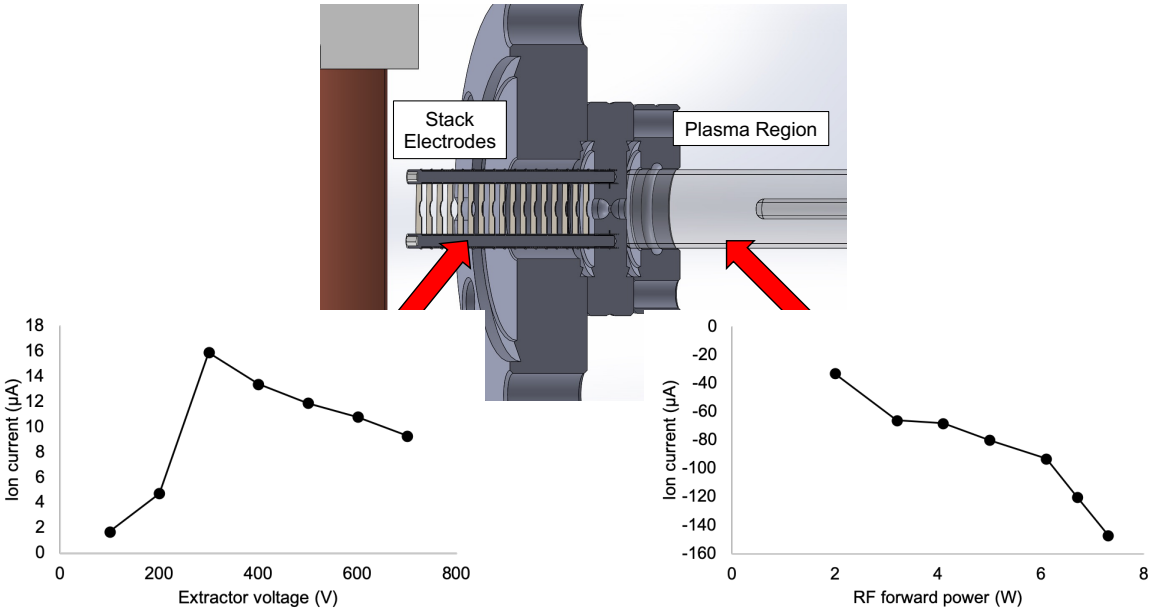

Fig. 5.8: **Above -** CAD drawing of the ion lens stack and the plasma torch, interfaced by a 1-mm aperture. The plasma ion current was measured on the torch side of the aperture using an input wire (**Right**), and then measured on the vacuum side of the aperture on the extractor stack (**Left**). The first extractor lens is electrically isolated from the rest of the stack, acting as an independent parameter.

ions from electrons. Initial measurements of the plasma current show a large negative current in the range of -100's of μA in the central portion of the plasma, indicating a large electron population in the plasma. Typical plasma measurements involving a Langmuir probe (see chapter 4, Fig. 4.5) require the plasma to be surrounded by a grounded sheath to reduce the electrons for a more accurate analysis. A non-conductive quartz or alumina tube is used in this setup, which does not sufficiently ground the plasma and allows a larger electron population than in grounded torch tubes. However, as the plasma leaves the initial 1-mm aperture, it interacts with the grounded aperture and the electron population is reduced. Further, a positive potential on the first focusing electrode separates the plasma by diverting electrons away from the field and focusing positive ions towards the ion stack. The initially high electron population is evidenced by the $\sim$-3 μA current observed on the first electrode after the first 1-mm aperture, with no voltages applied to the extractor or stack

electrodes. Here, the unfiltered plasma makes it through the aperture via gas dynamics. The electron population is relatively higher than the ion population in the plasma, driving the overall current negative. The current then increases significantly and becomes positive due to the removal of the electrons and focusing of the ions.

In traditional ICPMS systems, the high ion and electron population from the plasma is separated by a grounded skimmer cone, which effectively removes electrons from the plasma and delivers ions to the mass analyzer. The ions coming through the inlet aperture initially experience a high negative potential ($>$ -1 kV) as an "extractor", which pulls the positively charged ions from the cone system and gives them a high initial kinetic energy. In comparison, our setup uses a intermediate initial positive voltage (+100s of V), followed by a longer stack of positive electrodes ($\sim$ +1 kV) to columnate and focus the beam leaving the first aperture and deliver the ions to the next stage of the ion optics. The ion stack was also optimized for its performance.

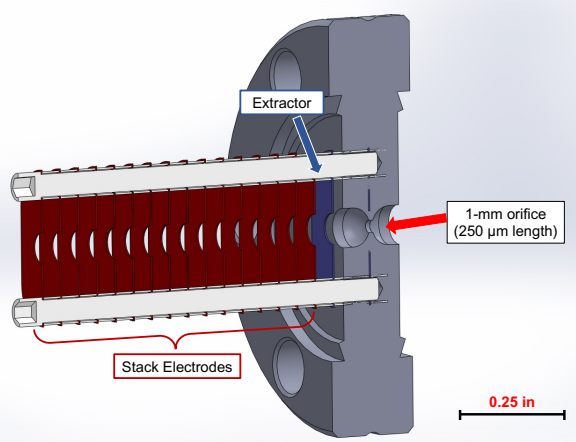

Fig. 5.9: CAD model of the first lens stack and 1-mm aperture. The first electrode in the stack is electrically isolated from the rest of the stack, and controlled by a separate voltage. The rest of the stack is separated by resistors, and a single voltage is applied to the second electrode in the stack.

5.5.2 First ion stack

The first stack of electrodes relies on two main voltages that control the ion population coming from the aperture (Fig. 5.9). The first is the extractor voltage, which separates the ions from the electrons and focuses the ion beam, and the second is the lens stack, which delivers the ions through the relatively high pressure environment to the 90° deflector. The

ion stack and the extractor work in tandem to provide the optimal focusing and ion trajectory confinement to properly deliver the ions, so both elements must be tuned together.

For the optimization experiments, the 90° deflector was positioned at a 45° offset from its normal position so that the front plate was situated directly in front of the lens stack, acting as the collector plate for ion current. The ion current was measured as a function of changing extractor and stack voltages by setting the extractor to a constant voltage, then sweeping through voltages on the stack up to 1 kV. Measurements are repeated at 100 V steps until the extractor reaches 1 kV.

This method of tuning two separate voltages to find an optimized combination produces a three-component set of data, with the two input voltages on the x and y axes and the measured current on the z axis (Fig. 5.10). To maximize ion current onto the collector plate, the optimal combination of voltages is to use a low potential (+400 to +500 V) as the initial extractor lens, followed by a higher potential (+900 to +1000 V) on the lens stack.

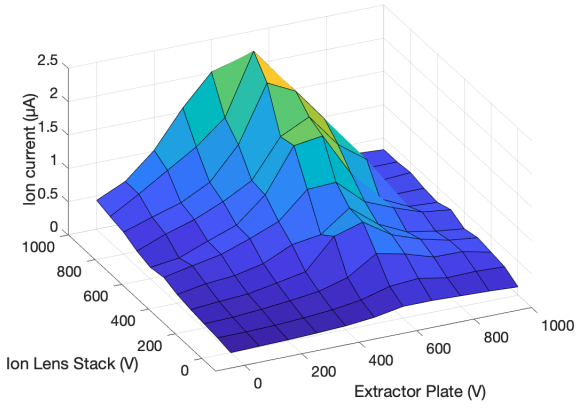

Fig. 5.10: 3D plot of the measured ion current generated by voltage tuning of the first lens stack. As the first electrode is isolated from the rest of the stack, the two voltage inputs can be manipulated to find the optimal combination.

In typical commercial ICPMS systems, the ion beam first experiences a high negative potential (> -1 kV), which provides a large initial kinetic energy to the ions as they exit the skimmer cone aperture. Experiments showed that a range of negative potentials had a detrimental effect on the magnitude of the ion beam, effectively cutting off transmission. Instead, the first ion lens stack operates more effectively at a positive polarity. Thus a low initial positive potential was used for focusing, rather than a high initial negative potential for extraction and kinetic energy.

5.5.3 90° Deflector

After optimizing the first lens stack, the 90° deflector is the next downstream ion optic requiring optimization. The purpose of this component is to turn the plasma ion source off-axis from the QMA detector, as the photons and metastable (non ionized, but at an excited energy state) species from the plasma can also be directed into the detector, flooding the signal. A plasma ion source that is off axis from the detector of the mass spectrometer allows for separation of the ion population from the metastable and photon populations.

A similar approach to the ion lens stack was taken to monitor the transmission efficiency of the 90° deflector. The deflector consists of two separate ion optical components working in tandem, with opposite deflector plates using opposite polarity potentials to drive the ion beam at a right angle (Fig. 5.11). This experiment was set up using two electrical feedthroughs, installed on opposite sides of a CF cube with the 90° deflector in the middle. On each feedthrough, a nickel strip was installed onto the connector pin, which acted as a collector plate for the ion beam and registered the beam current (see Appendix D for photos of the setup).

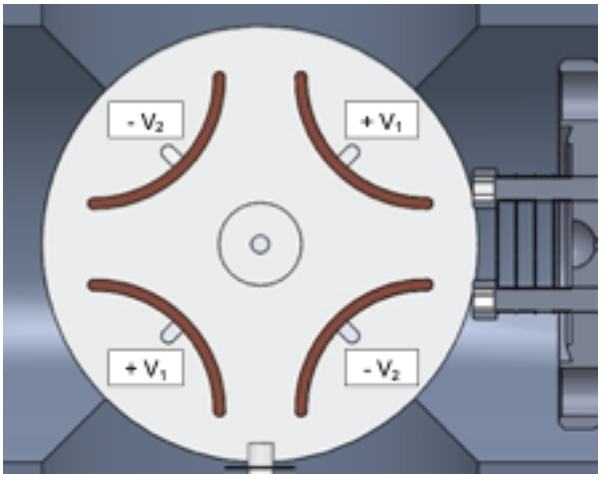

Fig. 5.11: Birdseye view of a CAD model of the 90° deflector. Each opposite pair of plates is connected to a single voltage of the opposite polarity of the adjacent plates.

Because the collector plates were installed on both sides of the deflector, the deflector has the ability to shift the ion beam either to the left or the right without any mechanical changes. Instead, switching the direction of the ion beam only requires a flipping of the polarity between two opposite rod pairs. Here, I carried out a systematic scan of the

combination of the two potentials to deliver the optimal ion beam after the deflector. The positive deflector plates were kept at a constant voltage, while the negative polarity was swept through 0 – 1 kV at 100 V steps, at which point the positive deflector plate was increased by 100 V and the process repeated. This systematic sweeping of voltages produced a 3D plot of ion current as a function of the two voltage combinations, analogous to the ion stack experiments (Fig. 5.12, 5.13). The experiment was repeated to collect the optimization data for both the right and left bend.

Data collected over this range of voltage combinations shows a characteristic "Ridge of Stability", in which the highest ion current changes little over a specific range of voltage combinations, while dropping off drastically at deviations from the optimal combination. These data confirms that the 90° deflector operates as designed, as opposite polarity voltages can direct the ion beam to the desired collector plate. The ion current measured on the opposite side of the intended deflection (i.e. the right side current when polarity bends the beam to the left) is typically $\sim$200$\times$ lower than the ion current on the deflected side, indicating that some ions do stray from the beam profile, but that the deflector efficiently deflects the ions in the intended direction.

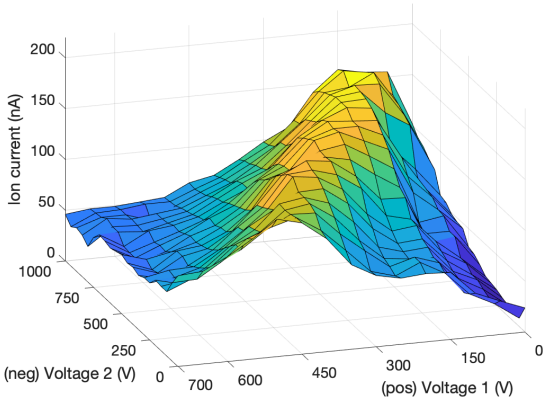

Fig. 5.12: Results of 90° deflector optimization experiments, with ion beam bending to the left away from the QMA.

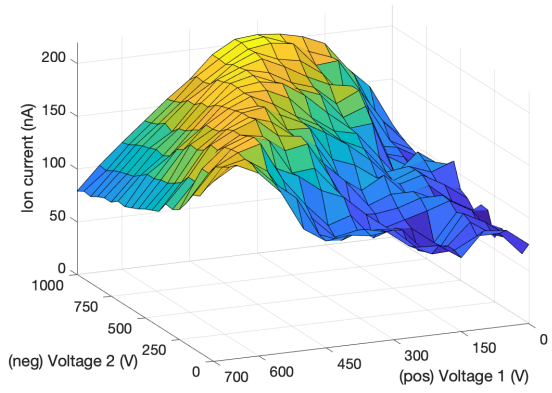

Fig. 5.13: Results of 90° deflector optimization experiments, with ion beam bending to the right towards the QMA.

Asymmetry is seen between the two optimization plots, in which the right bend peaks at ∼220 nA and shows a broader range of stability, while the left bend peaks at ∼170 nA, with a narrower ridge. The asymmetry is likely due to a slight off-axis bend in the initial ion stack, which preferentially diverts ions to one side. The second 1-mm aperture leading to the QMA region is situated on the right side of the cube, so this asymmetry is beneficial to the setup. The previous experiments on ion stack transmission efficiency revealed a peak ion current of ∼2.3 μA measured going into the deflector, and the peak current measured at ∼220 nA, which gives a bend efficiency of ∼10%. The deflector described here is less efficient than previously published deflector efficiencies (70-80%) [124], possibly due to the larger bend radius (designed for 2.75" CF cube) or more likely the higher pressure in the system (2×10^{-3} mbar, 1.5×10^{-3} torr, 0.2 Pa).

5.5.4 QMA chamber – second aperture

The 90° deflector is interfaced to the QMA via a second, 1-mm aperture for differential pumping and pressure regulation, as well as a DC ion funnel to shape and deliver the ion beam (Fig. 5.14). One of the main challenges of a differentially pumped system is the use of apertures to maintain a pressure gradient. At each of these junctures, the ion current can be cut off by a significant amount due to the limited transmission area. Here, I document the capability for beam steering via the 90° deflector through the second aperture into the QMA region.

The main goal of the interface region is to allow as many ions to pass through as possible into the QMA chamber. Previous experiments show the tunability of the 90° deflector to maximize ion transmission via tunable voltages, and this tactic was taken for these experiments as well. Prior to the analysis, a series of lenses was installed onto the second aperture to focus the bent ion beam through the aperture via DC electric fields. A nickel strip was

mounted on the backside of the aperture plate, with the ion current measured through a CF electrical feedthrough (see appendix D for photos). This chamber is differentially pumped via a second turbo pump on the back side of the second aperture, allowing a low pressure (10^{-5} – 10^{-6} mbar, 7×10^{-6} – 7×10^{-7} torr, 10^{-3} – 10^{-4} Pa) to be maintained even with plasma gas flowing into the system.

The focusing electrodes on the front end of the aperture were first optimized to allow in the maximum ion current at a set deflector voltage, and then kept constant throughout the duration of the experiments, leaving these two electrodes optimized in the deflector experiments. Once the initial stack and the second focusing electrodes are brought to their optimal values, a similar sweep of positive and negative potentials was carried out on the 90° deflector. This experiment demonstrates beam steering through the aperture using the deflector component, which is important for alignment with the focusing Einzel lens and QMA.

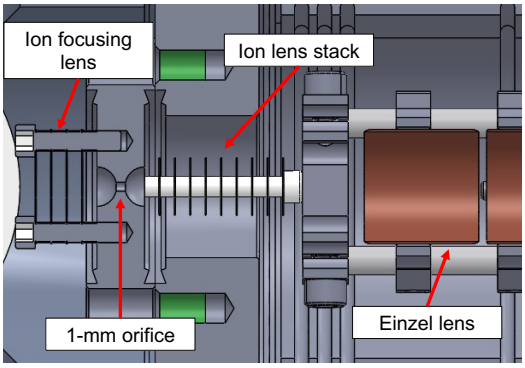

Fig. 5.14: CAD model of the aperture joining the interface region to the QMA region, with accompanying ion lens stacks and Einzel lens.

The ion current measured through the aperture demonstrates a similar Ridge of Stability as seen on the initial deflector experiments (Fig. 5.15). Reproducibility of the Ridge of Stability indicates that the 90° deflector maintains the capability to steer the beam to center onto the second aperture, which then gets focused via the focusing electrodes. The 3D plot shows a peak of ion current at $\sim$ 4 nA, a loss of $\sim$50x ion current via the aperture, highlighting the tradeoff between differential pumping and ion beam intensity. Future updates could replace the flange with a larger aperture to allow more ions to pass through, or electrically isolate that component and apply a voltage to limit ion loss.

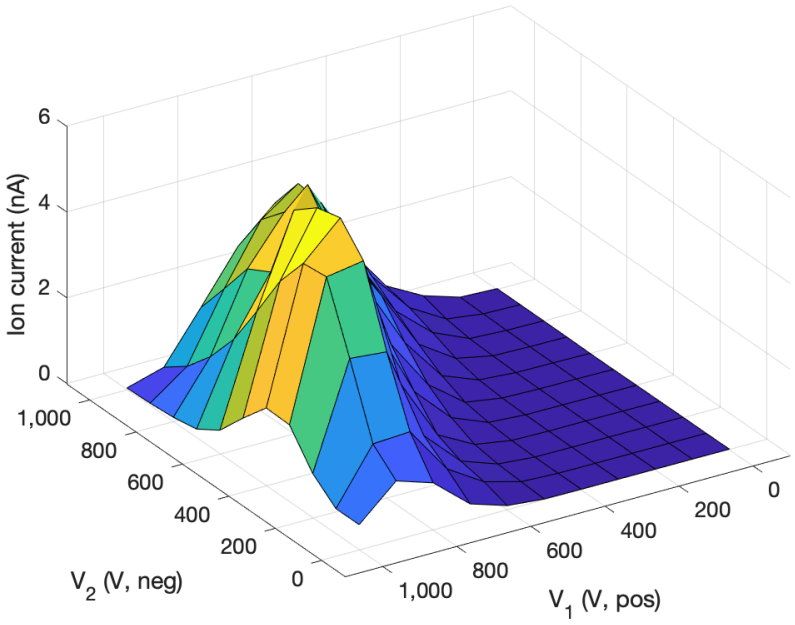

Fig. 5.15: Results of 90° deflector optimization experiments with ion beam measured after second aperture. Ion current intensity shows the same characteristic Ridge of Stability as before the aperture.

5.5.5 Ion measurement on the QMA

The final portion of the instrument includes the quadrupole mass analyzer, as well as a series of DC ion optics to focus the beam into the mass spectrometer. The QMA used here is a Stanford Research Systems Residual Gas Analyzer (SRS RGA200), which has a mass range up to m/z = 200 and a signal dynamic range of $\sim 10^9$ (10^{-15} – 10^{-6} A). The previous efforts of ion transmission efficiency were designed to deliver as much of the ion beam to the mass analyzer as possible, maximizing the ion signal of the analyte. Here, the ion beam from the previous optimization campaign is measured by the QMA faraday cup, to show the ability to deliver ions from the plasma to the mass analyzer and to construct the complete ICPMS instrument (Fig. 5.16).

The SRS RGA has multiple ways to measure sample ions. First, the QMA has two separate ion detectors; the faraday cup, which measures direct ion beam current, and the

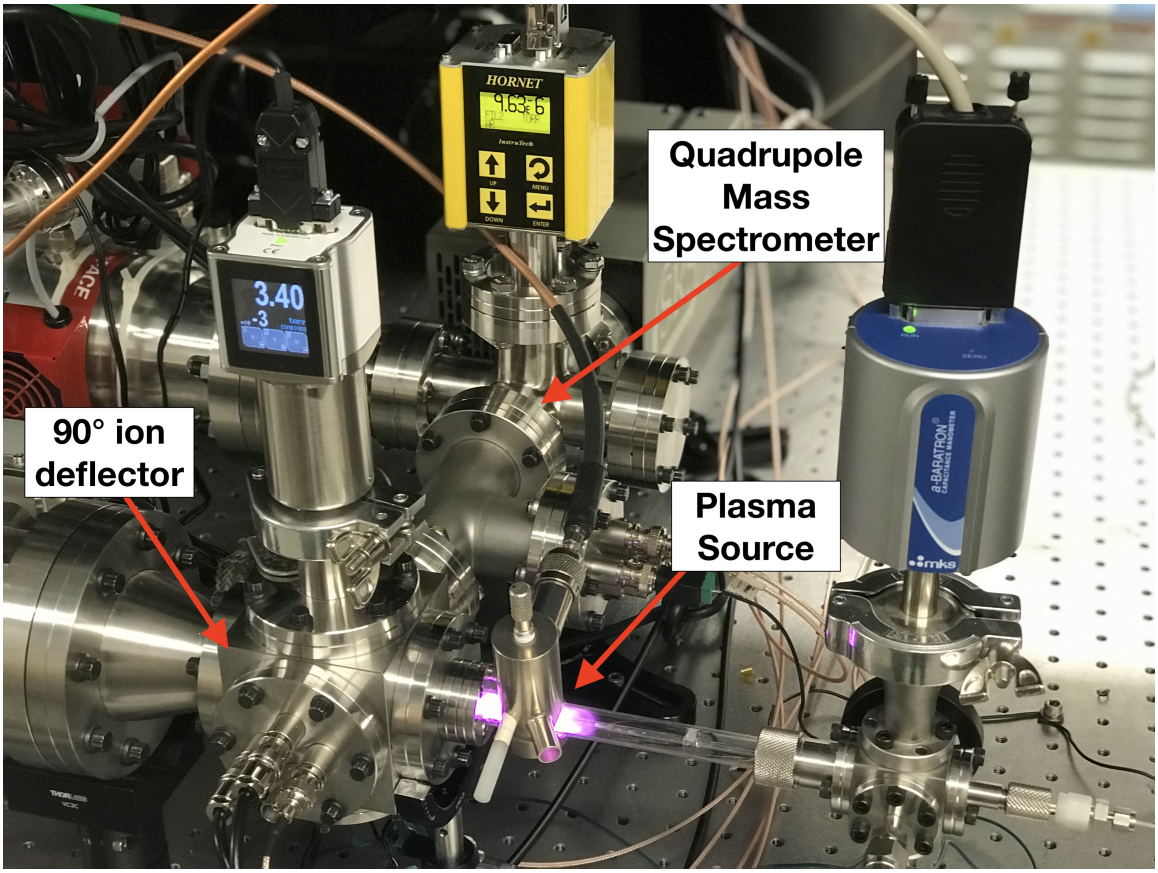

Fig. 5.16: Photo of the completed mini ICPMS setup in operation.

channeltron electron multiplier (CEM), which amplifies the signal via electron cascading. The QMA has the ability to scan across a range off masses, producing a spectrum, or it can select specific masses and measure that mass signal intensity as a function of time, known as a chromatogram. The experiment carried out here involved an initial optimization campaign, in which the ion beam was filtered for the Ar (m/z = 40) mass and intensity maximized on the faraday cup by applying the previously optimized voltages and adjusting the beam focusing via the Einzel lens. Once the ion beam reached its maximum, the QMA was switched to spectrum mode to measure the full spectrum of ion masses.

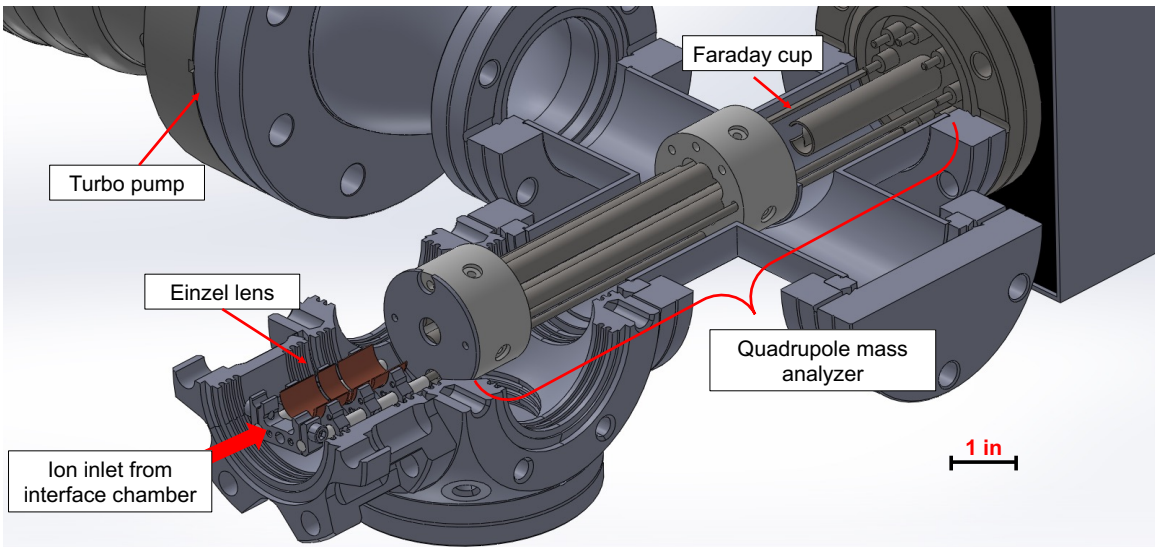

Fig. 5.17: CAD model of the major components of the QMA region, detailing the mass analyzer and Einzel lens focusing electrode.

5.5.5.1 Ar ion beam

The development campaign of the mass spectrometer resulted in a beam of Ar^+ ions traveling through the interface region via the 90° deflector and being focused through the 1-mm aperture into the second, differentially pumped chamber. The ions were focused into the QMA via the Einzel lens and a spectrum was acquired. The spectrum revealed the Ar

ion beam, at m/z = 40 and m/z = 20, measuring the $^{40}Ar^{+}$ and $^{40}Ar^{2+}$ ion populations. A time-dependent scan of the Ar ion beam showed a mean ion current of 3.39 $\pm$ 0.14 pA (4.2% 1σ), $\sim 10^{3}\times$ lower than the current measured on the backside of the second 1-mm aperture.

The reason for this major loss of ions could potentially be from the long travel distance ($\sim$25 cm, 10 in) the ions are required to travel between the aperture inlet and the faraday cup. At a pressure of $\sim 2\times 10^{-5}$ mbar (10^{-5} torr, 2×10^{-3} Pa), this pressure is high enough to cause ion-neutral collisions even with DC and RF voltages constraining the ion path. Thus, increasing the pumping capacity or reducing the plasma gas flow into the system can significantly increase ion transmission efficiency and analyte signal.

The QMA faraday cup can act as an ion current measurement device similar to the Keysight ammeter, so a set of experiments similar to those previously performed on the deflector, in which the two voltages on the the 90° deflector were systematically varied in tandem, was carried out on the QMA. Here, all the voltages in the system were set to their optimal values and the mass spectrum was taken as a baseline, and then the 90° deflector voltages were returned to 0 V. Another experiment sweeping through the positive and negative deflector potentials was carried out to observe the behavior of the full system in response to this component, and to show the ability for beam steering into the QMA. Because the QMA has the ability to selectively measure individual mass peaks over time, the deflector tuning was repeated with only the $^{40}Ar^{+}$ ions selected.

These results show the characteristic Ridge of Stability as seen on previous iterations of this experiment is reproducible on the QMA itself, verifying the ability to steer the ion beam from the previous chamber and demonstrating the reproducibility of this phenomenon (Fig. 5.18). In addition to the high ion currents along the characteristic ridge, $^{40}Ar^{+}$ ions were also observed on the QMA detector when the deflector voltages were off, although other ion focusing electrodes were at their optimal voltages. The electric field produced by

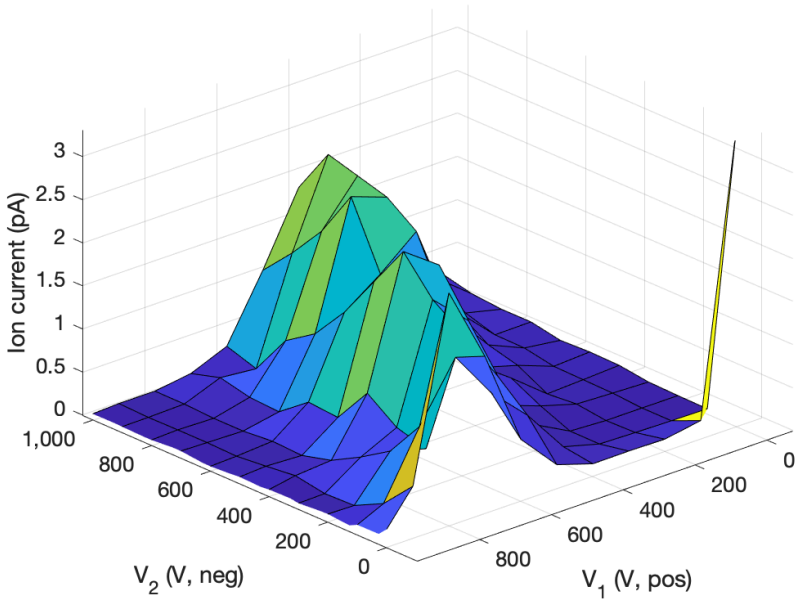

Fig. 5.18: Results of 90° deflector experiments, measured as $^{40}Ar^{+}$ ions via the QMA on the faraday cup detector.

the deflector does influence the ion beam trajectory, but ion drift due to gas flow could be delivering ions into the QMA chamber as well.

5.5.5.2 Peak shaping

Because the Ridge of Stability shows the range of voltage combinations that deliver ions to the QMA, the signal produced on the QMA by taking mass spectra across that identified range of voltages was explored further. The shape of the peak is an important metric in mass spectrometry, as the peak shape reflects the ion beam packet coming to the analyzer, and by extension the quality of the beam shaping electrodes. The peak shape can drive uncertainty in the system, as the mass accuracy of the peak can drift due to improper focusing or high ion energy.

Initial measurements of peak shape employed a high negative potential and low positive potential (V_1^+ = +275 V, V_2^- = -755 V), as this combination typically produced the highest

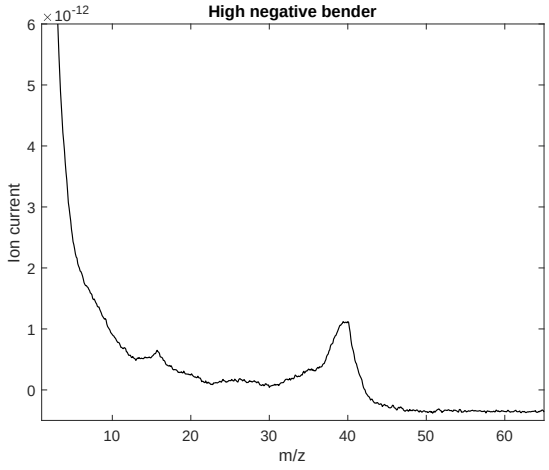

Fig. 5.19: Initial mass scan showing high background signal and a wide ^{40}Ar peak, likely due to a large population of ions with high kinetic energy. Generated with +275 V positive and -755 V negative deflector voltages.

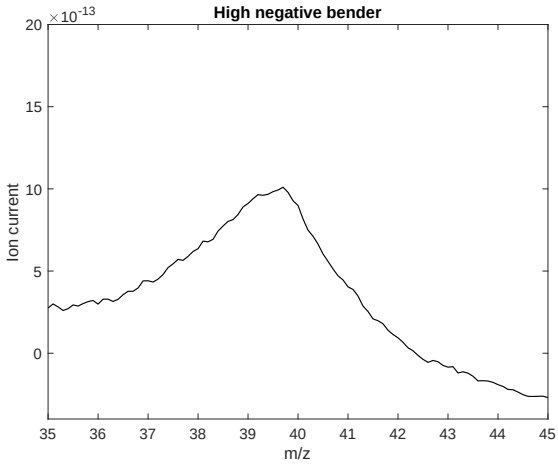

Fig. 5.20: Zoom in on Ar mass. High ion kinetic energy makes the peak spread out over ∼5 amu. The baseline likely turns to negative current after the ^{40}Ar peak due to secondary electron generation in the faraday cup from high kinetic energy ion impacts.

beam current on the collector electrodes and on the QMA faraday cup. This combination produced a wide peak with a base that covered ∼5 amu, as well as a high background signal, indicating that a high negative potential distorts the peak shape (Fig. 5.19, 5.20). By changing to a high positive potential and no voltage applied to the negative electrode (V_1+ = +800 V, V_2- = 0 V), the peak becomes narrower with a lower background signal ((Fig. 5.21, 5.22). Both peaks have a leading low mass edge to their peak shape, indicating a curved, non-uniform packet of ions.

The peak shape is a gauge of the ion beam, both its spread in 2-dimensional space but also in energy. An ion beam that has a high energy imparted onto it through a high voltage, for example through the +1 kV extractor stack, will produce a peak with a wide base. The peaks shown above have bases that range from m/z = 36 to 41, indicating that the high potential that is used to deliver the ions to the mass spectrometer produces a beam with excessively high kinetic energy. Further, ions with high kinetic energy can produce

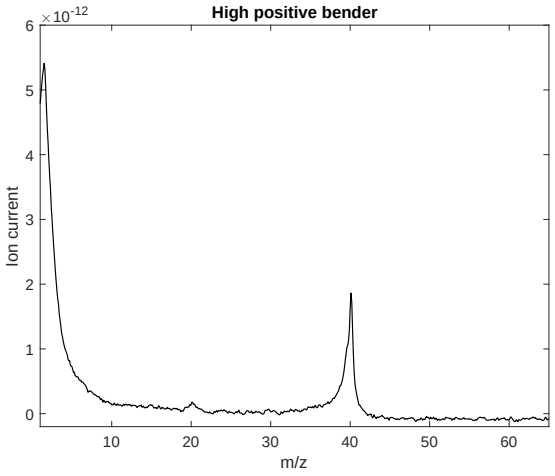

Fig. 5.21: Tuned mass scan with +800 V positive and 0 V negative deflector voltage. This reduction in negative potential reduces the kinetic energy spread of the ions, resulting in a narrower peak and a lower background baseline.

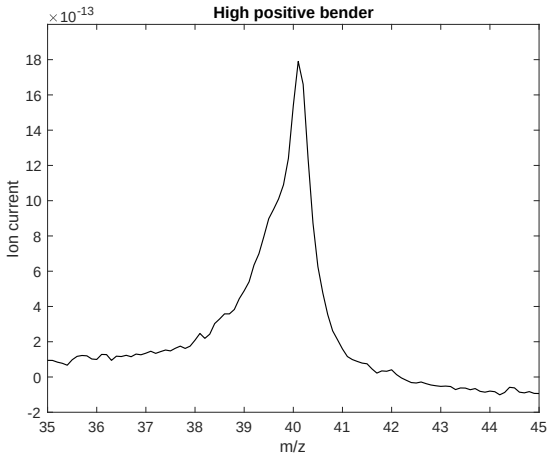

Fig. 5.22: $^{40}Ar^{+}$ peak after tuning the 90° deflector. Peak still has a wide base on the low mass side of the peak, covering ∼3 amu.

secondary electrons when they strike the faraday cup. This high population of secondary electrons produced a high negative background signal after the Ar peak, and ions with masses higher than m/z = 40 have been observed to produce peaks with negative current.

To mitigate the issue of high energy required for ion transmission, the second aperture was replaced with a larger (2.5 mm, 0.1 in), electrically isolated aperture that allowed more ions through to the second chamber. This higher ion transmission efficiency allowed the initial stack voltages to be lowered, thus reducing the initial kinetic energy of the ion beam. This low-potential electrical setup produced an ion beam with a narrower peak shape and lower background level, likely due to the dampening of ion kinetic energy (Fig. 5.23, 5.24). While the larger aperture allowed more ions through to the QMA chamber, it also reduced the differential pumping potential, bringing the QMA chamber pressure to $\sim 8\times10^{-5}$ mbar (6×10^{-5} torr, 8×10^{-3} Pa). Despite the higher chamber pressure, this is the most desirable peak shape for future analyses, as it delivers 1 amu resolution to the observed ion signal.

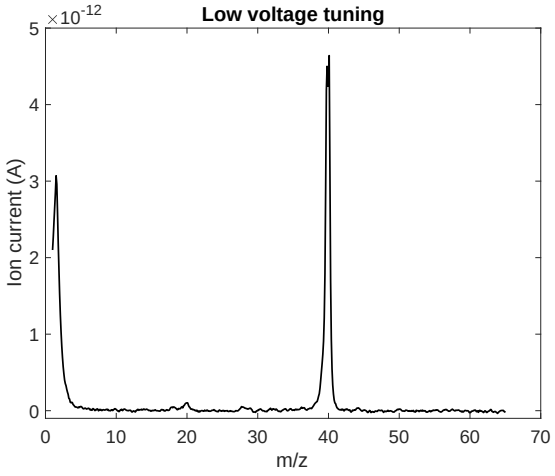

Fig. 5.23: After replacing the second aperture with a 2.5-mm aperture, lower voltages can be used to deliver low kinetic energy ions to the mass spectrometer.

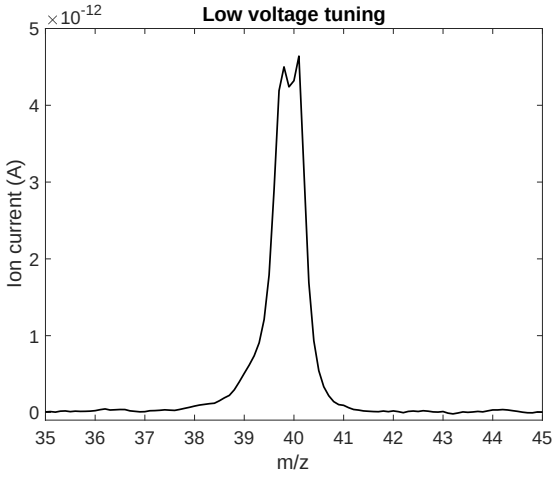

Fig. 5.24: ^{40}Ar peak tuned with lower kinetic energy reduces the spread to 1 amu peak resolution.

5.5.6 Sample Introduction

Once the ion beam has been properly tuned resulting in a unit resolution peak, and the ion current reaching the detector is at its maximum while still retaining the peak shape, then the sample can be introduced into the instrument. Sample input relies on a quartz tube with a 3.2 mm (0.125 in) OD and a 1 mm (0.047 in) ID that is concentric to the plasma tube, with the back end attached to a Kr gas cylinder via a capillary tube. The gas inlet is controlled by a mass flow controller, allowing low gas flow as low as 0.01 mL/min to be introduced into the plasma. From here, the introduced sample can be ionized and analyzed via the mass spectrometer. A noble gas was selected as the first analyte to be measured via this instrument due to ease of sample introduction, its natural state as a mono-atomic species, and its diagnostic isotopic abundances. Kr has five naturally occurring major isotopes with abundances within an order of magnitude of each other, leading to relative ease of isotope ratio measurement due to limited dynamic range capabilities on the instrument.

In order to demonstrate the analytical capability of the instrument, a sample of Kr was

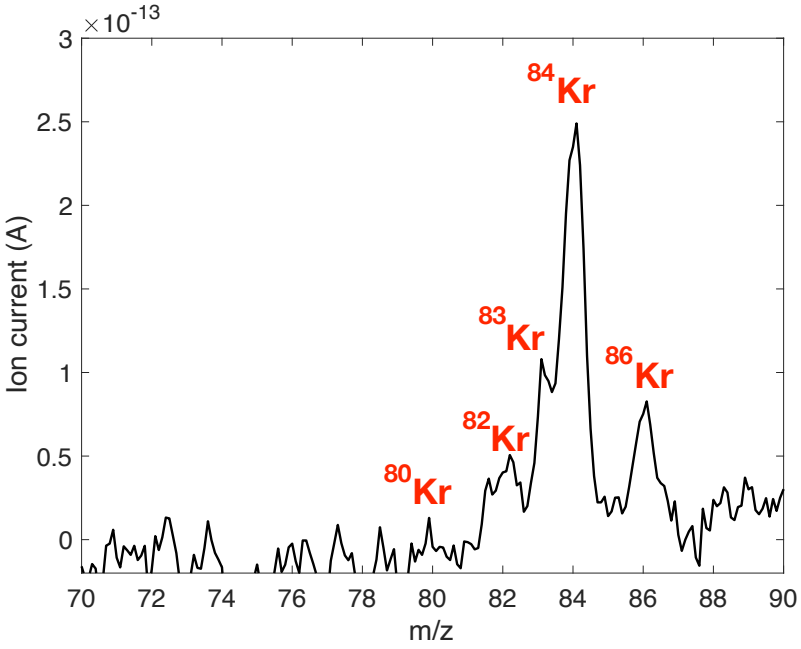

Fig. 5.25: Mass spectrum showing the isotopes of Kr, measured via the ICPMS prototype instrument. Kr was input as 1 SCCM of gas flow in a 14 W Ar plasma.

introduced into the plasma environment, and measured via the QMA (Fig. 5.25). A mass scan of the relevant mass range (m/z = 70-90) shows that the peaks are high enough resolution to distinguish individual isotopes, confirming the success of the peak tuning campaign. The Kr was input into the plasma via the sampler tube at a flow rate of 1 SCCM, with the Ar gas being input into the plasma tube at a flow rate of 10 SCCM, producing a plasma with an Ar/Kr ratio of $\sim$10. Estimates of the ionization efficiency of the Ar plasma indicate that elements with high first ionization potential such as Kr (13.99 eV) have a lower ionization efficiency than in He plasma. At 14 W of forward power, which was used for these experiments, the Ar plasma is predicted to ionize $\sim$50% of the Kr input in the system. Thus, switching to He plasma could potentially double the signal seen on each of the Kr peaks, as elements with the same first ionization potential can reach up to 99% ionization with He at similar power (Fig. 4.6). Regardless, the ratio of ^{40}Ar to ^{84}Kr ion current is similar to their respective ratio of the input gas flows due to their similar first ionization potential.

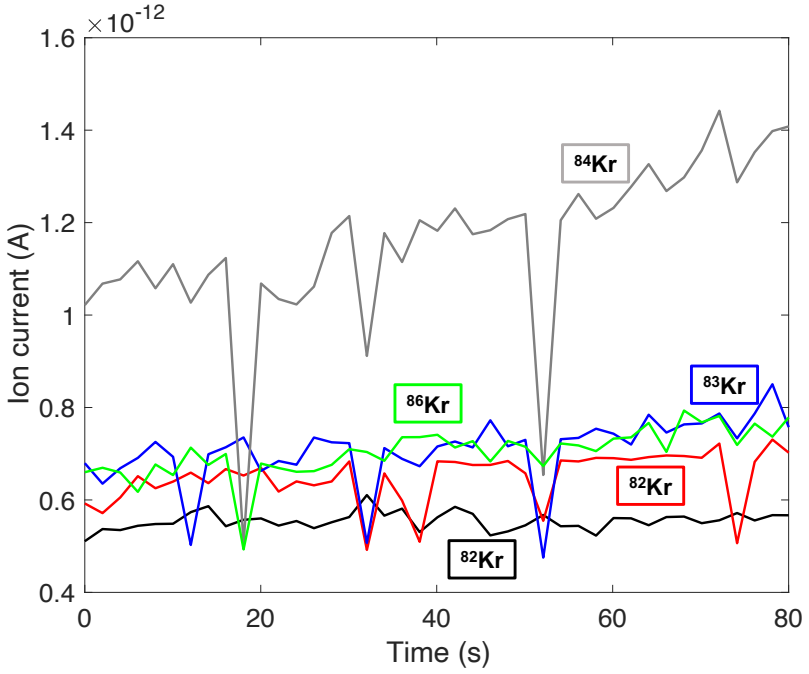

Fig. 5.26: Timescan of the measurement of Kr isotopes. Each mass station of Kr was monitored in peak-jumping mode on the faraday collector.

The QMA is capable of measuring a timescan, or peak-jumping from individual masses and measuring their abundances over time. For this analysis, each of the isotopes of Kr were selected and measured over 80 seconds in chromatogram mode (Fig. 5.26). This was done to monitor the stability of the ion signal over time, as well as to gather statistics on the average and standard deviation of the observed isotope abundances. Each mass signal was averaged over the 80 second collection time, and the average signal was used to calculate the isotope ratios. The uncertainty of the ratios was derived from the uncertainty of the measured signal.

Isotopic ratios may be altered by the instrument during analysis due to unequal transmission efficiency of isotope masses, known as mass bias. DC ion optics deliver ions to the mass spectrometer with different efficiencies, with low mass ions having lower transmission efficiency than high mass ions, which may fractionate isotope ratios. To account for instrument-induced mass bias, the mass fractionation correction between two similar iso-

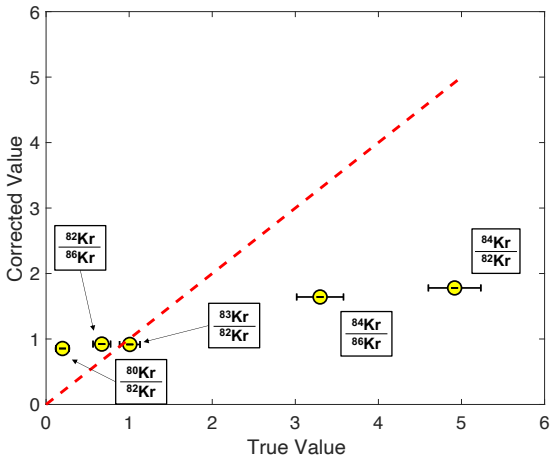

Fig. 5.27: Uncorrected Kr isotope ratio accuracy, as directly measured from timescan.

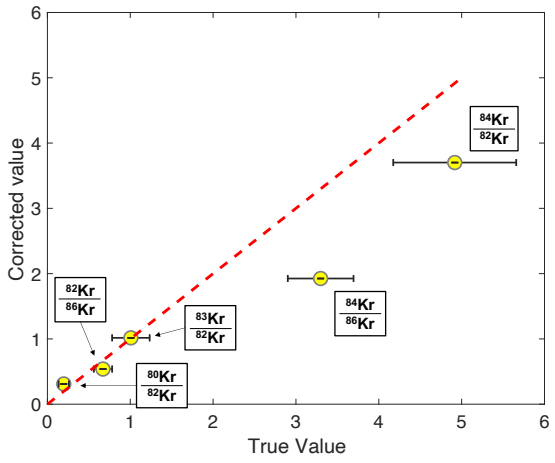

Fig. 5.28: Kr isotope accuracy after mass fractionation correction. The red line represents the 1:1 correlation between measured and true value.

tope masses (M_1 and M_2) is applied to the measured ratios using the Power Law, calculated as:

$$R_{true} = R_{meas} \times \alpha^{M_2 - M_1} \tag{5.9}$$

Where the α value is obtained from another similar isotope ratio with the same denominator, as:

$$\alpha = \left(\frac{true}{meas}\right)^{\frac{1}{M_3 - M_1}} \tag{5.10}$$

(Equations from [1]). The uncorrected values measured via the timescan (Fig. 5.27) show a linearity between the measured and the true value, although the linearity diverges from the 1:1 line between the observed and true ratios, indicating an inaccurate measurement relative to the true value. However, after the mass bias correction, the measured ratios trend closer to the 1:1 line, indicating that the corrected ratios are more accurate (Fig. 5.28). The accuracy of each ratio ranges from within 57% accuracy relative to the true ratio (e.g. ^{80}Kr/^{82}Kr), to within 0.9% relative to the true value (e.g.^{83}Kr/^{82}Kr). Further, the low accuracy of the ^{80}Kr/^{82}Kr ratio is likely due to ^{40}Ar dimers interfering with the m/z = 80 signal,

Ratio	True Ratio	Corrected Ratio	Accuracy	Precision (1 σ)
^{80}Kr/^{82}Kr	0.20	0.31	57%	20.1%
^{84}Kr/^{86}Kr	3.3	1.9	42%	20.6%
^{84}Kr/^{82}Kr	4.9	3.7	25%	20.1%
^{83}Kr/^{82}Kr	1.01	1.02	0.9%	22.3%
^{82}Kr/^{86}Kr	0.67	0.54	20%	20.6%

Table 5.1: Results of measured Kr isotope ratio accuracy relative to true value, and associated measurement precision.

in which future measurements would require background measurements for background subtraction. The precision of each of the corrected ratios is $\sim \pm 20\%$ (1σ). See table 5.1 for the full reporting of the precision and accuracy of the isotope ratios.

5.6 Instrument Performance and Scientific Goals

The instrument development effort detailed here was carried out to accomplish the scientific goals laid out in chapter 3, among other future landed in situ applications. The scientific questions that can be answered by any analytical instrument are limited by its performance metrics. Here, using the measured performance metrics of the prototype ICPMS, the feasibility of the science goals of a landed mission to the lunar farside is discussed.

As opposed to the faraday detector used in the experiments described in this chapter, a landed ICPMS instrument would instead use an electron multiplier as the ion detector. The electron multiplier produces secondary electrons that result in output signal in units of counts per second (cps), where the measured ion counts are proportional to the ion beam current. For example, as one ion has a charge of 10^{-19} C, the measured ion current of 10^{-12} A (e.g. Fig. 5.24) yields a total ion count of 10^7 cps. Here, the ion signal of a range of geologically relevant analytes measured by an electron multiplier is estimated.

The electron multiplier signal is estimated assuming an assumed Fe concentration of 1 wt.%, a 40 μm diameter laser spot size, and the measured ion transmission efficiency of this

instrument of $\sim 10^{-6}$. The signal is then used to calculate the sensitivity of the instrument, as well as the limit of detection (LOD) for each analyte. The LOD is calculated as:

$$LOD = \frac{3\sigma_{bgnd}}{S} \tag{5.11}$$

Where σ_{bgnd} is the measured uncertainty of the background, and S is the sensitivity (cps/ppm, from [116]). The limit of detection is calculated as ~5,500 ppm for Fe based on a measured background uncertainty of $\pm 10^{-14}$ A (7×10^4 cps). However, the measured background on our existing instrument is equivalent to the Johnson noise level, thus the actual LOD of the system is likely be lower than the value estimated here. Future iterations of a spaceflight QMA and detector will allow for a more accurate estimate of the instrument LOD. Efforts will be made to increase ion transmission efficiency, as well as to reduce background noise, to ensure that the detection limit is within the abundances of the analytes found in minerals on the lunar surface. Improvements on the system will allow this technique to achieve the science goals detailed in chapter 3.

Other factors regarding instrument performance and operations should be considered as well. For example, the mass loading capacity of the plasma may be another limiting factor in elemental analysis, as the thermodynamic calculations performed in chapter 4 indicate that a He plasma can atomize input sample generated by a maximum laser spot size of only 40 μm diameter pulsing at 10 Hz. Also, quantification uncertainties scale with abundance, with lower abundance elements potentially having higher uncertainties than higher abundance elements. These uncertainties are propagated when using elemental chemistry as a proxy for science goals, such as crystallization depth or mantle source composition [194], and future work should focus on documenting any abundance-dependent uncertainty.

5.7 Future Directions

The purpose of this effort was to produce a miniature ICPMS capable of measuring trace elements to low limits of detection in geologic materials. While the prototype instrument constructed here has demonstrated the capability to analyze input material, further work remains to expand the capabilities of the instrument.

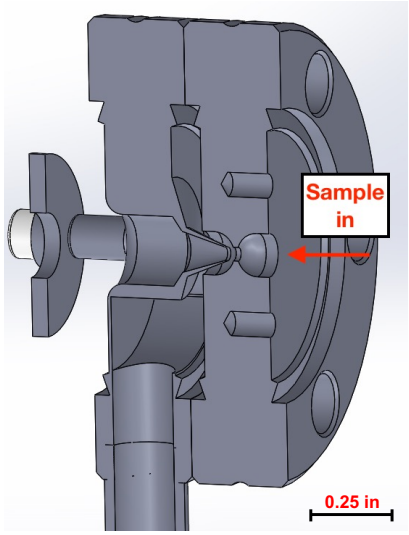

Fig. 5.29: CAD model depicting the newly designed skimmer cone interface, potentially allowing higher gas flow with limited ion loss. This system would allow the input of solid sample via laser ablation and aspirated liquid sample.

The sample input experiments relied on low gas flow (1 to 10 SCCM, mL/min), as higher gas flow would increase the pressure in the 90° deflector chamber, effectively reducing ion beam transmission. Here, I have designed and 3D printed a skimmer cone that can minimize ion loss through a differentially pumped chamber, allowing higher gas flow while maintaining low pressure at other chambers of the instrument (Fig. 5.29). This can allow the carrier gas to input ablated geologic material, as well as aspirated liquid sample, broadening the analytical capabilities of the prototype. The low power Ar plasma can also act as a "soft" ionization source, or one that ionizes the sample with minimal atomization. Thus future experiments will involve the input of organic material, such as amino acids or peptides for astrobiology purposes, which would require the ability to aspirate liquid into the torch environment.

A common method of inputting geologic material into a commercial ICPMS system is via laser ablation. Laser ablation (LA) ICPMS allows for trace element analysis of individual mineral phases, with spot analyses as small as 15-20 μm in diameter. LA sample introduction requires minimal sample processing, and maps to spaceflight technology due

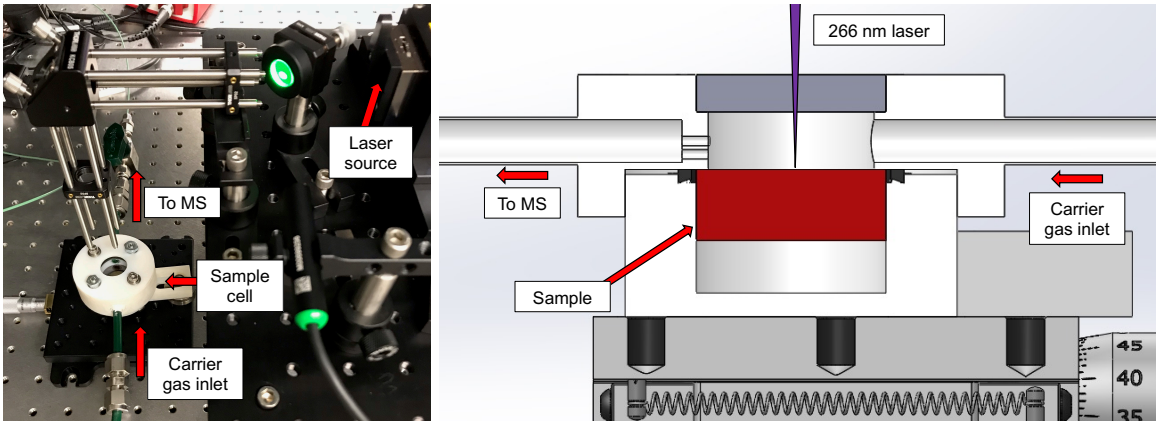

Fig. 5.30: **Left -** Photo of the assembled laser setup interfaced to the instrument setup. This includes a 200 μJ 266 laser and focusing optics. The laser ablation cell has been 3D printed, assembled, and tested for its vacuum compatibility. **Right -** Cross section of a CAD model of the sample ablation cell, showing the laser input and gas flow system.

to its ease of sampling and manipulation. Laser ablation sample introduction is a logical next step to the development of the prototype ICPMS.

Because the plasma system is maintained under vacuum, the sample introduction system must also be under vacuum prior to laser ablation. In lieu of interfacing the instrument to a commercial LA sample introduction system, a novel laser ablation sample cell has been designed, constructed, and installed onto the mass spectrometer (Fig. 5.30). This includes a 266 nm laser system, with optical elements to focus the beam to as small as 30 μm in diameter based on beam divergence calculations. The cell relies on He gas flow to carry the ablated material into the plasma torch; the carrier gas can double as the plasma gas itself. Thus, the capabilities demonstrated by this instrument will use the legacy standard of laser ablation to measure solid input sample.

Finally, as this effort was intended to construct a working prototype of a spaceflight ICPMS, future plans have been proposed to construct an engineering test unit (ETU) of the spaceflight hardware (Fig. 5.31). The ETU includes new innovations in spaceflight hardware, such as a multi-wavelength laser ablation system and a mobile sampling cell, and the

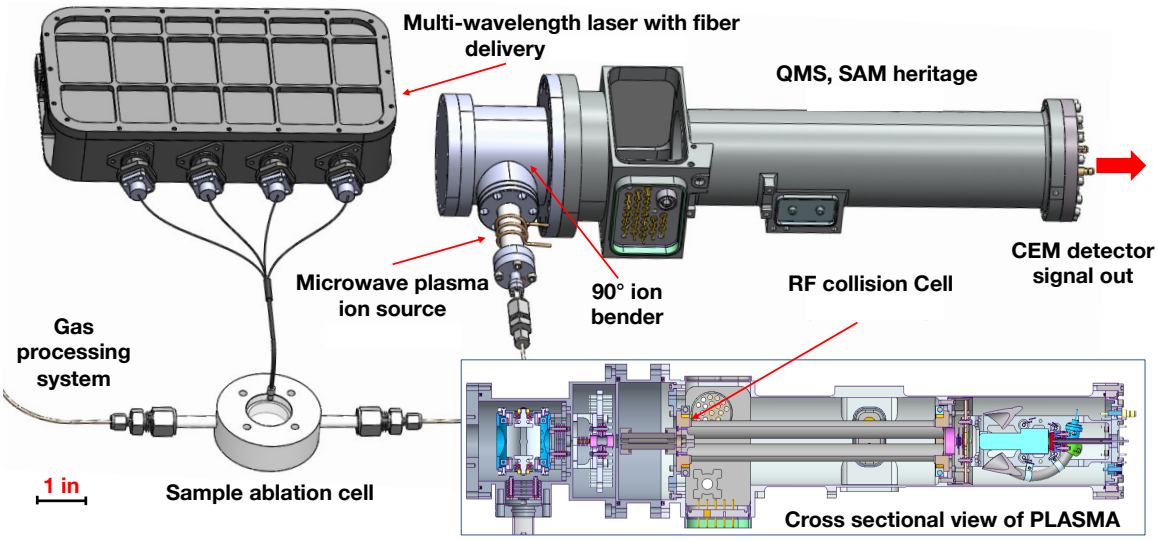

Fig. 5.31: CAD model depicting the full instrument concept developed as flight hardware. The novel mission concept has been proposed to the NASA DALI program, which would allow construction of flight hardware designed for lunar exploration.

ability to withstand hardware qualification such as thermal vacuum and vibration testing. This effort has been submitted to the NASA DALI program for funding consideration.

5.8 Conclusion

I have constructed a prototype mass spectrometer using a low power plasma as the ion source, demonstrating the end-to-end proof of concept of a miniature ICPMS. The instrument was tuned for maximum ion transmission, and has demonstrated its performance measuring input sample. Measurements of ion transmission efficiency show progressive loss of ions throughout the ion optic setup, with a final transmission efficiency calculated at $\sim 10^{-6}$ - 10^{-7}, as compared to commercial systems which record efficiencies of $\sim 10^{-3}$ - 10^{-4}. Kr was introduced into the ion source and its isotope ratios were measured to a precision of $\pm 20\%$ (1σ) and accuracy ranging from within 0.9% to within 57% due to interference from an Ar dimer. While future work is needed to allow input geologic

material, aspirated liquid sample, and organic material into the mass analyzer, this shows that the prototype instrument is capable of sample analysis using a reduced power, low pressure plasma source.

Chapter 6: Conclusions

6.1 Key Conclusions:

Using the dual-pronged approach of geochemistry and instrumentation, this dissertation has identified a scientific and technological foundation for a planetary mission that includes in situ analysis which focuses on targeting trace element abundances in lunar materials. In chapters 2 and 3, I have identified a series of geochemical proxies that may be used to understand better the history of the Earth and Moon, and applied some of those proxies to a geological system relevant to the Earth in chapter 2. I also identified a series of landing sites on the lunar farside with lithologies that would best deliver on the stated science goals in chapter 3. Combined, these studies document the relevance of targeted trace elements to understanding better planetary history.

Additionally, a miniature ICPMS was developed and constructed as a prototype for a spaceflight instrument proof of concept. The miniature plasma system was integrated to a quadrupole analyzer and a faraday cup detector demonstrating an end-to-end system for analyzing samples. The capability of the plasma to operate as an ion source was first investigated in chapter 4. Chapter 5 describes the buildup of the instrument and documents its performance. Overall, the major conclusions of this dissertation are as follows:

1. **K/U value of the Bulk Silicate Earth:** Using the log-log plot method of processing trace element abundance data, we estimate the relative partitioning of K and U between silicate melt and residue and find that K has a higher solid/liquid partition

coefficient than U by a factor of 3 to 7×. This shows that K fractionates during mantle melting, causing systematic variation in the K/U value of incompatible element enriched or depleted silicate reservoirs.

We calculated a lower bound of K/U, between 14,000 and 15,500, for mantle source of MORB, although the ratio may be higher in depleted sources. Combining this limiting value with the K/U ratio of the continental crust and OIB sources, we estimated the has a BSE K/U >12,100, and a BSE K abundance of >260 μg/g, which generates ∼3.5 TW of heat in the Earth.

2. **Trace element investigations of the lunar farside:** In order to understand better the structure and composition of the lunar farside mantle, a series of geochemical proxies should be targeted in specific lithologies. Specifically, a mission could measure Al and Cr contents in olivine or Al and Ti contents in pyroxene to determine the temperatures and pressures of basalt formation, Fe, Zn, Mn, or Ni contents for mantle source mineralogy, K, Th, and U contents in exposed upper mantle material for radiogenic heat investigations, and Rb-Sr isotopes for major event chronology. Applying these proxies to farside exposed mantle materials and later emplaced mare basalts could provide critical insights into the farside formational history.

   The locations best suited for these analyses are Apollo, Leibnitz, Moscoviense, and Von Karman craters on the lunar farside. All of these localities contain exposed mantle material contacting with multiple mare basalt units, as well as flat terrain for minimal mission hazards.

3. **Characterization of low power plasma:** Low power plasma generated from He or Ar gas flow is a viable ion source for an ICPMS at low pressure (1 torr; 10^3 Pa) and low gas flow (10 cm^3/min). The plasma electron density decreases and the electron temperature increases with decreasing pressure, driving up ionization efficiency in

low pressure systems. Langmuir probe analyses of He and Ar plasmas show that He produces a higher electron temperature than Ar, indicating that He is a more efficient ionizer. Empirically measured electron temperature and electron density are used to estimate the ionization efficiency of a range of elemental ionization potential, and shows that 99% ionization efficiency can be achieved with 23 W of Ar and only 5 W of He at low pressure.

Thermodynamic models show that low power He plasma can also atomize sub-μm solid materials, opening the door to laser ablation sample introduction. At the measured plasma temperature, we estimate that the He plasma can atomize 2×10^{-9} g/s of silicate material, comparable to typical sample input generated by laser ablation.

4. **Miniature ICPMS prototype:** I constructed a miniature ICPMS prototype as a proof of concept technology demonstration. I have integrated the plasma ion source to a quadrupole mass analyzer and faraday cup detector. The prototype instrument includes a He or Ar plasma operating at $<$25 W of forward power, with a series of DC ion optics tuned to optimize ion delivery to the mass analyzer. The estimated ion transmission efficiency of Kr is $\sim10^{-7}$, which is below the operation of commercial ICPMS systems ($\sim10^{-3}$). Measurements of a Kr gas sample show the ability to resolve individual isotopes, demonstrating that the instrument can analyze an input sample. The isotope ratios of the measured Kr sample are estimated to have precision of $\sim \pm20\%$ (1σ), and range in accuracy from within 57% to 1% of their true value. This represents a benchtop validation of the instrument concept, bringing the prototype to a NASA-defined maturity of technical readiness level (TRL) 4, which is a laboratory demonstration of the proposed technology.

6.2 Future Directions

The efforts described in this dissertation represents a foundation for the complete ICPMS instrument concept and accompanying mission objectives. While major progress has been made on the development of the prototype and identification of science targets, more updates to the prototype instrument are necessary to improve its performance and analyze other samples. Further, a campaign to analyze the proxies identified above can deliver more insights into how a mission operation would proceed, and what level of detection limits and uncertainty are necessary to answer the stated science questions. Looking forward, the science will drive the needed performance.

A new skimmer cone interface region will be added to the front end of the plasma inlet, which would allow for higher gas flow from laser ablation or higher torch pressure from input liquid sample. The skimmer cone system would allow for higher pressure sample introduction (e.g. aspirated liquid, laser ablation sampling), allowing improved estimates of limit of detection and demonstrating the quantification of trace element abundances. From here, the geochemical proxies identified in chapter 3 can be measured on the prototype instrument, documenting the precision, accuracy, and instrument performance. Using the instrument developed here, these investigation could include measuring Al, Ti, and Cr abundances in olivine and pyroxene for thermobarometry, Rb-Sr for geochronology, or first row transition elements for mantle mineralogy in lunar and martian meteorites.

Appendix A: K/U of the MORB source and silicate Earth

The data accompanying this chapter was downloaded from the Earthchem database, and filtered using the criteria identified in the manuscript. In order to investigate the difference between K/U from K_2O and K measured as a trace element, K_2O measurements were converted from oxide wt.% to K wt.% by multiplying K_2O data by the K molar proportion in K_2O (0.8301), then into concentration in 10^{-6} kg/kg by multiplying by 10^4.

The 1st and 3rd interquartile range (IQR) of the K and K/U data spread were recorded, and the outliers were calculated as $3\times$ the difference between the 1st and 3rd IQR. K and K/U data were filtered to be within the range of the 3rd IQR high and low outliers. A similar filter scheme was applied to the K, U, and K/U data converted to log form, and also filtered out by 3rd IQR high and low outliers.

The figures compiled below demonstrate the fractionation of the K/U ratio as a function of incompatible element enrichment or depletion and magma evolution, further highlighting the conclusions drawn by this study.

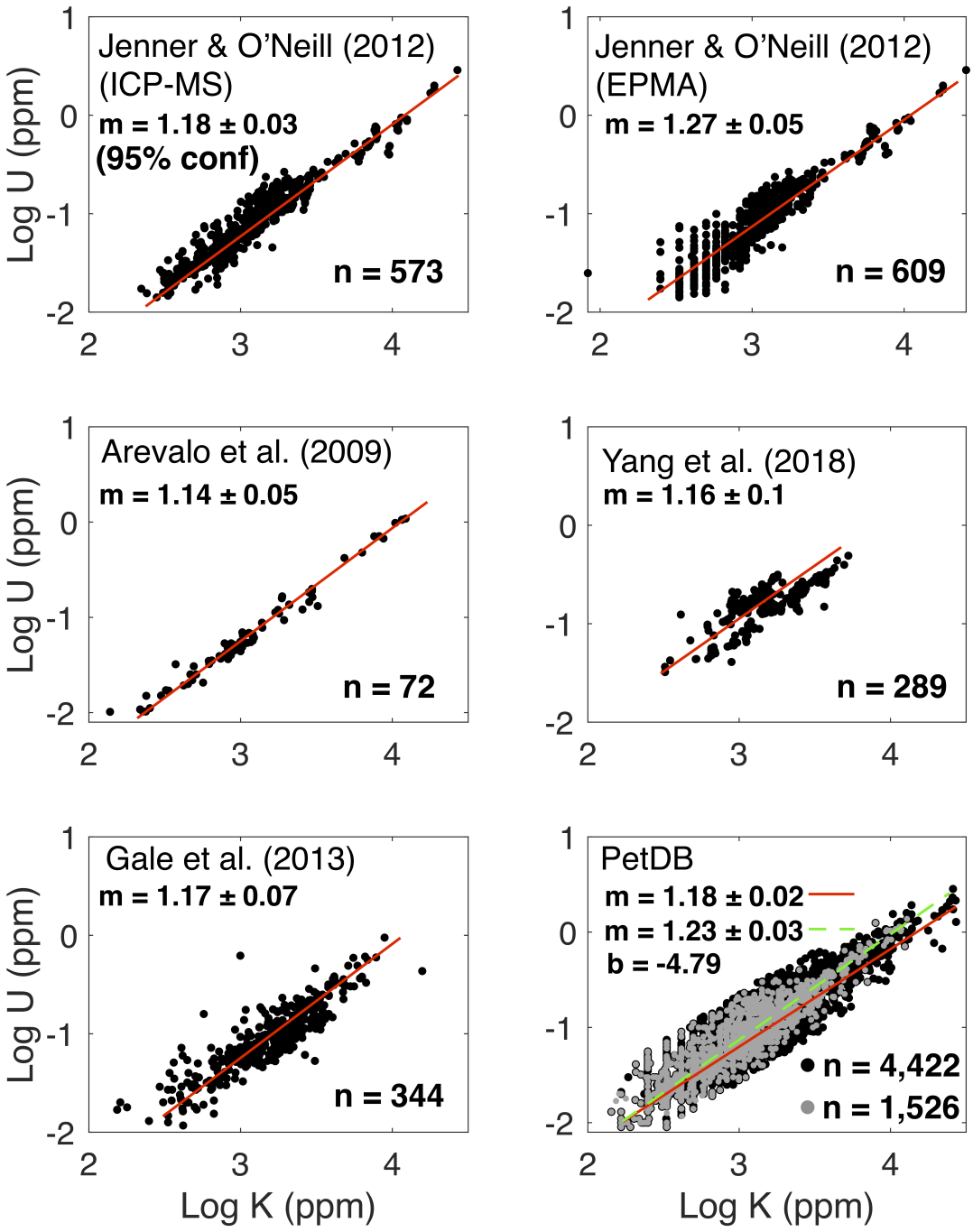

Fig. A.1: Results of log-log regression analyses of MORB K and U data taken from multiple sources. Data from Jenner & O'Neill (2012) and the PetDB database consist of K measured as both a trace element (via LA-ICP-MS) and an oxide (via EPMA), so two regressions are produced per data source. All data sources indicate that U is measurably more incompatible than K, and the slope of the bivariate regression indicates the difference in partition coefficients during MORB genesis. Plots of PetDB data shows all MORB samples (black circles) and MORB samples with $>$ 8 wt.% MgO (grey circles). Source K estimates rely on regression statistics from PetDB samples with $>$ 8 wt.% MgO (green dashed line).

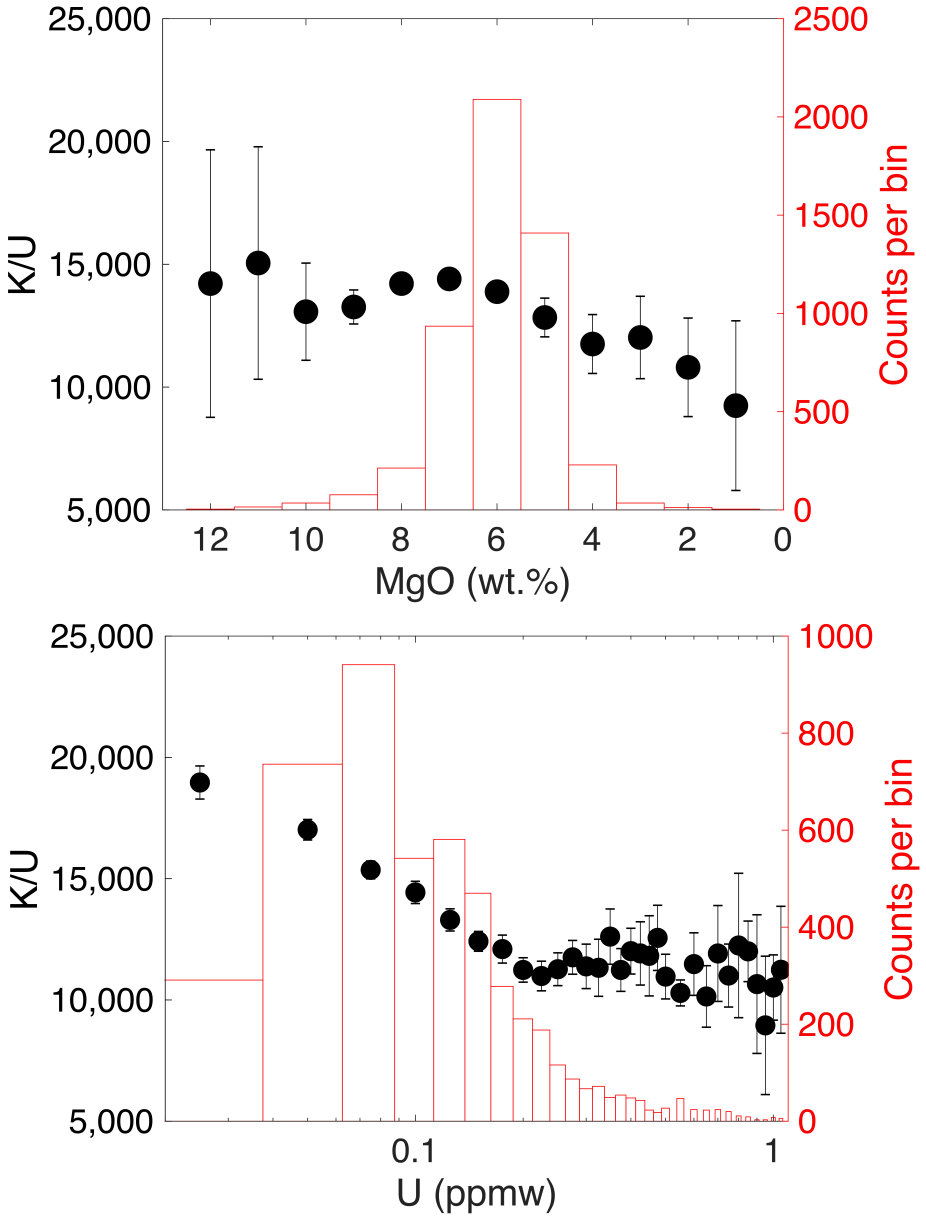

Fig. A.2: K/U fractionation mapped in global MORB as a function of (A) fractional crystallization (tracked by MgO), and (B) absolute abundances of incompatible element enrichments (e.g., U). Data from full PetDB compilation.

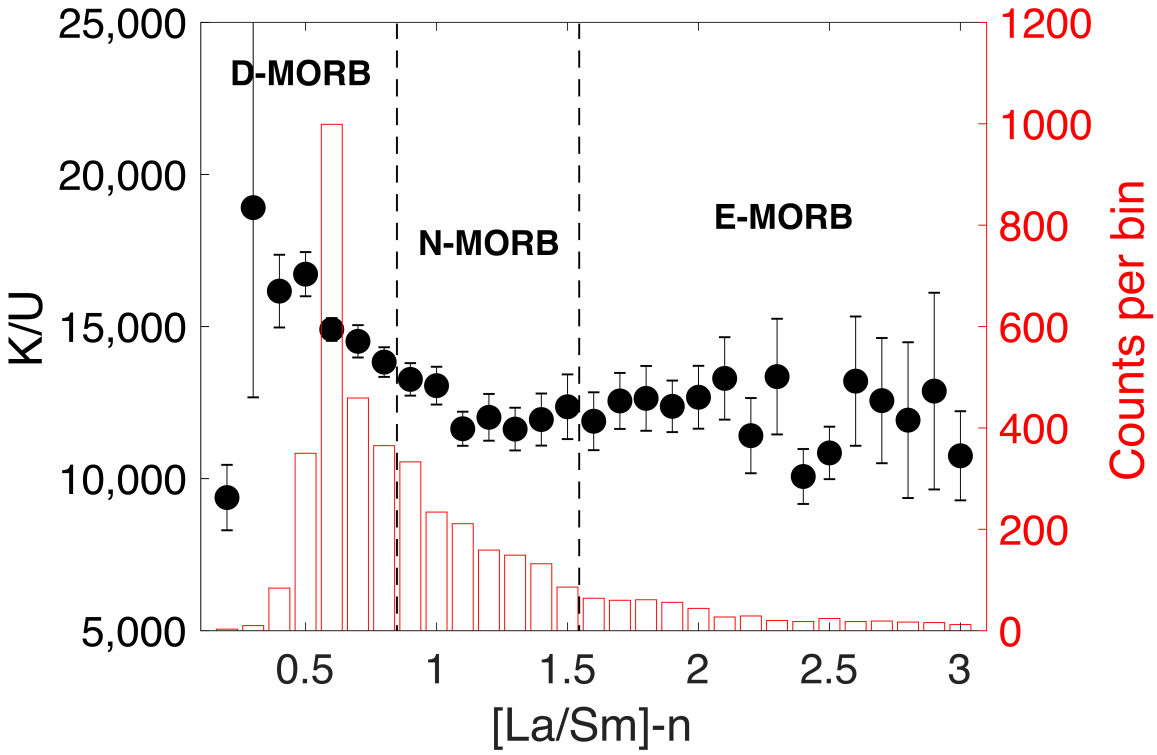

Fig. A.3: K/U fractionation mapped in global MORB as a function of source enrichment/depletion in incompatible elements. D-, N-, and E-MORB are defined as [La/Sm]n >0.8, 0.8-1.5, and $\leq$ 1.5, respectively. Data bin sizes are: MgO = 1 wt.%, U = 0.025 ppb, and [La/Sm]n = 0.1. Data from full PetDB compilation.

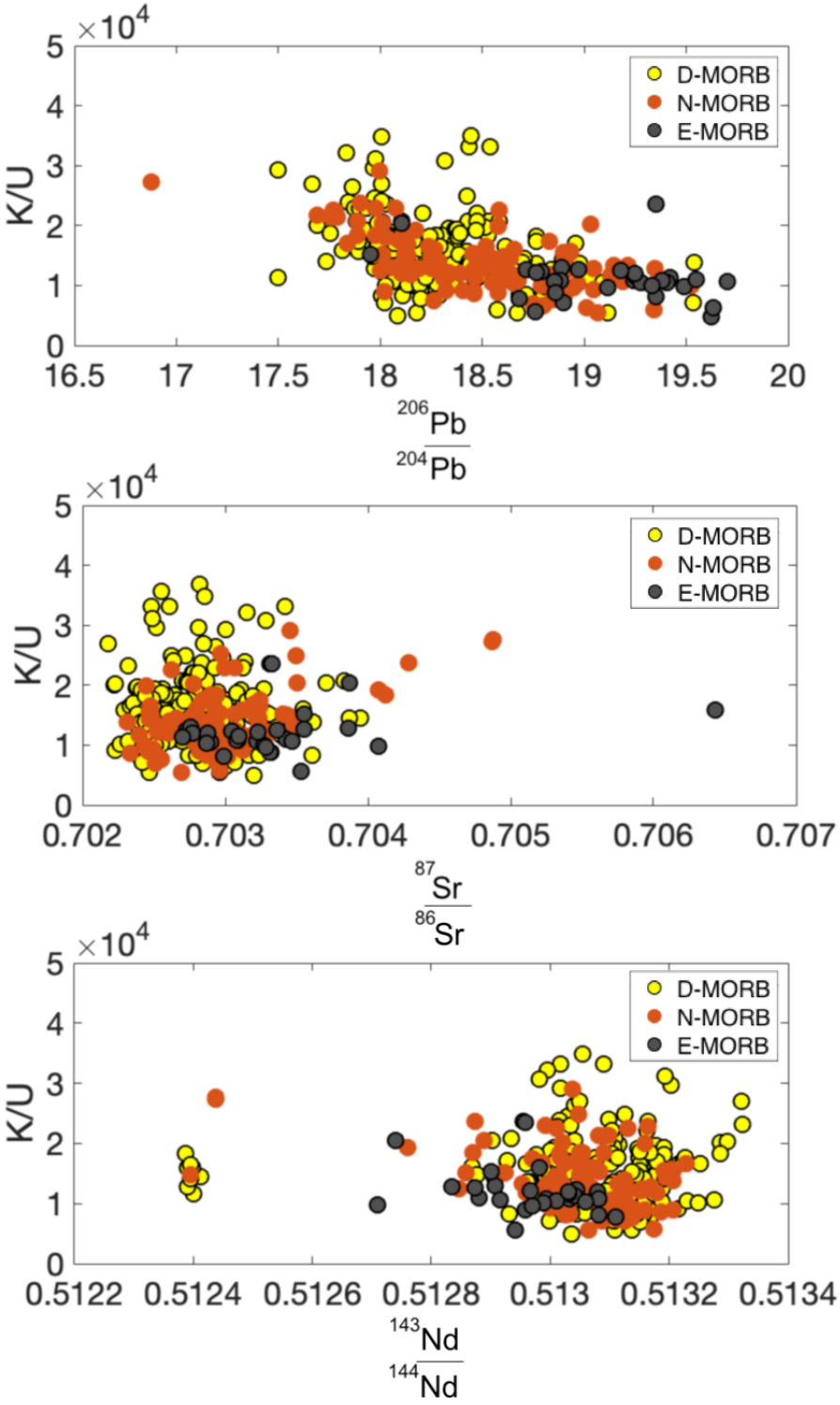

Fig. A.4: K/U fractionation in D-, N- and E-MORB (defined in Figure A.3 legend) subpopulations map to signatures in Pb, Sr, and Nd isotope systems. Only samples with $>$ 8 wt.% MgO are shown in order to isolate fractional crystallization effects. All three sample groups are statistically distinct in K/U space based on parametric t-tests. Data from PetDB

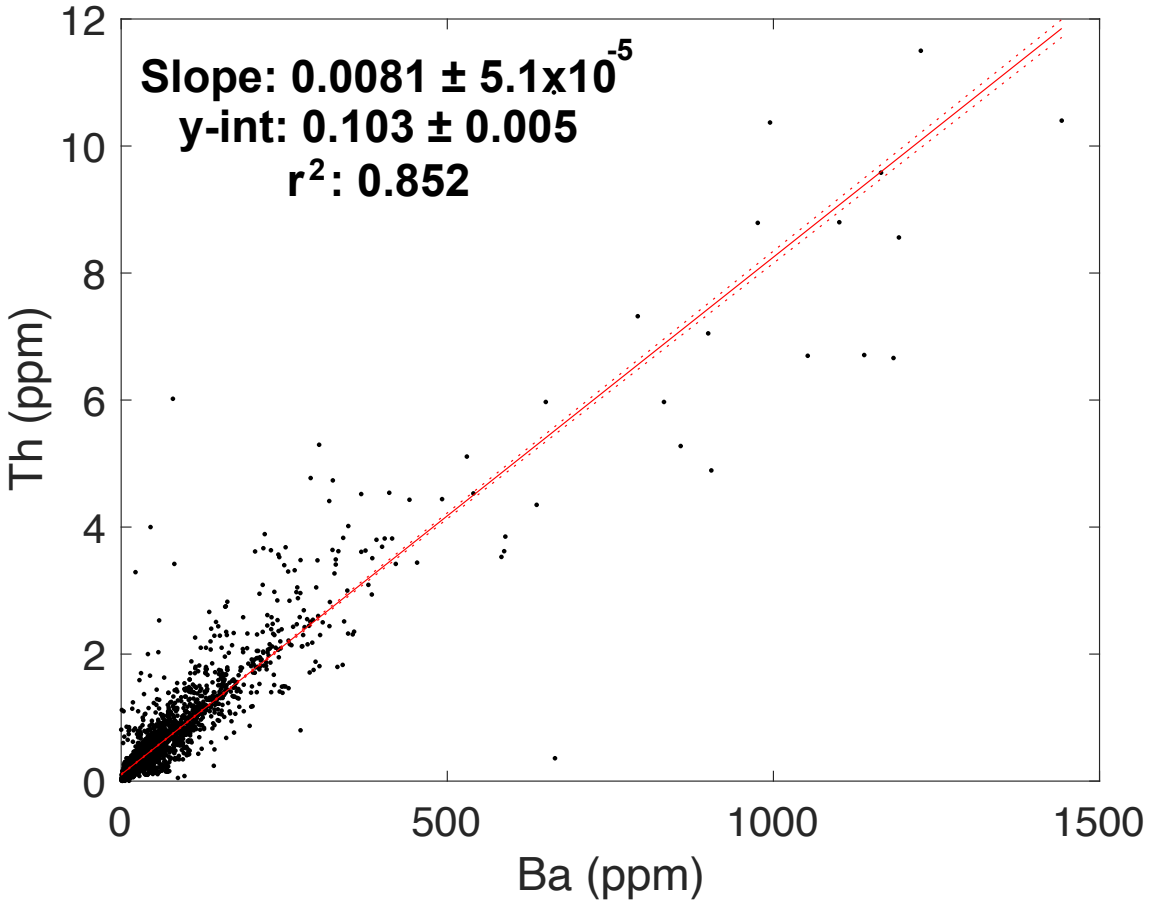

Fig. A.5: Plot of Ba vs Th in MORB samples. A cohesive linear trend between Ba and Th concentration shows little seawater alteration of the samples due to the higher fluid mobility of Ba relative to Th. Solid red line represents linear regression of the data, and dotted lines represent 95% confidence interval on regression.

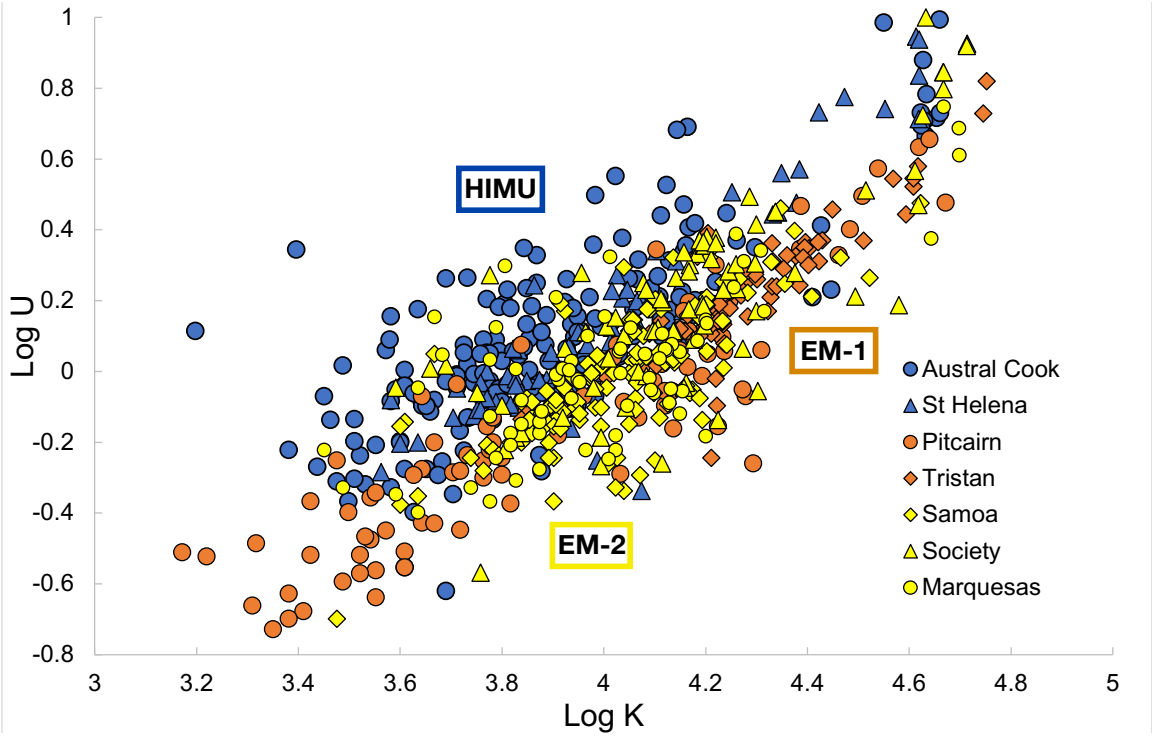

Fig. A.6: Log-Log plot of the K and U abundances of various OIB end-member localities. Different mantle components are defined based on isotope ratios representing enrichment or depletion of incompatible elements. Distinct reservoirs are defined as EM-1 (Enriched mantle 1, recycling of crustal sediments), EM-2 (Enriched mantle 2, recycling of continental crust), and HIMU (high μ=^{238}U/^{204}Pb) [86, 216]. HIMU basalts have a higher U abundance, as shown in both absolute abundance and radiogenic Pb isotopes, leading to a lower K/U ratio than OIBs sourced from other mantle reservoirs.

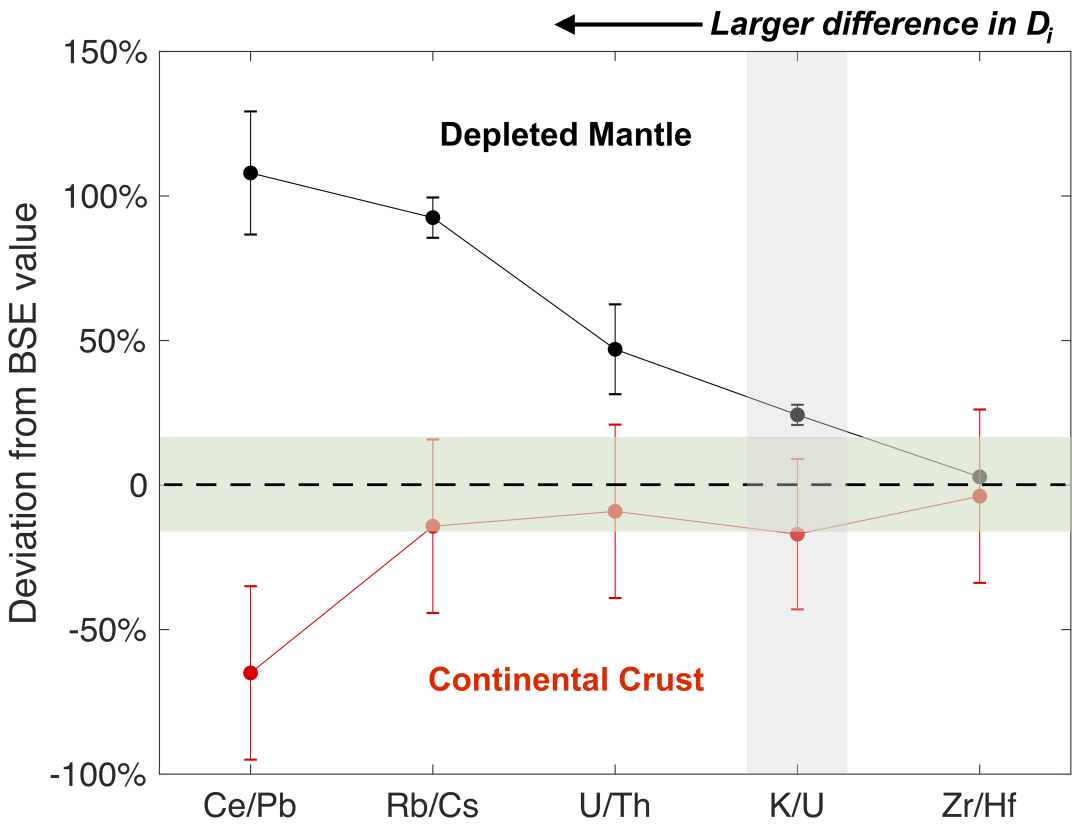

Fig. A.7: Fractionation of trace element ratios due to continental crust extraction. Depleted mantle values calculated using MORB data >8 wt.% to better estimate primary melt compositions, and assuming 10% partial melting relying on partition coefficients ($D^i_{sol/liq}$) from Salters & Stracke (2004). Continental crust composition from [169], and primitive BSE values from [130]. Green bar represents ± 20% deviation from the BSE value.

Appendix B: Application of Trace Elements to Lunar Landed Science

Introduction

Trace, minor, and major elements occupy specific sites in the crystal structure of a mineral, with partition coefficients (K_D) measuring the partitioning of a specific element between two phases ($K_D = \frac{C_1}{C_2}$) at equilibrium. The equilibrium partitioning of an element between two phases is often sensitive to pressure and temperature, so this sensitivity can be exploited to understand temperature and pressure of formation. These geothermobarometers require experimental calibration, where the partitioning of elements between phases is measured as a function of known temperature and pressures, often produced by piston cylinder presses or diamond anvil cells. The composition or elemental partitioning is then plotted as a linear regression relative to experimentally controlled temperature or pressure, allowing mineral-specific composition measurements to be applied to the experimental results. Here, we use two separately calibrated geothermometers in order to measure the temperature and pressure of crystallization of a series of ocean island basalt (OIB) samples.

Ocean island basalts are the result of volcanism occurring separate from plate tectonics, typically emerging as intraplate volcanics. These volcanic centers are interpreted to be hot spot plumes of high temperature ambient mantle buoyantly rising to the crust [81, 135], with seismic evidence supporting this [134]. Here we apply a series of geothermobarometers to various OIB localities to discern the crystallization pressures and temperatures of

these intraplate volcanic centers. This also serves as a demonstration of these thermobarometers as they would be used by an in-situ planetary mission, as these measurements are feasible with the prototype ICP-MS currently under development.

Sources of Data

Data was collected from the GeoRoc database for Azores, Pitcairn, and Galapagos, from the PetDB database for Hawaii, and from [171] for Reunion. When searching the databases, the filter criteria was set to deliver separate mineral compositions of olivine, clinopyroxene, and spinel only. The data sets were processed by converting all FeO + Fe_2O_3 into FeO_T and filtering the mineral oxide sums as $100 \pm 3\%$. The OIB localities were selected to reflect a range of estimated mantle potential temperatures from [163].

Barometry

The full context of basalt crystallization requires constraints on pressure to help constrain temperature, so a geobarometer is first applied to the samples. We estimate pressure using the pressure-sensitive partitioning of Al and Ti in specific sites in clinopyroxene. Tschermak pyroxene are pyroxene crystals with 3+ cations substituting for 2+ cations in the M1 site of the mineral (generalized pyx formula - $M1M2T_2O_6$). Al is more likely to be accepted into the M1 site due to its smaller ionic radius relative to Ti (Al^{3+} = 0.675 Å, Ti^{3+} = 0.81 Å). Lattice strain theory predicts that this site becomes smaller at higher pressure, thus allowing less Ti into the site and lowering the Ti/Al ratio with higher pressure.

In order to calculate site specific abundances, mineral oxide must be converted into atoms per formula unit (apfu). The conversion is calculated as:

1. Divide the oxide composition by the molecular weight of the oxide to get molecular proportion (e.g. CPX SiO_2 = 55 wt.%, SiO_2 = 60 g/mol, =0.917).

2. Multiply that proportion by # of oxygens in the oxide to calculate proportion of anions measured (2 oxygen per SiO_2, 0.917*2 = 1.83).

3. Calculate mineral-specific normalization factor. If clinopyroxene has 6 oxygens per formula unit, divide 6 by the sum of all anion proportions from each oxide (if sum of all anion proportions = 2.3, 6/2.3 = 2.6).

4. Multiply the proportion of anions by the normalization factor (1.83*2.6 = 4.76 anions per formula unit).

5. Divide # anions by anions per cation (for SiO_2 = 2 anions per cation, 4.76/2 = 2.38 cations Si per formula unit).

Once all compositions have been converted to apfu with this formula, plot Al vs Ti (apfu) along with experimentally determined regressions deliminating various crystallization pressures. This barometer has been calibrated by [141] and [60], and previously applied to Martian basalts [36, 143]. While magma ascent tends to record multiple pressures of formation in different geobarometers, this barometer characterizes the final, lowest pressure during ponding and crystallization.

Al-Cr thermometry, using olivine only

A series of thermometers have been calculated by [47], based on the observation that the partition coefficients of Al and Cr in olivine are highly temperature and pressure sensitive. This allows simple thermometers to be applied solely to olivine chemistry if crystallization pressure is constrained. [47] constrained three Al-Cr-olivine thermometers, as

$$T_{Al-Cr-ol}(^{\circ}C) = \frac{9423 + 51.4P + 1960Cr\#^{ol}}{13.41 - ln[Al]^{ol}} - 273 \tag{B.1}$$

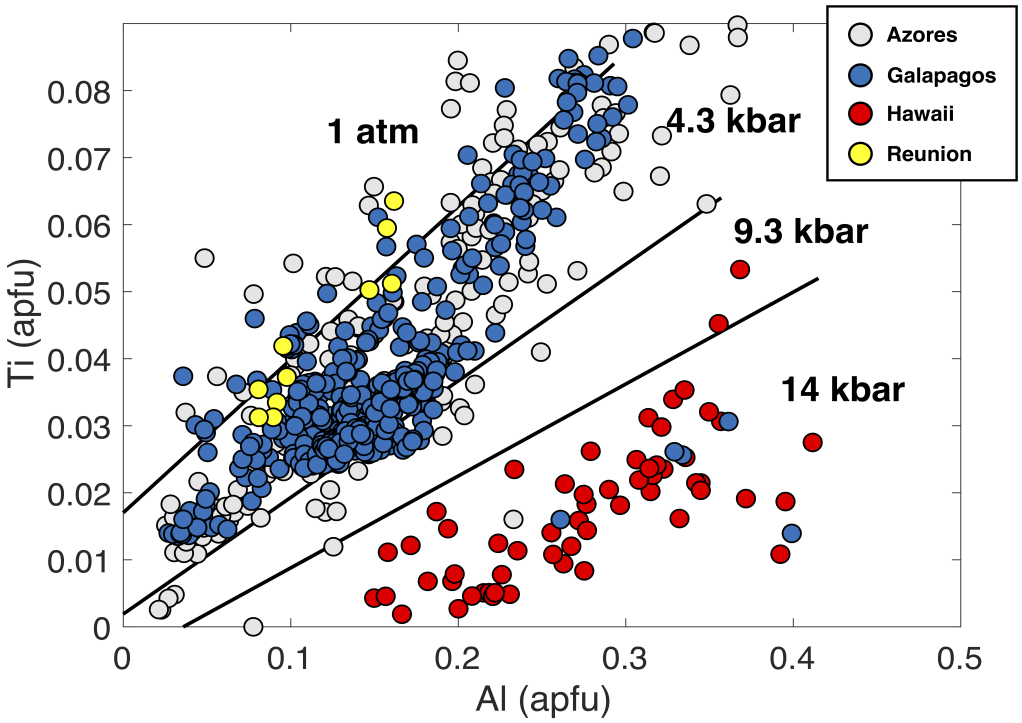

Fig. B.1: Pressure estimates using Al-Ti partitioning in CPX. Al and Ti contents calculated as atoms per formula unit (apfu) using method described above. Pressure calibration lines from [60, 141]

$$T_{Cr-ol}(^{\circ}C) = \frac{13,444 + 48.5P - 4678Cr\#^{ol}}{14.53 - ln[Cr]^{ol}} - 273 \tag{B.2}$$

$$T_{Al-ol}(^{\circ}C) = \frac{11,959 + 55.6P}{14.53 - ln[Al]^{ol}} - 273 \tag{B.3}$$

Where Cr # is

$$\frac{Cr}{Cr + Al}(molar)$$

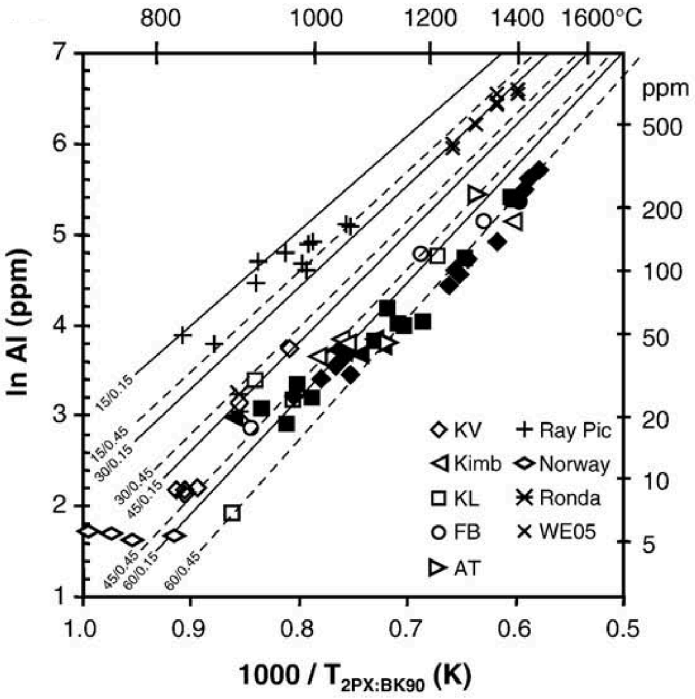

Fig. B.2: Temperature Al in olivine calibration from [47]. Dashed lines represent Cr# values of 0.15 and 0.45, respectively

Calculating temperature from these thermometers reveals 2σ uncertainties of 100-215

$^{\circ}C$ for all OIB localities, except Pitcairn with uncertainty of 25-45 $^{\circ}C$. The typical uncertainty for these thermometers is $\pm$ 22 $^{\circ}C$. This geothermometry method records equilibrium partitioning of elements between olivine and surrounding crystals, thus this records the highest temperature of equilibrium after the sample has completely crystallized.

Al-Cr thermometry, olivine and spinel partitioning

The temperature-sensitive nature of Al abundance in olivine has been exploited as other thermometers as well. [39] and [199] used a piston-cylinder apparatus to calibrate the temperature-dependent equilibrium partitioning of Al_2O_3 between olivine and Cr-spinel. The equilibrium temperature is estimated as:

$$T(^{\circ}C) = \frac{10,000}{0.575 + 0.884\text{Cr\#}^{\text{sp}} - 0.897\ln[\text{K}_\text{d}]} - 273 \tag{B.4}$$

Where

$$K_d = \frac{[\text{Al}_2\text{O}_3]^{\text{ol}}}{[\text{Al}_2\text{O}_3]^{\text{sp}}}$$

This thermometer represents the highest temperature that the olivine is at equilibrium with the surrounding melt, as opposed to the previous thermometers which record equilibrium with surrounding crystals.

No mineral separates that were downloaded from PetDB or GeoRoc had compositions for both olivine and spinel in the same sample, so this thermometer could not be directly applied to the downloaded data set. Mineral compositions from the supplementary materials of [39] do show individual ol-sp partitioning data, so the three Al-Cr thermometers established previously by [47] were applied to these samples.

Plots comparing equilibrium temperature (olivine only) with crystallization temperature (olivine-spinel) show a systematic difference of about 100-150 $^{\circ}C$ between these two

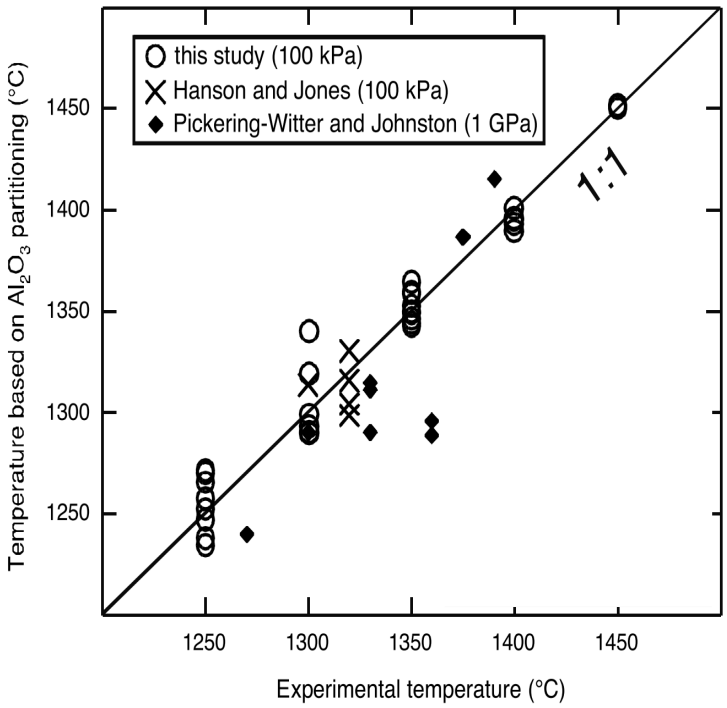

Fig. B.3: Experimental calibration curve from [199]. Temperature calculated using Al partitioning between olivine and spinel, and measured experimental temperatures at various pressures.

methods. Cr in olivine thermometry shows the largest discrepancy between equilibrium and crystallization temperatures, and has temperature estimates systematically lower than all other geothermometers. Because of the lack of OIB samples with both olivine and spinel measurements, the crystallization temperature of each OIB locality was calculated with the regression equation relating the two thermometers.

Although the two geothermometers have systematic differences in their calculated crystallization temperatures by about 100 °C, uncertainties of both thermometers applied to this data set have 2σ uncertainties up to 287 °C, therefore these two methods produce temperatures that are within uncertainty of each other. In this case, the two thermometry methods

	14 kbar	4.3 kbar	3 kbar
Al+Cr	y = 1.26(T(°C)) - 219	y = 1.31(T(°C)) - 199	y = 1.32(T(°C)) - 196
Cr only	y = 1.46(T(°C)) - 296	y = 1.53(T(°C)) - 290	y = 1.53(T(°C)) - 291
Al only	y = 1.43(T(°C)) - 400	y = 1.50(T(°C)) - 382	y = 1.50(T(°C)) - 383

Table B.1: Regression statistics for temperature comparisons at various pressures

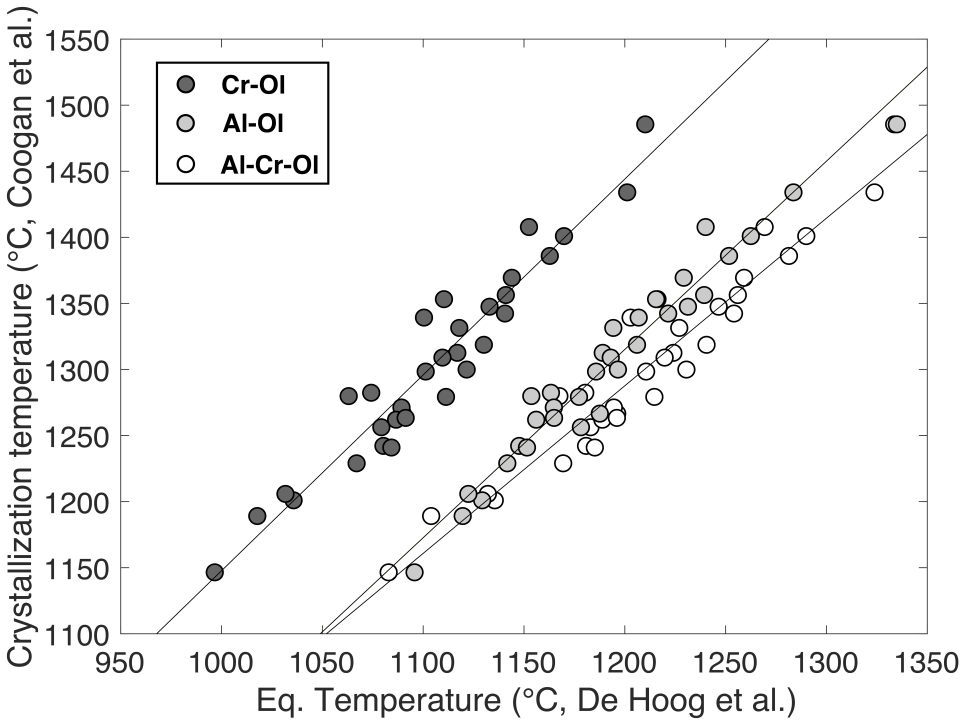

Fig. B.4: Comparison of temperature estimates using regression methods of [47] and [39]. Regressions show that temperature estimates using Al-Cr in olivine only result in a systematically lower temperature estimate of 100-150 °C) than partitioning between olivine and spinel. Calculations performed on samples from supplimentary tables of [39] at 14 kbar.

can act as redundant checks on each other in cases where spinel grains or pressure estimates are unavailable.

Other temperature proxies

Other temperature proxies based on olivine chemistry can be used as a check on these results. For instance, Ni abundance and molar Mg# both correlate with crystallization and mantle potential temperature [167, 195] and have also been calibrated as a geothermometer [80]. Plots of crystallization temperature correlate with both olivine Ni abundance and Mg#, showing that olivine Al-Cr speciation occurs in conjunction with other temperature sensitive tracers.

Estimates of mantle potential temperature from oceanic basalts show that OIBs record hot spot magmatism in excess of the mantle potential temperatures recorded by MORBs by 100-300 °C [163]. Similar hot spot magmatism is evidenced on Mars, where shergottite meteorites form from mantle potential temperatures in excess of 200 °C of the potential temperatures recorded by flood basalts [59]. If this olivine thermometry is applied to a single landing site that contains multiple styles or ages of magmatism (e.g. [105]), these measurements can provide insight into the cooling or crystallization history of Martian crust or mantle derived magmatism.

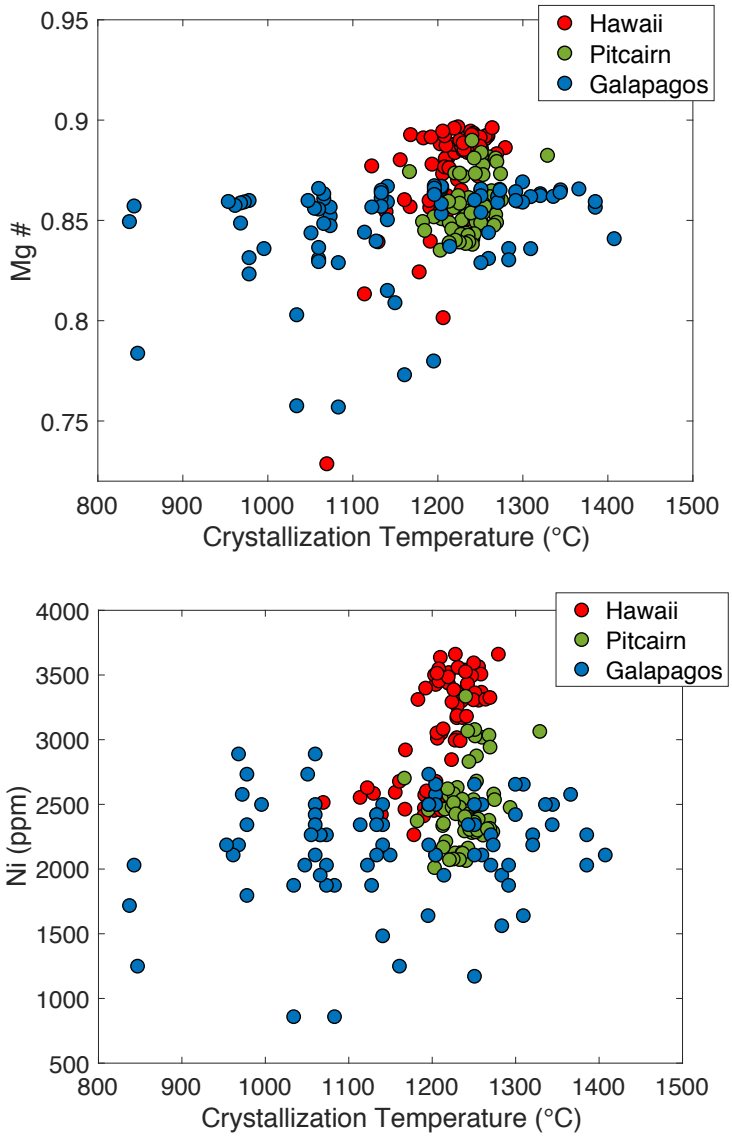

Fig. B.5: Comparison of Mg# and Ni content relative to calculated olivine temperature. Both these values act as temperature proxies as well.

Appendix C: A Prospective Microwave Plasma Source for In Situ Spaceflight Applications

C.1 Plasma Characterization by Optical Emission Spectroscopy

In addition to plasma analysis using a Langmuir probe, electron density and temperature can also be measured in a plasma spectroscopically. Further work is done on a series of analytes injected into a commercial plasma, and their relevant physical parameters (Te and Ne) are measured by inductively coupled plasma optical emission spectroscopy (ICPOES).

Three samples of single element standard solutions with varying first ionization potentials are used to compare the predicted Saha ionization efficiency with a directly measured ionization efficiency. 10 ppm (μg/ml) solutions of La (5.5 eV, first ionization potential), Mg (7.6 eV), and Zn (9.4 eV) are dissolved in HNO_3 and individually injected into the plasma via an autosampler. A Shimadzu ICPOES 9800 was used to generate the plasma and measure the emission spectra of both

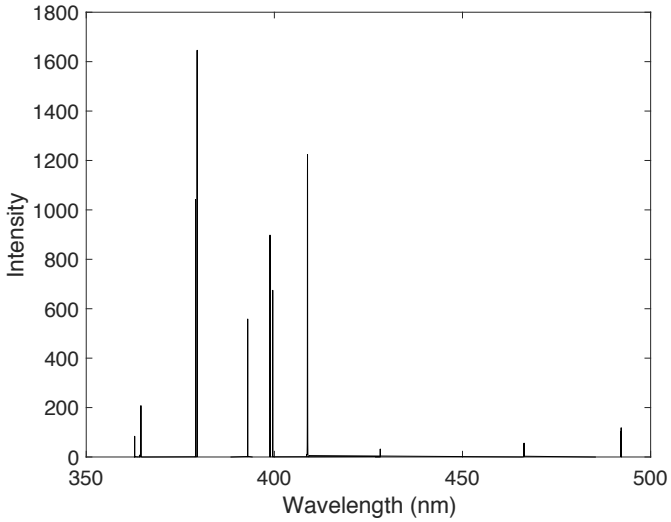

Fig. C.1: Example composite spectrum of La ion and neutral emission, measured by a Shimadzu 9800 plasma optical emission spectrometer

ionized and neutral species. All constants and statistical parameters associated with each emission are taken from the NIST atomic spectroscopy database

C.2 Electron density

The electron density is constrained in the commercial using the Stark effect, which is caused by the collisions of emitting species with electrons. The Stark effect is a phenomenon where ion-electron collisions cause measured emission peaks to broaden, with peak width correlating to electron density as:

$$N_e = C\Delta\lambda^{\frac{3}{2}} \times 10^{19} \tag{C.1}$$

Where C is an experimentally determined constant (C = 35.8), and $\Delta\lambda$ is the full width at half maximum (FWHM) peak width of the emission line (constants and eq. C.1 from (Boumans, 1987). The Stark effect is especially prevalent on Balmer series emission, so electron density was calculated using the FWHM of the Hβ line at 468.1 nm where the effect is most pronounced

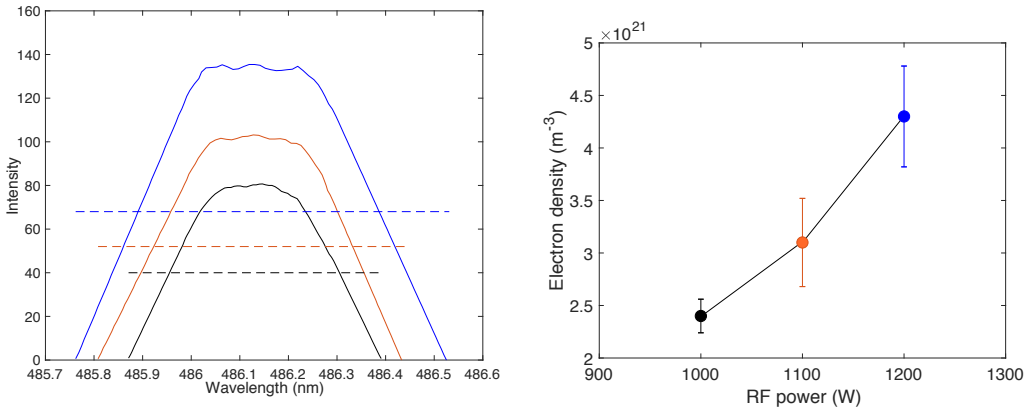

Fig. C.2: **(Left)** FWHM measurements of H_β emission for various outputs of plasma RF power. Peak width is used to calculate plasma electron density. **(Right)** Results of electron density estimates from peak width measurements.

Peak width measurements show a progressive increase in electron density with increasing RF forward power, with Ne values ranging from 2.4×10^{21} m^{-3} at 1000 W to 4.3×10^{21} m^{-3} at 1200 W (Fig. 2) In atmospheric pressure RF plasmas, the total particle density is 10^{24} m^{-3} with a typical Ar ion-neutral ratio of 10^{-3} at 7500 K (Niu and Houk, 1996). If we assume negligible electron contributions from 2^{+} cations in this plasma, these values for electron density reflect the typical ionization state of a commercial Ar plasma.

C.3 Temperature

The emission intensity of a spectroscopic peak is dependent on the number of emitting species and by the temperature of the system. The Boltzmann method of temperature measurement was used to determine ion and neutral excitation temperature in the plasma. The Boltzmann method uses the equation:

$$ln[\frac{\varepsilon\lambda}{A_{jk}g_{jk}}] = [-\frac{1}{k_BT}]E + ln[\frac{hcN_o}{4\pi}] \tag{C.2}$$

where ε is peak emissivity, λ is the wavelength, A_{jk} is the emission efficiency, g_{jk} is the statistical weight of each transition. This takes the form of a line, y = mx+b. Plotting the highest energy level of a transition against $ln[\frac{\varepsilon\lambda}{A_{jk}g_{jk}}]$ gives a linear trend, and the temperature of this system in units of K can be calculated from the slope as:

$$m = -\frac{1}{k_BT} \tag{C.3}$$

These plots give the temperature of the individual species, either an ion or neutral. In order to plot both ions and neutrals on the same plot, a correction is needed for the ion population for both the x and y axes. The correction applied to emission from the

population of ions is:

$$X = \begin{cases} E_j(neutral) \\ E_j + E_ion(ion) \end{cases} \tag{C.4}$$

$$Y = \begin{cases} ln[\frac{\varepsilon\lambda}{A_{jk}g_{jk}}](neutral) \\ ln[\frac{\varepsilon\lambda}{A_{jk}g_{jk}}] - ln[\frac{2\pi m_e k_b T}{h^3 N_e}]^{\frac{3}{2}}(ion) \end{cases} \tag{C.5}$$

The temperature found by Boltzmann plots of ion and neutral species is the excitation temperature, which is equal to the electron temperature (T_e) at atmospheric pressure. Thus using the T_e and N_e values calculated above, we estimate the Saha ionization efficiency of the measured analyte.

Temperature (K)	1,000 W	1,100 W	1,200 W
Zn	8,000 ± 240	8,200 ± 260	8,400 ± 270
Mg	8,100 ± 500	8,300 ± 580	8,400 ± 630
La	6,000 ± 1,100	6,100 ± 1,100	6,100 ± 1,200

Table C.1: Excitation temperatures for each analyte measured via linear Boltzmann method.

Saha Ionization efficiency (%)	1,000 W	1,100 W	1,200 W
Zn	76 ± 6%	78 ± 11%	79 ± 9%
Mg	98 ± 9%	99 ± 15%	98 ± 15%
La	98 ± 19%	98 ± 22%	98 ± 2%

Table C.2: Ionization efficiency estimated using the Saha equation, with values for Te calculated from linear Boltzmann temperature measurements and N_e from Stark broadening of Hβ lines.

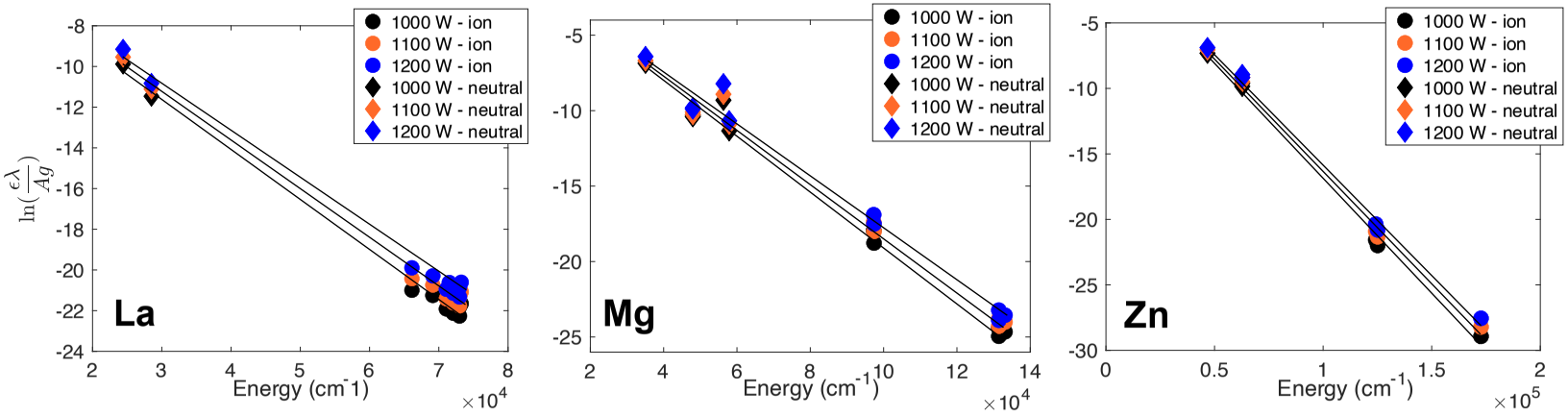

Fig. C.3: Linear Boltzmann plots calculated for La, Mg, and Zn, using measured emission from ion and neutral species.

C.4 Measurement of ion-neutral ratio

These Saha ionization efficiency values are compared to the measured ion-neutral ratio of emission lines from ion and neutral species in the plasma. The population densities of ions and neutrals are calculated from emission line intensities. The intensity of the emitting species is related to the population by:

$$N_o = \frac{\varepsilon}{4\pi h\nu A_{jk} g_{jk}} e^{\frac{E}{k_B T}} \tag{C.6}$$

Using observed emission lines from ion and neutral species, average ionization efficiencies for the three element species are 70% Zn, 96% Mg, and 98% La. The measured ionization efficiencies are within 2-5% of the predicted Saha ionization efficiencies, despite the large measurement uncertainties. These measurements show that the Saha equation produces estimates of analyte ionization with high accuracy and give confidence that it is an appropriate predictor of the ionization capabilities of the experimental plasma.

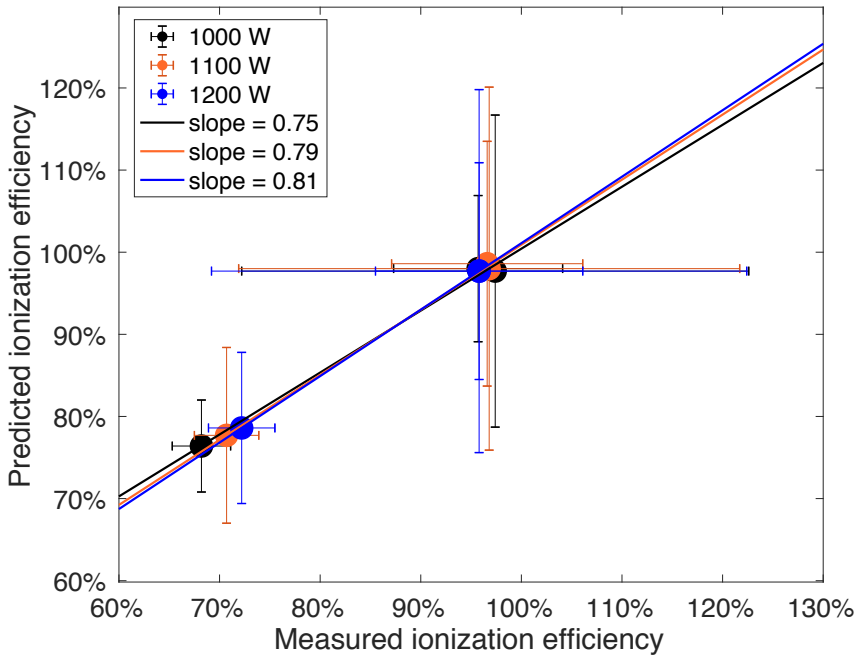

Fig. C.4: Comparison of analyte ionization efficiency predicted by the Saha equation based on spectroscopic T_e and N_e measurements compared to measured ion-neutral ratios. Data points for Mg, La, and Zn.

C.5 Plasma interaction with injected sample

During laser ablation sampling, a distribution of particle sizes spanning primarily between 25-150 nm in radius are generated (Moná et al., 2006); thus, the plasma needs to atomize particulates in this range. Here, we model the thermodynamics of the atomization process for this distribution of particle sizes. We also estimate the maximum mass loading the plasma can support and perform sample injection experiments with the plasma described in the main text.

C.5.1 Sample atomization

We calculate the total amount of energy needed to break all Si-O bonds in a silicate phase and assuming a spherical particle with uniform composition, conservatively modeled as pure SiO_2. This composition represents an upper limit of bond strengths in geologic materials (Si-O, 798 kJ/mol), as most ionic bonds (e.g. Fe-O, 409 kJ/mol) have lower bond strengths.

Ablated particles are injected into the plasma at high velocity and exposed to high gas temperatures for a transient amount of time. A gas flow rate of 200 SCCM (3.3 cm^3/s) through a sample injector tube with a 1 mm inner diameter achieves a gas velocity of $>$400 cm/s. If the end of the sample tube is positioned 1 cm distance from the orifice interfacing the plasma region, then a particle is exposed to the plasma environment for 2 ms. Based on this exposure time, we calculate the amount of energy that is imparted into a transient particle of rocky material as:

$$E = HtrT \tag{C.7}$$

Where H is the thermal conductivity of silica (e.g., 1.3 W m^{-1} K^{-1}), t is the time the particle is exposed to the plasma (in s), r is the particle radius (in m) and T is the plasma gas temperature (in K). Using this equation, we find that a spherical particle 25 nm in radius has

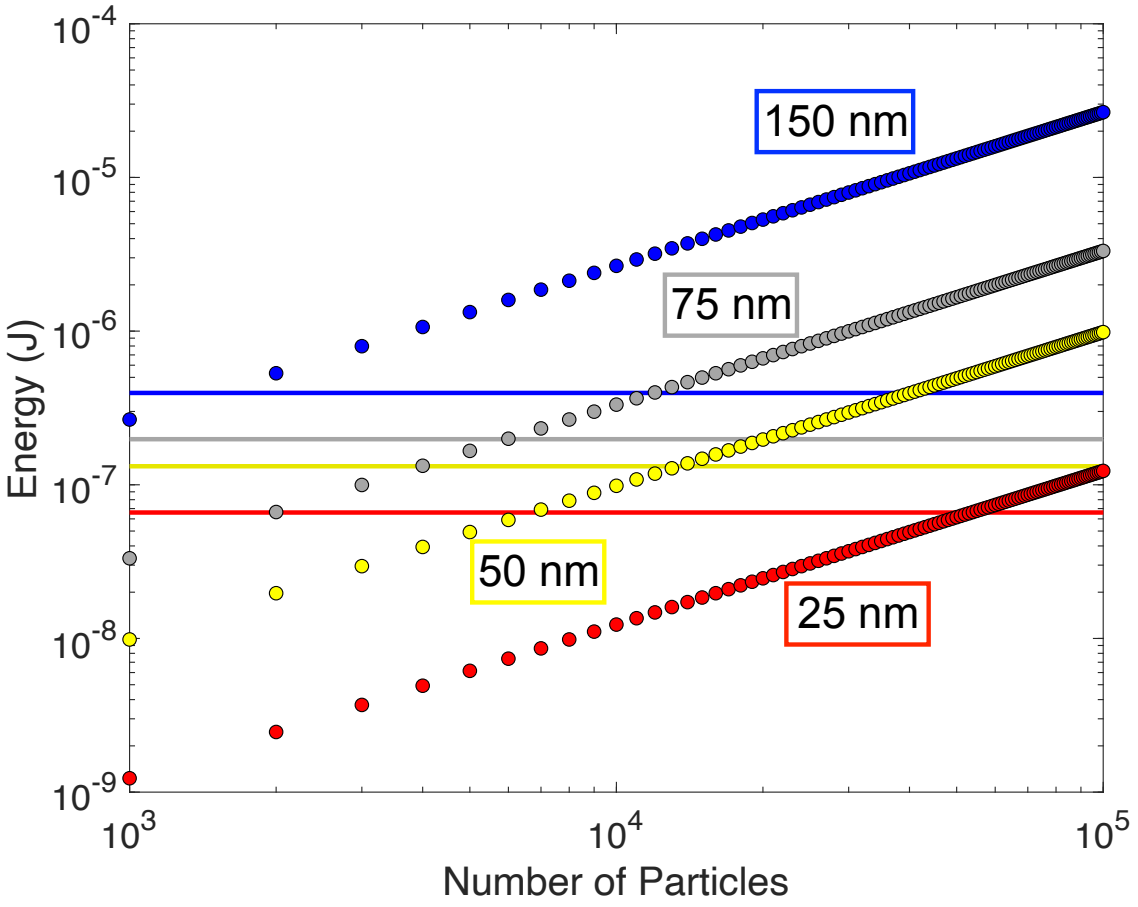

Fig. C.5: Thermodynamic model estimating atomization efficiency of the 19 W He plasma (500 K gas temperature) described in the main text. This model shows the relationship between particle diameter and total number of particles that the plasma can atomize during standard operations. The solid lines represent the maximum amount of energy available to a single particle of a certain diameter, and curved lines show the total amount of energy necessary to atomize a population of particles of that same diameter.

3.1×10^{-8} J imparted into the particle during exposure to a 500 K plasma, equivalent to the conditions measured for our He plasma at 19 W. Assuming a silicate particle with a mafic composition (Mg_2SiO_4, 140 g/mol), a 25 nm radius particle contains 1.5×10^{-18} moles. With a dissociation energy for Si-O bonds of 798 kJ/mol, that particle requires 1.2×10^{-12} J to completely dissociate that particle. Thus, a single particle is exposed to four orders of magnitude more energy than is needed for complete dissociation.

According to this model, a plasma at 500 K is capable of atomizing ∼44,000 particles with a 25 nm radius, or ∼1,600 particles with a radius of 150 nm during standard operations (Fig. S1). However, gas expansion during injection from the sampler tube could accelerate the particles, leaving their exposure time lower than previously calculated. Thus, these estimates of mass load represent an upper bound. Consequently, the maximum mass load that the plasma can atomize is estimated at $\sim2\times10^{-9}$ g/s, comparable to the mass generated during laser ablation processing of a 40 μm diameter sample spot with a repetition rate of 10 Hz (assuming 80 nm depth incised per shot; (Pisonero and Gunther, 2008)).

C.5.2 Sample gas injection

A plasma was generated with 200 SCCM of He at 19 W of forward power, and varying amounts of N_2 (representing analyte) were mixed in with the He plasma gas. Fig. 2 shows the measurements of ion current and electron density with increasing N_2 gas flow into the plasma. As the sample N_2 gas flow was increased, the ion current and electron density in the plasma source both decreased, showing a reduction in plasma performance with increasing sample mass load.

From the ideal gas law, a 10 SCCM gas flow rate is equivalent to 1×10^{-4} g/s of N_2 (Fig. S2), greater than the maximum mass loading the plasma can support ($\sim5\times10^{-9}$ g/s, as described above).

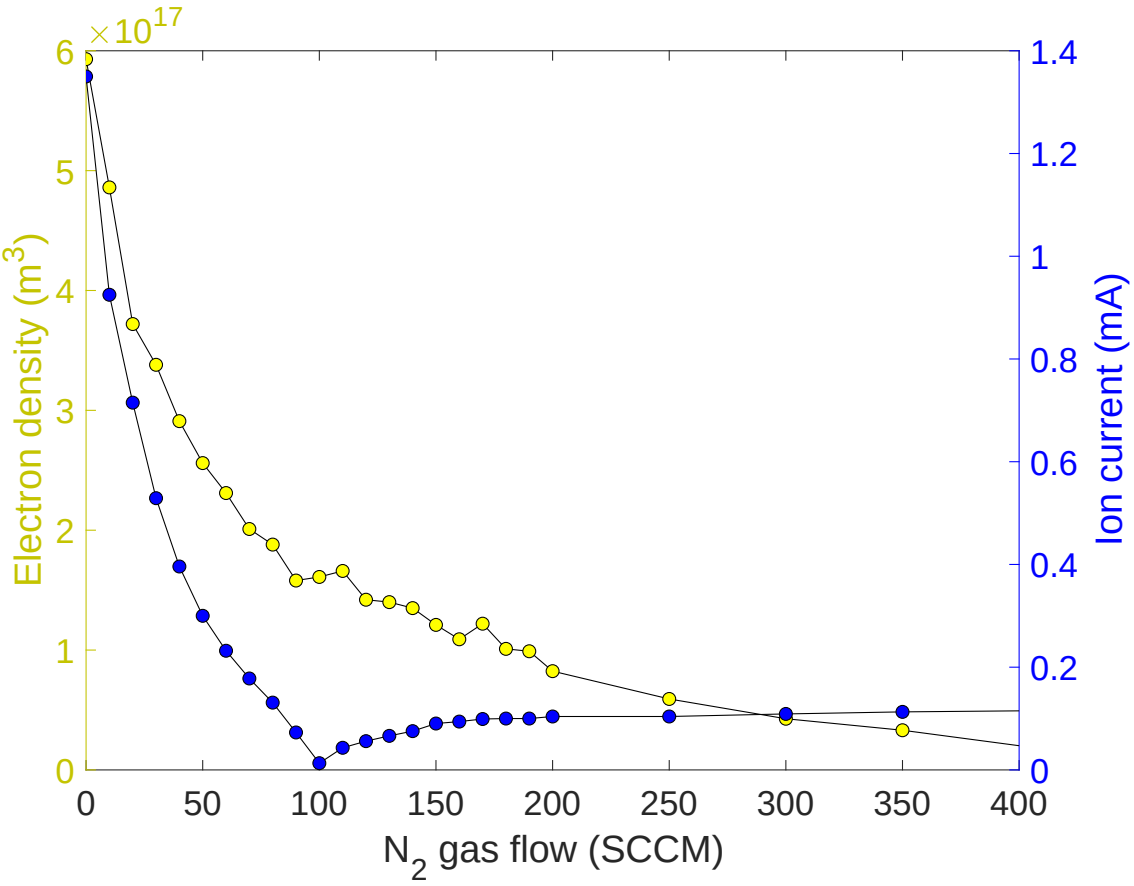

Fig. C.6: Measurements of the electron density and ion current of the plasma as a function of introduced N2 sample gas. Sample gas was mixed into a He plasma of 200 SCCM gas flow rate and 19 W of forward power.

Appendix D: A miniature ICPMS for in situ planetary science

D.1 Pressure Estimate of the Plasma Torch Region

The method of calculating chamber conductance will depend on the flow regime, which changes as a function of pressure. In an environment with a sufficiently high pressure, the movement of individual gas particles in the chamber can be estimated as analogous to a liquid flowing through a constrained area if the pressure is high enough, known as continuum flow. If the pressure is low enough that a particle is more likely to collide with a wall of the chamber than with another gas molecule, then the gas can be modeled as molecular flow. A pressure regime between molecular flow and continuum flow is known as transitional flow, in which the gas can be modeled as neither a fluid or as a set of individual particles. Prior to calculating the conductance of each component, the flow regime can be estimated based on the Knudsen number (K_n):

$$K_n = \frac{\lambda}{r} \tag{D.1}$$

Where λ is the mean free path of the particle, and r is the radius of the chamber. This ratio defines the flow regime of the system, as:

$$\begin{gathered} K_n > 1 \text{ molecular flow,} \\ 1 > K_n > 0.01 \text{ transitional flow,} \\ K_n < 0.01 \text{ continuum flow.} \end{gathered}$$

In order to calculate the K_n value, the mean free path of the system must be calculated, as:

$$\lambda = \frac{RT}{\sqrt{2}\pi d^2 N_A P} \tag{D.2}$$

Where R is the ideal gas constant ($J \cdot mol^{-1} \cdot K^{-1}$), T is the temperature of the gas (K), N_A is Avogadro's number, d is the particle diameter (m), and P is the system pressure (Pa). The proposed setup uses small orifices to restrict the flow of gas from one chamber to the next, and the relationship between gas flow, orifice diameter, and chamber pressure is well established. If the flow of a gas through an orifice is calculated as:

$$flow(cm^3/s) = 0.01749 \cdot \frac{P_1}{29.7} \cdot \sqrt{\frac{29}{m_{gas}}} \cdot \sqrt{\frac{528}{T}} \cdot D^2 \tag{D.3}$$

Where P_1 is the pressure in the tube (PSI), m_{gas} is the atomic weight of the gas molecule (g/mol), and D is the orifice diameter (μm), then the pressure of the tube can be estimated if the gas flow and orifice diameter are known. Using a 1-mm orifice diameter, and 10 sccm gas flow of Ar at 250 °C (523 K), this gives a pressure in the plasma torch of 1.1 torr (1.6 mbar, 160 Pa). And while the calculated pressure here is a first order approximation, other factors such as conductance and pumping speed will be considered for a more accurate pressure estimate of the torch.

Using the calculated torch pressure as an assumed starting point, I calculate a mean free path of $\sim$83 μm inside the plasma environment. This metric, as well as the 10 mm ID of the plasma tube, that gives a K_n value of 0.083 mm/10 mm = 0.0083, which indicates that the gas flow in the torch environment can be modeled as continuum flow for the purposes of conductance calculations. From here, I assume molecular flow for the remaining sections and continuum flow for the torch section.

Because the flow in the gas tube is calculated to be in the continuum flow regime due to the K_n value being $<$0.01, a different method of calculating conductance is needed for this portion of the instrument. The high pressure of the torch is interfaced via a 1-mm orifice,

which can be modeled as gas flow through a nozzle. Nozzle gas flow is calculated as:

$$q_pV = A_{min}\sqrt{\frac{\pi}{4}}P_1 \nu \psi(\frac{P_2}{P_1}) \tag{D.4}$$

Where q_pV is the throughput, A_{min} = 0.86*D, and D is the orifice diameter (m). ψ is the maximum value for the flow function (*unitless*), which is 0.513 for inert gases such as Ar. P_1 and P_2 are the different pressures on either side of the orifice (Pa).

When modeling the flow of gas as continuous flow, further calculations are needed to decipher whether the flowing gas travels in a straight, laminar pattern, or as a chaotic turbulent flow pattern. The transition from laminar to chaotic flow is characterized by the Reynolds number:

$$R_e = \frac{32}{\pi^2}\cdot\frac{q_pV}{\eta \nu D}\begin{cases} < 2300 & \text{laminar viscous flow} \\ > 4000 & \text{turbulent flow} \end{cases} \tag{D.5}$$

Where η is the viscosity of the gas (η_{Ar} =4.6$\times 10^{-5}$ Pa·s at 500 °C). Using the value calculated from eq. D.4, as well as other gas constants, the Reynolds number is calculated to be 845, showing the flow through the plasma torch can be modeled as laminar flow. The conductance of a tube with laminar flowing gas is calculated as:

$$C_{T,lam} = \frac{\pi}{256}\cdot\frac{1}{\eta}\cdot\frac{D^4}{L}\cdot(P_1+P_2) \tag{D.6}$$

The interface region consists of a 7 cm (2.75 in) CF cube, with a 60 L/s turbo pump interfaced via a conical reducer flange (Fig. 5.6). The conductance of the CF cube was calculated assuming a tube-shaped geometry, with a 7.6 cm (3 in) length and a 3.3 cm (1.33 in) inner diameter, giving a conductance of 2.3 m^3/s. The conductance of the conical reducer is dependent on the ratio of both diameters, and is calculated as 0.016 m^3/s. This

shows that the conical reducer acts as a conductance limiting component, and even a larger pump with an increased pumping speed would have minimal effect on the ultimate system pressure. Adding the conductances together in series as $\frac{1}{c_{tot}} = \frac{1}{c_{cone}} + \frac{1}{c_{cube}}$ gives a total conductance of 0.0161 m^3/s or 16 L/s. With a 60 L/s nominal pumping speed and this calculated conductance, this gives an effective pumping speed of this component of 12.7 L/s.

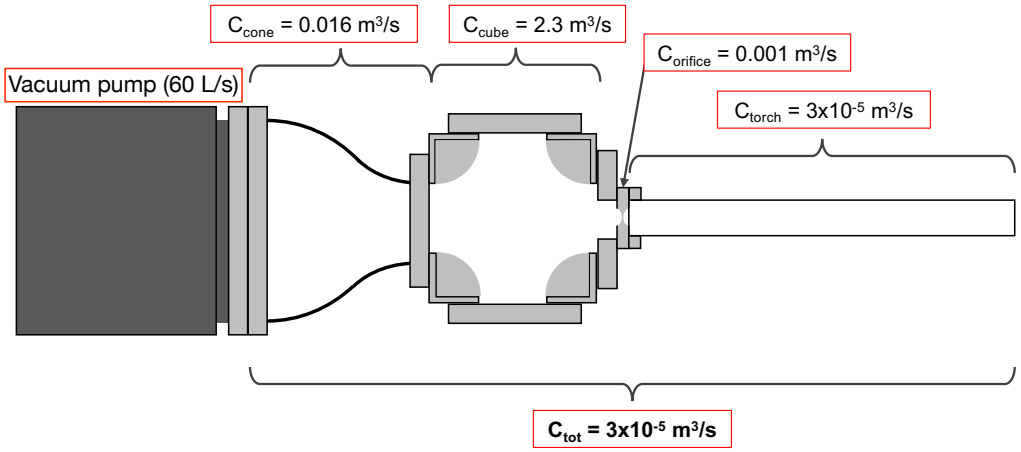

Fig. D.1: Summary of conductances of individual components comprising the interface and torch regions. The pumping in the torch region is dependent on the conductance of the interface region, so both conductances are added in series for this calculation.

The conductance of the torch had already been calculated using the above formulae, under continuous, laminar flow. The conductance of a tube is lower in continuous flow than in molecular flow, as reflected by the significantly lower conductance of the torch itself at high gas flow (3×10^{-5} m^3/s). Because the torch is pumping through the 1-mm orifice, the conductance of the torch is calculated including the conductance of the orifice as well as the interface region as well (Fig. D.1). The low conductance of the torch pumping through the orifice at high gas flow results in a high pressure in the torch system, with an effective pumping speed in the torch region of 0.025 L/s.

Considering the QMS and interface, all observed pressures remain within a factor of

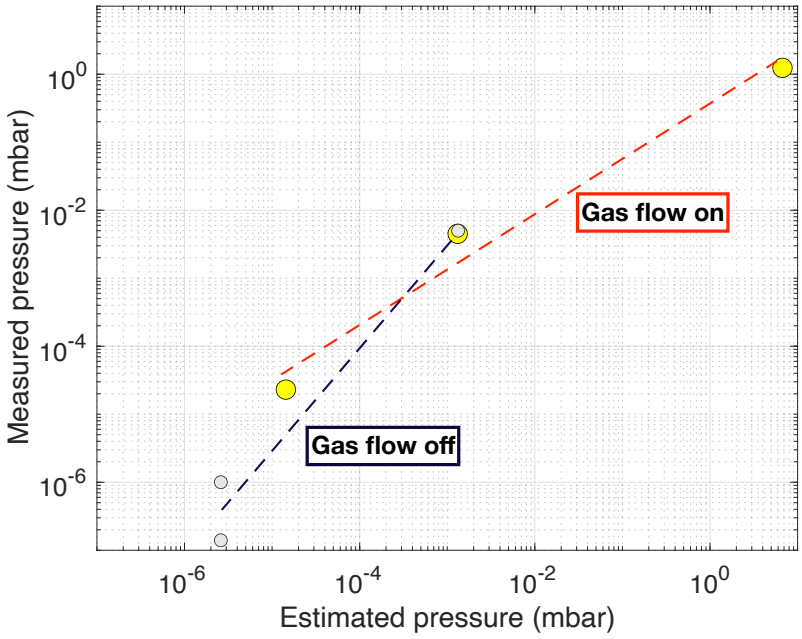

Fig. D.2: Comparison of calculated pressure in each subsystem in the chamber to the observed pressure, with 10 SCCM of Ar gas on and gas off.

2-5× their pressure estimates across 7 orders of magnitude (Fig. D.2).

D.2 Photos of ICPMS chamber development

The buildup of the prototype ICPMS included construction of the vacuum chamber housing, with integration of DC electrodes to guide the ion flight path. Each step in the buildup involved the construction and integration of custom electrostatic lenses, and experiments quantifying the amount of ion current delivered through each electrode. While the details and results of each experiment are detailed in the main text of chapter 5, this section contains photographs of the chamber construction. Here, I detail the electrodes used to manipulate ion trajectory, the chamber setup during ion current optimization experiments, and the integration of the QMS to the plasma ion source.

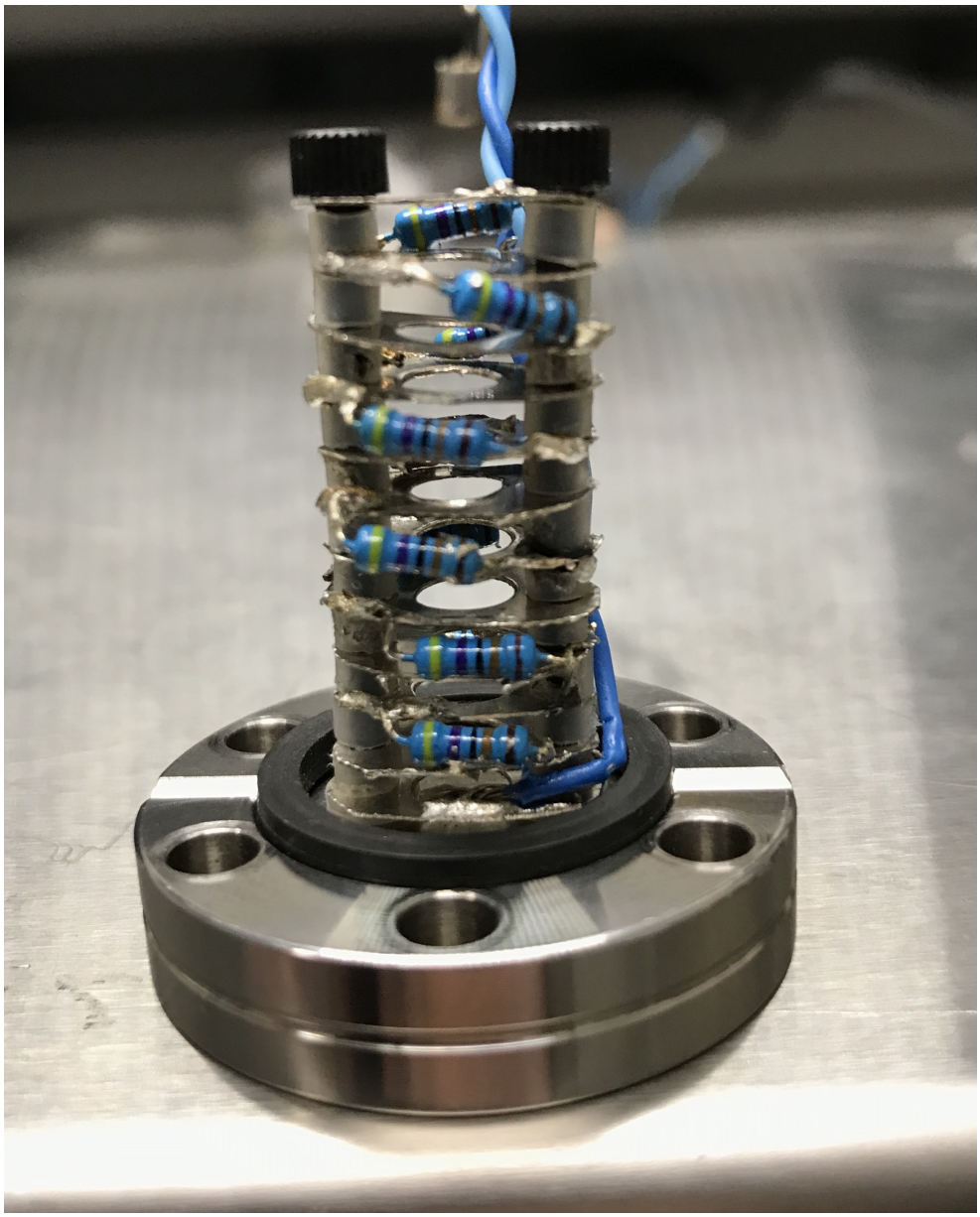

Fig. D.3: Photo of the ion lens stack. The stack was constructed from nickel shim stock and the electrodes are separated by nylon insulating spacers. Each electrode in the stack is connected to the previous electrode via 410 kΩ resistors soldered onto the electrode plate. The stack is held in place by two insulating nylon screws, interfaced to the CF aperture plate. Two separate voltages are applied to the stack, one at the initial electrode closest to the aperture, and another to the second electrode which applied voltage to the rest of the stack through the resistor network.

Fig. D.4: Photos showing the collector plates used in the 90° deflector experiments. **(Top Left)** Collector plate was made from nickel shim stock and mounted onto a CF electrical feedthrough, allowing measurement of ion current onto the nickel plate. **(Top Right)** Side view showing mounting setup of nickel plate. A rigid wire was soldered to the plate, keeping it in place during experiments and connecting the plate to the feedthrough. **(Bottom)** Photo of the collector plate in place inside the interface chamber. An identical collector plate and CF feedthrough setup was installed on the opposite side of the 90° deflector as well.

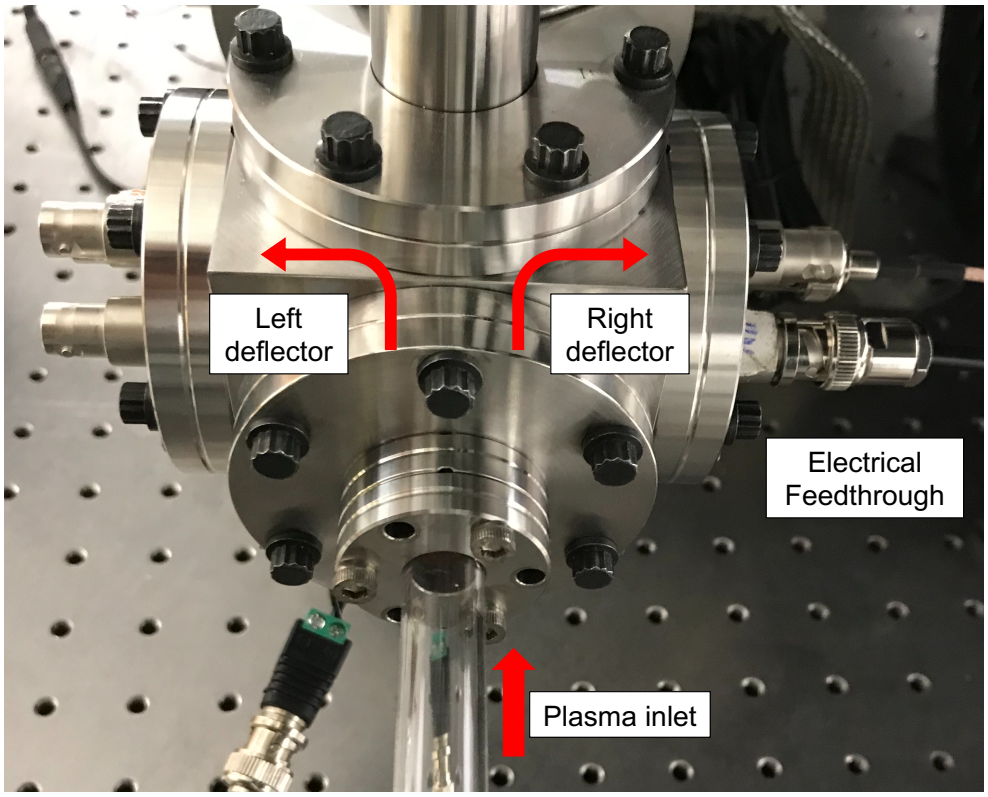

Fig. D.5: Photo of the interface chamber depicting the direction of ion trajectory deflection by the 90° deflector. A nickel collector plate is mounted to either side of the deflector, with current measured on each CF feedthrough.

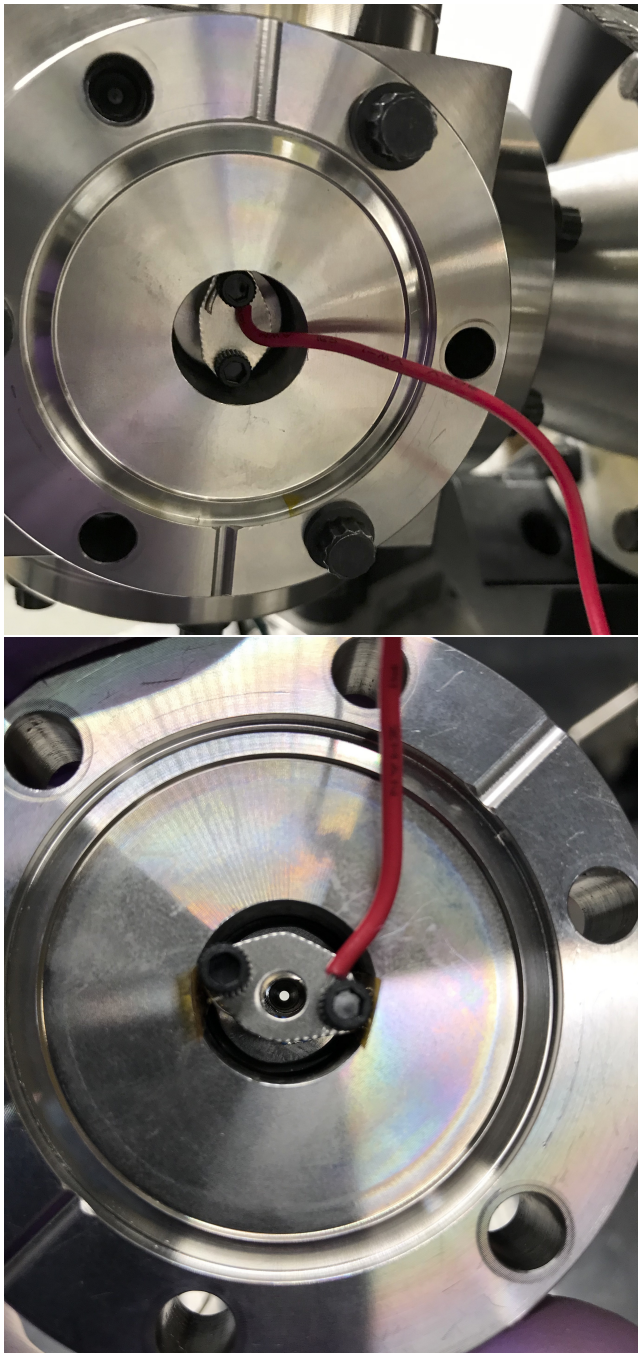

Fig. D.6: Photos of the backside of the second aperture depicting electrode setup leading into the QMS chamber. **(Top)** Photo showing collector plate setup on the backside of the second aperture. Ion current measurements were made after this aperture to test ability to steer ions into the QMS chamber and quantify ion loss. **(Bottom)** The collector plate was replaced by a stack of electrodes to reduce ion energy and columnate the beam. Both collector plate and stack are connected to a separate CF electrical feedthrough in the QMS chamber.

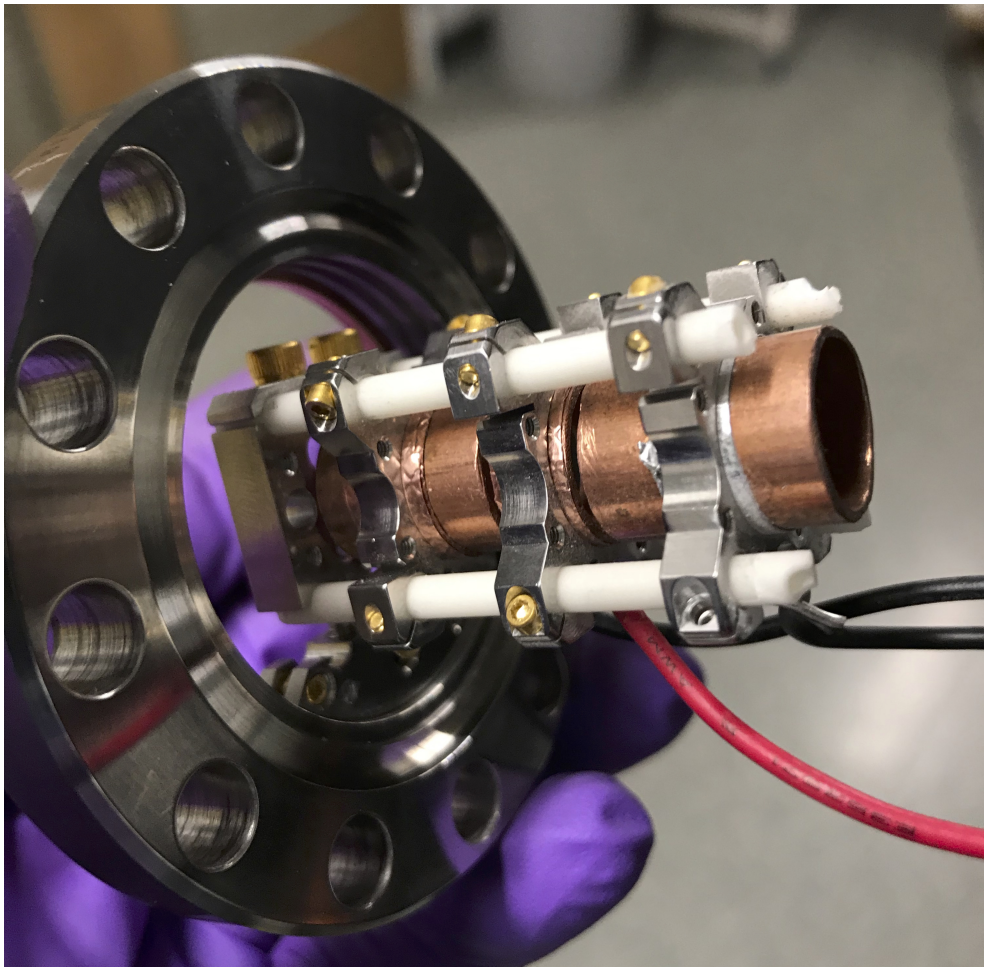

Fig. D.7: Photo of custom built Einzel lens. The lens is used to focus the incoming columnated beam to a smaller beam diameter, reducing beam dispersion for better peak resolution. The Einzel lens consists of three separate electrodes, with the first and third held at ground and the second brought to a variable voltage for focusing. Each electrode is isolated from the others by insulating alumina rods, which also hold the lens setup in place.

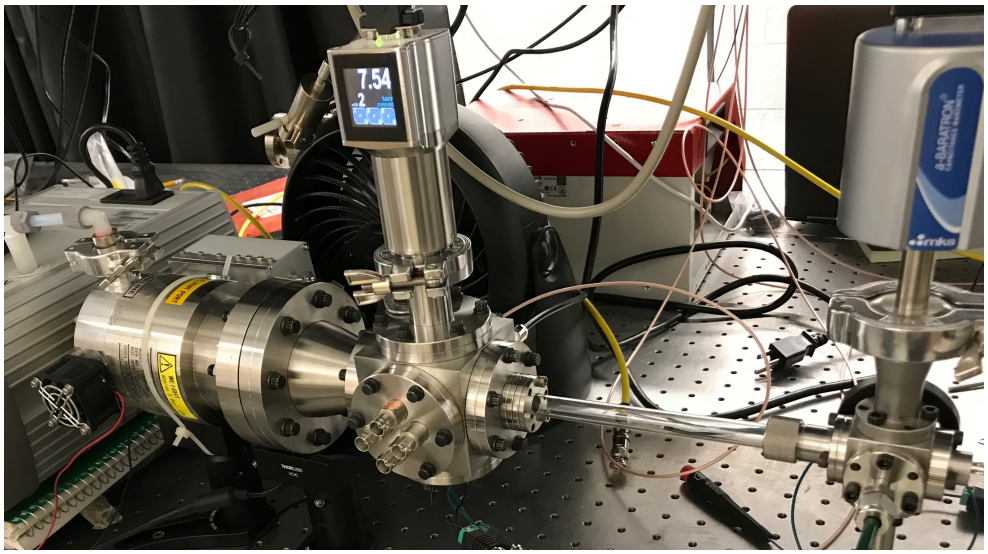

Fig. D.8: Photo of the initial chamber setup, depicting the plasma torch integrated to the interface region with no QMS. This is the configuration that the 90° deflector experiments were carried out on.

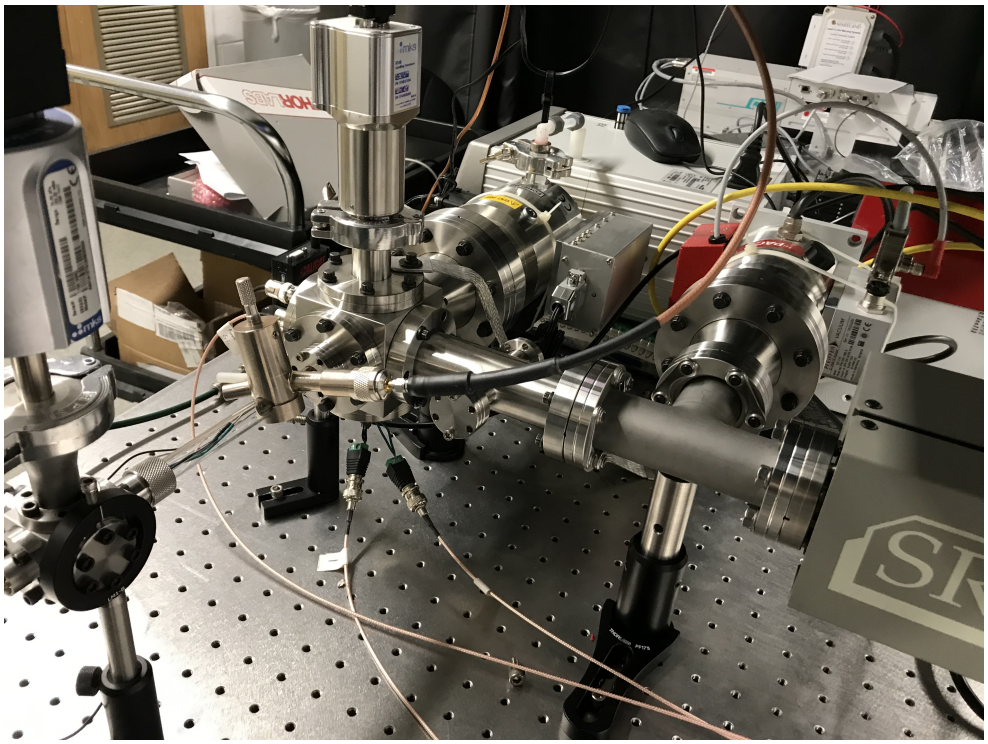

Fig. D.9: Progressive buildup of the ICPMS prototype instrument, showing the integration of the QMS chamber to the interface chamber.

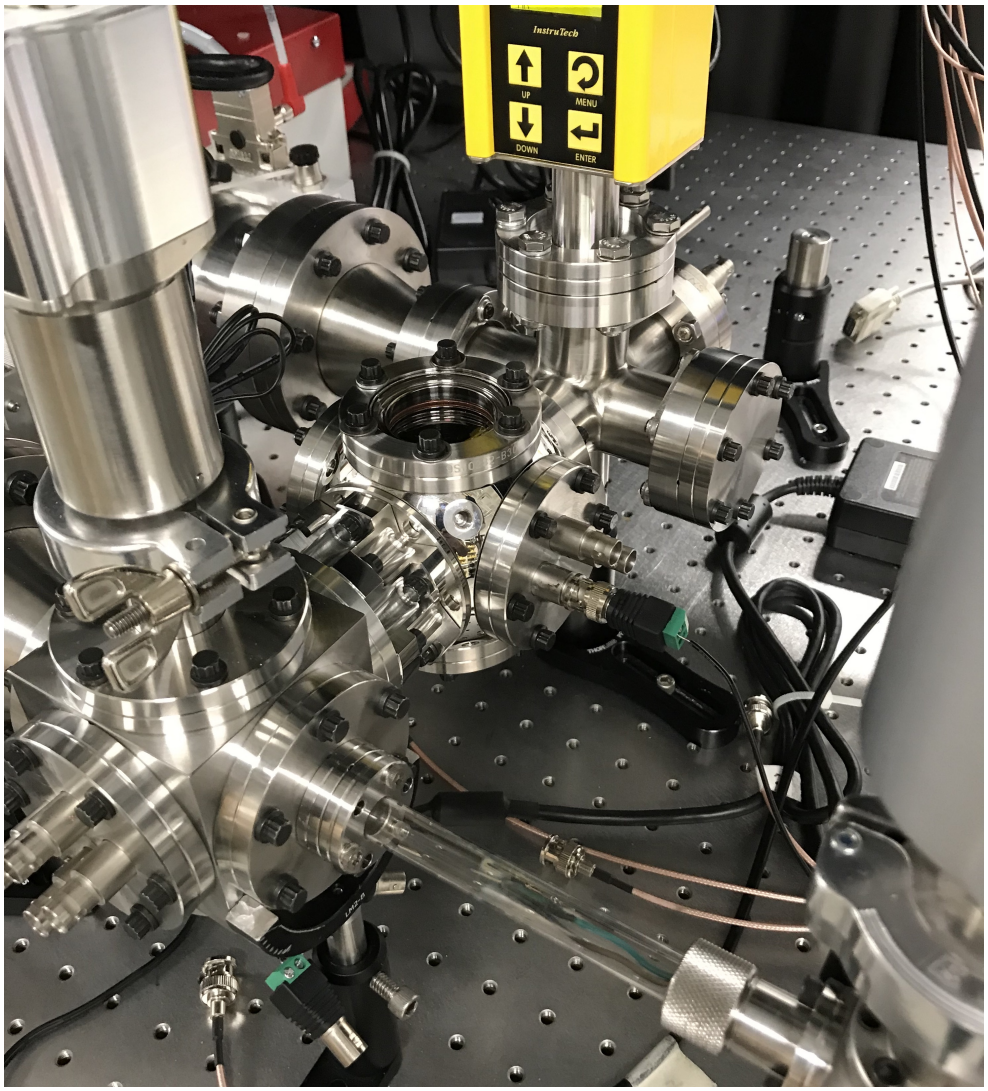

Fig. D.10: Final ICPMS chamber configuration

D.3 Accuracy of Kr isotope ratios measured using RGA filament ion source

Prior to analysis of input Kr sample via the plasma, the accuracy, precision, and total ion current of the Kr isotopes and their ratios was measured using the ionization filament on the front end of the QMA. This was done as a baseline measurement of the QMA performance in order to establish the extent of performance loss due to the ion beam delivery to the QMA. Here, the same Kr gas input rate (1 SCCM) was for continuity with the sample analysis experiments. The electron filament was turned on to measure the ambient background gas composition including the input Kr.

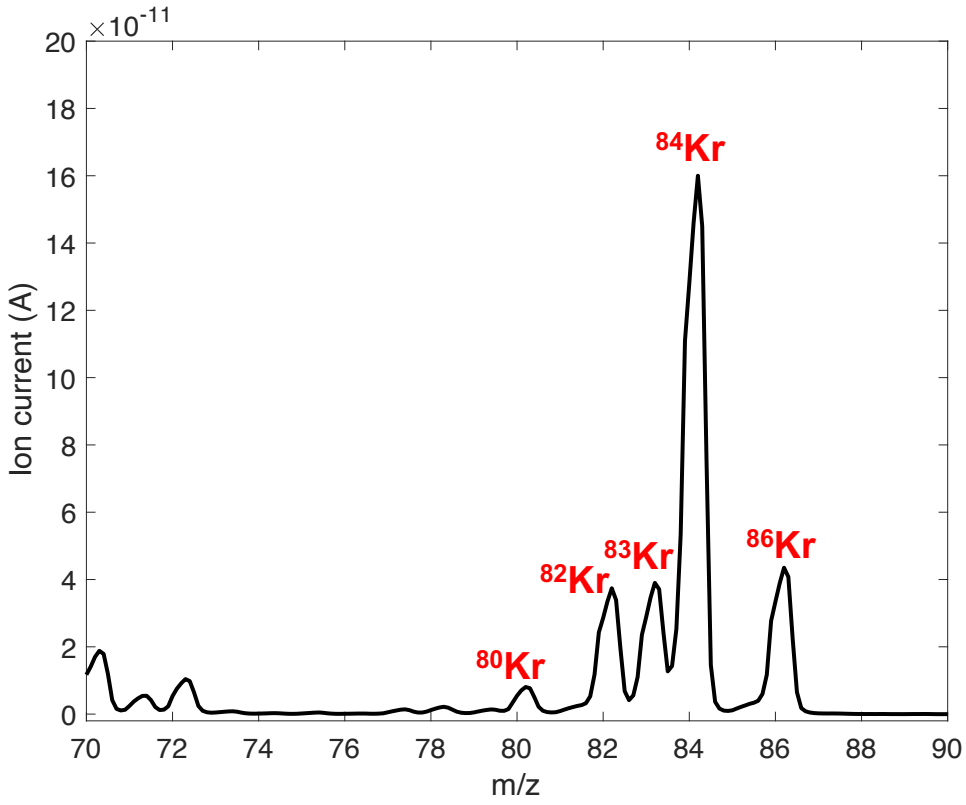

Fig. D.11: Mass spectrum showing isotopes of Kr measured using the QMA with the ionization filament as the ion source.

The individual isotopes of Kr were selected for a timescan, measured in peak-jumping mode over an 80 second chromatogram. Similar to the analyses described in chapter D, the

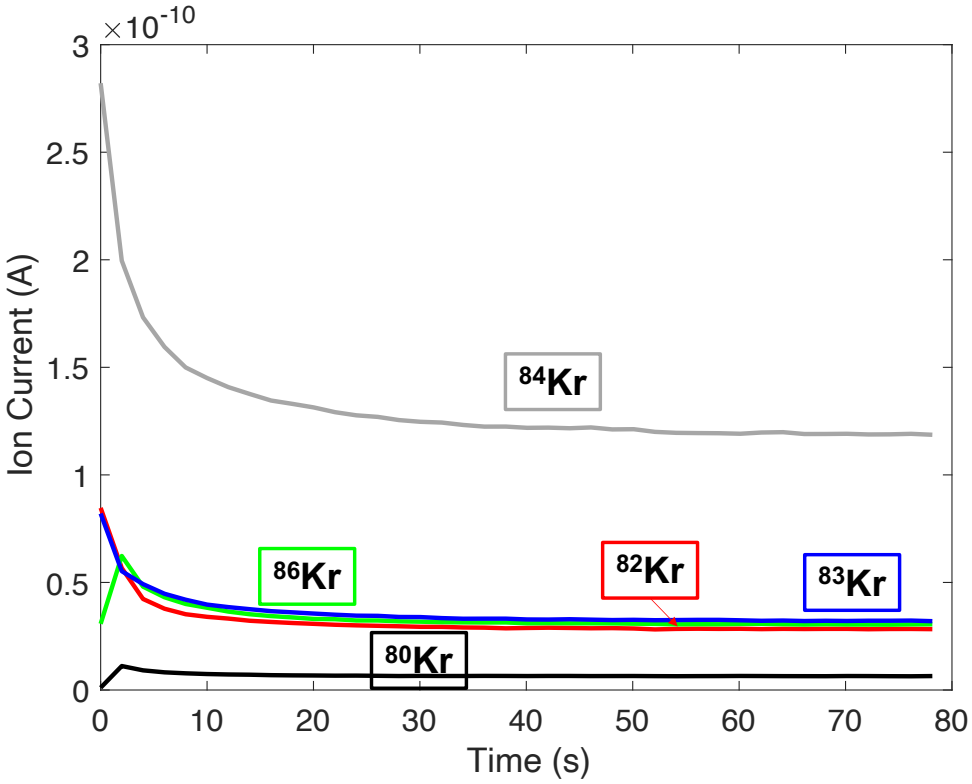

Fig. D.12: Chromatogram of individual isotopes of Kr, using the filament as the ion source.

signal was monitored over the collection time and the mass signal was averaged over the length of the chromatogram (excluding the first 10 seconds of the scan). The uncertainty of each isotope abundance is derived from the uncertainty of the measured signal.

The signal of each isotope abundance observed via the filament is $10^3\times$ higher than the Kr produced via the Ar plasma. The uncertainty of each mass channel ranges from $\pm 1.3\%$ to $\pm 2.8\%$, in contrast to the $\pm 3.4\%$ to $\pm 15.5\%$ uncertainty measured on the Kr chromatogram delivered from the plasma.

Finally, the isotope ratios of Kr, as well as their precision and accuracy, were calculated using the ion current signal at each mass channel. Unlike the measurements made from the plasma ion source, the isotope ratios were left uncorrected for instrument induced fractionation. This is because the ion source is located at the front entrance of the QMA, so

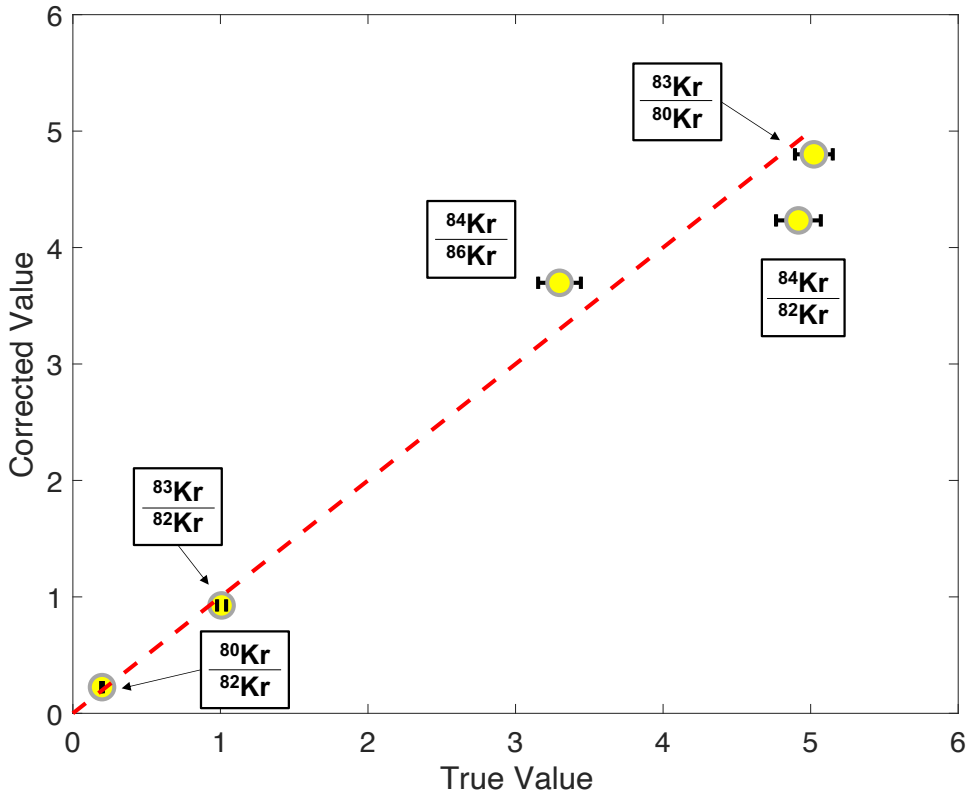

Fig. D.13: Accuracy of Kr isotope ratios relative to true values, measured using filament as the QMA ion source.

the ion beam interacts with minimal electrostatics prior to mass analysis, minimizing ratio fractionation.

The isotope ratios measured are accurate to within 5% to 16% of the true values, with ratio precision ranging from 2.6% to 4%. These performance metrics are more accurate and precise than the chromatogram derived from the plasma ion beam, although the ratio uncertainty is also reduced due to no isotope ratio corrections being applied to this dataset. Regardless, isotope ratios measured using the filament ion source resulted in a factor of $\sim 10\times$ higher precision with $10^3\times$ higher ion signal. Thus, future work is needed to increase the magnitude of ion beam delivery to further improve the precision and accuracy of elemental abundance measurements.

Ratio	True Ratio	Measured Ratio	Accuracy	Precision (1 σ)
^{80}Kr/^{82}Kr	0.20	0.22	57%	2.6%
^{82}Kr/^{83}Kr	1.01	0.93	42%	3.3%
^{83}Kr/^{80}Kr	5.02	4.8	25%	2.6%
^{84}Kr/^{82}Kr	4.9	4.2	0.9%	3.6%
^{84}Kr/^{86}Kr	3.3	3.7	20%	3.9%

Table D.1: Results of measured Kr isotope ratio accuracy relative to true value, and associated measurement precision. Kr isotope abundances measured using the filament ion source at the entrance of the SRS RGA. The measured ratios reported here are not corrected for instrument-induced ratio fractionation.

Bibliography

[1] Francis Albarède and Brian Beard. Analytical methods for non-traditional isotopes. *Reviews in mineralogy and geochemistry*, 55(1):113–152, 2004.

[2] Anastasia Albert, Jacob T Shelley, and Carsten Engelhard. Plasma-based ambient desorption/ionization mass spectrometry: state-of-the-art in qualitative and quantitative analysis. *Analytical and bioanalytical chemistry*, 406(25):6111–6127, 2014.

[3] Claude J Allègre, Albrecht Hofmann, and Keith O'Nions. The argon constraints on mantle structure. *Geophysical Research Letters*, 23(24):3555–3557, 1996.

[4] Claude J. Allègre, Jean-Paul Poirier, Eric Humler, and Albrecht W. Hofmann. The chemical composition of the Earth. *Earth and Planetary Science Letters*, 134(3):515–526, 1995.

[5] Abigail Allwood, Ben Clark, David Flannery, Joel Hurowitz, Lawrence Wade, Tim Elam, Marc Foote, and Emily Knowles. Texture-specific elemental analysis of rocks and soils with PIXL: The Planetary Instrument for X-ray Lithochemistry on Mars 2020. In *2015 IEEE Aerospace Conference*, pages 1–13. IEEE, 2015.

[6] Scott Anderson, Jonathan Levine, and Tom Whitaker. Dating a Martian meteorite with 20 Myr precision using a prototype in-situ dating instrument. *Planetary and Space Science*, page 105007, 2020.

[7] Tomoko Arai, Hiroshi Takeda, Akira Yamaguchi, and Makiko Ohtake. A new model of lunar crust: asymmetry in crustal composition and evolution. *Earth, planets and space*, 60(4):433–444, 2008.

[8] R Arevalo and William F McDonough. Gallium and germanium abundances in MORB and OIB: evidence for pyroxenitic source components. *Geochim Cosmochim Acta*, 74:A32, 2010.

[9] Ricardo Arevalo and William F McDonough. Chemical variations and regional diversity observed in morb. *Chemical Geology*, 271(1-2):70–85, 2010.

[10] Ricardo Arevalo, William F. McDonough, and Mario Luong. The K/U ratio of the silicate Earth: Insights into mantle composition, structure and thermal evolution. *Earth and Planetary Science Letters*, 278(3-4):361–369, 2009.

[11] Ricardo Arevalo, William F McDonough, Andreas Stracke, Matthias Willbold, Thomas J Ireland, and Richard J Walker. Simplified mantle architecture and distribution of radiogenic power. *Geochemistry, Geophysics, Geosystems*, 14(7):2265–2285, 2013.

[12] Ricardo Arevalo Jr, William F McDonough, and Mario Luong. The k/u ratio of the silicate earth: Insights into mantle composition, structure and thermal evolution. *Earth and Planetary Science Letters*, 278(3-4):361–369, 2009.

[13] Ricardo Arevalo Jr, Ziqin Ni, and Ryan M Danell. Mass spectrometry and planetary exploration: A brief review and future projection. *Journal of Mass Spectrometry*, 55(1):e4454, 2020.

[14] Ricardo Arevalo Jr, Laura Selliez, Christelle Briois, Nathalie Carrasco, Laurent Thirkell, Barnabé Cherville, Fabrice Colin, Bertrand Gaubicher, Benjamin Farcy, Xiang Li, et al. An orbitrap-based laser desorption/ablation mass spectrometer designed for spaceflight. *Rapid Communications in Mass Spectrometry*, 32(21):1875–1886, 2018.

[15] Melanie Barboni, Patrick Boehnke, Brenhin Keller, Issaku E Kohl, Blair Schoene, Edward D Young, and Kevin D McKeegan. Early formation of the Moon 4.51 billion years ago. *Science advances*, 3(1):e1602365, 2017.

[16] K Biemann, JIIIPT Oro, Priestley Toulmin III, LE Orgel, AO Nier, DM Anderson, PG Simmonds, D Flory, AV Diaz, DR Rushneck, et al. The search for organic substances and inorganic volatile compounds in the surface of Mars. *Journal of Geophysical Research*, 82(28):4641–4658, 1977.

[17] David Blake, David Vaniman, Cherie Achilles, Robert Anderson, David Bish, Tom Bristow, Curtis Chen, Steve Chipera, Joy Crisp, David Des Marais, et al. Characterization and calibration of the CheMin mineralogical instrument on Mars Science Laboratory. *Space Science Reviews*, 170(1-4):341–399, 2012.

[18] Lars E Borg, William S Cassata, Josh Wimpenny, Amy M Gaffney, and Charles K Shearer. The formation and evolution of the moon's crust inferred from the sm-nd isotopic systematics of highlands rocks. *Geochimica et Cosmochimica Acta*, 290:312–332, 2020.

[19] Lars E Borg, Amy M Gaffney, and Charles K Shearer. A review of lunar chronology revealing a preponderance of 4.34–4.37 ga ages. *Meteoritics & Planetary Science*, 50(4):715–732, 2015.

[20] AM Borst, BH Foing, GR Davies, and W Van Westrenen. Surface mineralogy and stratigraphy of the lunar south pole-aitken basin determined from clementine UV/VIS and NIR data. *Planetary and Space Science*, 68(1):76–85, 2012.

[21] P W J M Boumans. *Theory of Spectrochemical Excitation*. Hilger & Watts, London, 1966.

[22] P W J M Boumans. *Inductively Coupled Plasma Emission Spectroscopy Part II: applications and fundamentals. Volume 2*. John Wiley & Sons, Inc., 1987.

[23] I G Brown. Ion temperature in a 'cold' microwave-produced plasma. *Plasma Physics*, 18:205–209, 1976.

[24] James Camparo and Gilda Fathi. Effects of rf power on electron density and temperature, neutral temperature, and Te fluctuations in an inductively coupled plasma. *Journal of Applied Physics*, 105(10):103302, 2009.

[25] JL Campbell. The instrumental blank of the mars science laboratory alpha particle x-ray spectrometer. *Nuclear Instruments and Methods in Physics Research Section B: Beam Interactions with Materials and Atoms*, 288:102–110, 2012.

[26] Robin M Canup, Channon Visscher, Julien Salmon, and Bruce Fegley Jr. Lunar volatile depletion due to incomplete accretion within an impact-generated disk. *Nature geoscience*, 8(12):918–921, 2015.

[27] Francis F Chen and Jane P Chang. *Principles of Plasma Processing*. Plenum/Kluwer Publishers, 2002.

[28] Xi Chen and Peng Han. On the thermodynamic derivation of the saha equation modified to a two-temperature plasma. *Journal of Physics D: Applied Physics*, 32(14):1711, 1999.

[29] Chinwook Chung. Experimental investigation on the floating potential of cylindrical Langmuir probes in non-Maxwellian electron distributions. *Physics of Plasmas*, 12(12):1–3, 2005.

[30] Benton C Clark, AK Baird, Harry J Rose, Priestley Toulmin, Ralph P Christian, Warren C Kelliher, Angelo J Castro, Catherine D Rowe, Klaus Keil, and Gary R Huss. The Viking X-ray fluorescence experiment: Analytical methods and early results. *Journal of Geophysical Research*, 82(28):4577–4594, 1977.

[31] Sydney P Clark and AE Ringwood. Density distribution and constitution of the mantle. *Reviews of Geophysics*, 2(1):35–88, 1964.

[32] Danielle Cleveland, Peter Stchur, Xiandeng Hou, Karl X Yang, Jack Zhou, and Robert G Michel. Resonant laser ablation of metals detected by atomic emission in a microwave plasma and by inductively coupled plasma mass spectrometry. *Applied spectroscopy*, 59(12):1427–1444, 2005.

[33] Robert B Cody, James A Laramée, and H Dupont Durst. Versatile new ion source for the analysis of materials in open air under ambient conditions. *Analytical chemistry*, 77(8):2297–2302, 2005.

[34] B Cohen, K Young, N Zellner, K Zacny, A Yingst, R Watkins, R Warwick, S Valencia, T Swindle, S Robbins, N Petro, A Nicoletti, D Moriarty, R Lynch, S Indyk, J Gross, J Grier, J Grant, A Ginyard, C Fassett, K Farley, B Farcy, B Elhmann, D Dyar, G Daelemans, N Curran, C van der Bogert, R Arevalo, and S Anderson. In situ geochronology for the next decade: Mission designs for the moon, mars, and vesta. *Journal of Planetary Science*, 2020.

[35] Barbara A Cohen, J Scott Miller, Zheng-Hua Li, Timothy D Swindle, and Renee A French. The Potassium-Argon Laser Experiment (KA r LE): In Situ Geochronology for Planetary Robotic Missions. *Geostandards and Geoanalytical Research*, 38(4):421–439, 2014.

[36] Logan M Combs, Arya Udry, Geoffrey H Howarth, Minako Righter, J Lapen, Juliane Gross, Daniel K Ross, Rachel R Rahib, and James M D Day. Petrology of the enriched poikilitic shergottite Northwest Africa 10169 :. *Geochimica et Cosmochimica Acta*, 2019.

[37] Logan M Combs, Arya Udry, Geoffrey H Howarth, Minako Righter, Thomas J Lapen, Juliane Gross, Daniel K Ross, Rachel R Rahib, and James MD Day. Petrology of the enriched poikilitic shergottite Northwest Africa 10169: Insight into the martian interior. *Geochimica et Cosmochimica Acta*, 266:435–462, 2019.

[38] JN Connelly and Martin Bizzarro. Lead isotope evidence for a young formation age of the earth–moon system. *Earth and Planetary Science Letters*, 452:36–43, 2016.

[39] L A Coogan, A D Saunders, and R N Wilson. Aluminum-in-olivine thermometry of primitive basalts : Evidence of an anomalously hot mantle source for large igneous provinces. *Chemical Geology*, 368:1–10, 2014.

[40] LA Coogan, AD Saunders, and RN Wilson. Aluminum-in-olivine thermometry of primitive basalts: evidence of an anomalously hot mantle source for large igneous provinces. *Chemical Geology*, 368:1–10, 2014.

[41] Alexandre Corgne, Shantanu Keshav, Yingwei Fei, and William F McDonough. How much potassium is in the Earth's core? new insights from partitioning experiments. *Earth and Planetary Science Letters*, 256(3-4):567–576, 2007.

[42] Sarah T Crites and Paul G Lucey. Revised mineral and mg# maps of the moon from integrating results from the lunar prospector neutron and gamma-ray spectrometers with clementine spectroscopy. *American Mineralogist*, 100(4):973–982, 2015.

[43] Natalie M Curran, KH Joy, JF Snape, John F Pernet-Fisher, Jamie D Gilmour, AA Nemchin, Martin J Whitehouse, and Ray Burgess. The early geological history of the moon inferred from ancient lunar meteorite miller range 13317. *Meteoritics & Planetary Science*, 54(7):1401–1430, 2019.

[44] Andrew M Davis. Volatile evolution and loss. *Meteorites and the early solar system II*, 1:295–307, 2006.

[45] Fred A Davis, Munir Humayun, Marc M Hirschmann, and Rupert S Cooper. Experimentally determined mineral/melt partitioning of first-row transition elements (FRTE) during partial melting of peridotite at 3 gpa. *Geochimica et Cosmochimica Acta*, 104:232–260, 2013.

[46] James MD Day and Frederic Moynier. Evaporative fractionation of volatile stable isotopes and their bearing on the origin of the moon. *Philosophical Transactions of the Royal Society A: Mathematical, Physical and Engineering Sciences*, 372(2024):20130259, 2014.

[47] Jan C M De Hoog, Louise Gall, and David H Cornell. Trace-element geochemistry of mantle olivine and application to mantle petrogenesis and geothermobarometry. *Chemical Geology*, 270(1-4):196–215, 2010.

[48] Jan CM De Hoog, Louise Gall, and David H Cornell. Trace-element geochemistry of mantle olivine and application to mantle petrogenesis and geothermobarometry. *Chemical Geology*, 270(1-4):196–215, 2010.

[49] John W Delano. Pristine lunar glasses: Criteria, data, and implications. *Journal of Geophysical Research: Solid Earth*, 91(B4):201–213, 1986.

[50] Tammy Dickinson, GJ Taylor, K Keil, and RW Bild. Germanium abundances in lunar basalts-evidence of mantle metasomatism? In *Lunar and Planetary Science Conference Proceedings*, volume 19, pages 189–198, 1989.

[51] Jennifer L Eigenbrode, Roger E Summons, Andrew Steele, Caroline Freissinet, Maëva Millan, Rafael Navarro-González, Brad Sutter, Amy C McAdam, Heather B Franz, Daniel P Glavin, et al. Organic matter preserved in 3-billion-year-old mudstones at gale crater, mars. *Science*, 360(6393):1096–1101, 2018.

[52] Stephen M Elardo, Matthieu Laneuville, Francis M McCubbin, and Charles K Shearer. Early crust building enhanced on the Moon's nearside by mantle melting-point depression. *Nature Geoscience*, 13(5):339–343, 2020.

[53] Linda T Elkins-Tanton, Seth Burgess, and Qing-Zhu Yin. The lunar magma ocean: Reconciling the solidification process with lunar petrology and geochronology. *Earth and Planetary Science Letters*, 304(3-4):326–336, 2011.

[54] TJ Falloon and DH Green. Anhydrous partial melting of peridotite from 8 to 35 kb and the petrogenesis of MORB. *Journal of Petrology*, (1):379–414, 1988.

[55] Ben Farcy, Ricardo Arevalo, Mazdak Taghioskoui, William McDonough, Mehdi Benna, and William Brinckerhoff. A prospective microwave plasma source for in situ spaceflight applications. *Journal of Analytical and Atomic Spectroscopy*, 2020.

[56] Benjamin Farcy, Ricardo Arevalo, and William McDonough. K/u of the morb source and silicate earth. *Journal of Geophysical Research: Solid Earth*, 2020.

[57] Kenneth A Farley, C Malespin, P Mahaffy, John P Grotzinger, Paulo M Vasconcelos, RE Milliken, M Malin, KS Edgett, Alexander A Pavlov, Joel A Hurowitz, et al. In situ radiometric and exposure age dating of the martian surface. *science*, 343(6169), 2014.

[58] F C Fehsenfeld, K M Evenson, and H P Broida. Microwave Discharge Cavities Operating at 2450 MHz. *Review of Scientific Instruments*, 36(3):294–298, 1964.

[59] Justin Filiberto and Rajdeep Dasgupta. Constraints on the depth and thermal vigor of melting in the Martian mantle. *Journal of Geophysical Research: Planets*, pages 109–122, 2014.

[60] Justin Filiberto, Donald S Musselwhite, Juliane Gross, Katherine Burgess, Loan Le, and Allan H Treiman. Experimental petrology , crystallization history , and parental magma characteristics of olivine-phyric shergottite NWA 1068 : Implications for the petrogenesis of " enriched " olivine-phyric shergottites. 1270(8):1258–1270, 2010.

[61] Justin Filiberto, Donald S Musselwhite, Juliane Gross, Katherine Burgess, Loan Le, and Allan H Treiman. Experimental petrology, crystallization history, and parental magma characteristics of olivine-phyric shergottite NWA 1068: Implications for the petrogenesis of "enriched" olivine-phyric shergottites. *Meteoritics & Planetary Science*, 45(8):1258–1270, 2010.

[62] CN Foley, TE Economou, and RN Clayton. Chemistry of mars pathfinder samples determined by the apxs. *LPI*, page 1979, 2001.

[63] Caroline Freissinet, DP Glavin, Paul R Mahaffy, KE Miller, JL Eigenbrode, RE Summons, AE Brunner, A Buch, Cyril Szopa, PD Archer Jr, et al. Organic molecules in the sheepbed mudstone, gale crater, mars. *Journal of Geophysical Research: Planets*, 120(3):495–514, 2015.

[64] Jeannine Gagnepain-Beyneix, Philippe Lognonné, Hugues Chenet, Denis Lombardi, and Tilman Spohn. A seismic model of the lunar mantle and constraints on temperature and mineralogy. *Physics of the Earth and Planetary Interiors*, 159(3-4):140–166, 2006.

[65] Allison Gale, Colleen A Dalton, Charles H Langmuir, Yongjun Su, and Jean-Guy Schilling. The mean composition of ocean ridge basalts. *Geochemistry, Geophysics, Geosystems*, 14(3):489–518, 2013.

[66] Shan Gao, Ting-Chuan Luo, Ben-Ren Zhang, Hong-Fei Zhang, Yin-wen Han, Zi-Dan Zhao, and Yi-Ken Hu. Chemical composition of the continental crust as revealed by studies in East China. *Geochimica et Cosmochimica Acta*, 62(11):1959–1975, 1998.

[67] Ian Garrick-Bethell, Francis Nimmo, and Mark A Wieczorek. Structure and formation of the lunar farside highlands. *Science*, 330(6006):949–951, 2010.

[68] Jeffrey J Gillis, Bradley L Jolliff, and Randy L Korotev. Lunar surface geochemistry: Global concentrations of Th, K, and FeO as derived from lunar prospector and clementine data. *Geochimica et Cosmochimica Acta*, 68(18):3791–3805, 2004.

[69] Fred Goesmann, William B Brinckerhoff, François Raulin, Walter Goetz, Ryan M Danell, Stephanie A Getty, Sandra Siljeström, Helge Mißbach, Harald Steininger, Ricardo D Arevalo Jr, et al. The Mars Organic Molecule Analyzer (MOMA) instrument: characterization of organic material in martian sediments. *Astrobiology*, 17(6-7):655–685, 2017.

[70] C Gorse, S De Benedictis, G Dilecce, and M Capitelli. Electron energy distribution functions in he/n2 mixtures in the presence of metastable states. *Spectrochimica Acta Part B: Atomic Spectroscopy*, 45(4-5):521–525, 1990.

[71] Valentine Grimaudo, Pavel Moreno-García, Andreas Riedo, Maike B Neuland, Marek Tulej, Peter Broekmann, and Peter Wurz. High-resolution chemical depth profiling of solid material using a miniature laser ablation/ionization mass spectrometer. *Analytical chemistry*, 87(4):2037–2041, 2015.

[72] Marco Grotti, Cristina Lagomarsino, and Jean Michel Mermet. Effect of operating conditions on excitation temperature and electron number density in axially-viewed ICP-OES with introduction of vapours or aerosols w. *Journal of analytical atomic spectroscopy*, 21(9):963–969, 2006.

[73] Andrey A Gurenko, Alexander V Sobolev, Kaj A Hoernle, Folkmar Hauff, and Hans-Ulrich Schmincke. Enriched, himu-type peridotite and depleted recycled pyroxenite in the Canary plume: a mixed-up mantle. *Earth and Planetary Science Letters*, 277(3-4):514–524, 2009.

[74] Justin J Hagerty, Charles K Shearer, and David T Vaniman. Heat-producing elements in the lunar mantle: Insights from ion microprobe analyses of lunar pyroclastic glasses. *Geochimica et cosmochimica acta*, 70(13):3457–3476, 2006.

[75] Daniel Halwidl. *Development of an effusive molecular beam apparatus*. Springer, 2016.

[76] Jason D Harper, Nicholas A Charipar, Christopher C Mulligan, Xinrong Zhang, R Graham Cooks, and Zheng Ouyang. Low-temperature plasma probe for ambient desorption ionization. *Analytical chemistry*, 80(23):9097–9104, 2008.

[77] Erik H Hauri, Thomas P Wagner, and Timothy L Grove. Experimental and natural partitioning of Th, U, Pb and other trace elements between garnet, clinopyroxene and basaltic melts. *Chemical Geology*, 117(1-4):149–166, 1994.

[78] Detao He, Cin-Ty A Lee, Xun Yu, and Michael Farner. Ge/Si partitioning in igneous systems: Constraints from laser ablation ICP-MS measurements on natural samples. *Geochemistry, Geophysics, Geosystems*, 20(10):4472–4486, 2019.

[79] James W Head and Lionel Wilson. Lunar mare volcanism: Stratigraphy, eruption conditions, and the evolution of secondary crusts. *Geochimica et Cosmochimica Acta*, 56(6):2155–2175, 1992.

[80] C Herzberg and P D Asimow. PRIMELT3 MEGA.XLSM software for primary magma calculation: Peridotite primary magma MgO contents from the liquidus to the solidus. *Geochemistry, Geophysics, Geosystems*, pages 563–578, 2015.

[81] C Herzberg and M J O Hara. Plume-Associated Ultramafic Magmas of Phanerozoic Age. *Journal of Petrology*, 43(10):1857–1883, 2002.

[82] Claude Herzberg and PD Asimow. PRIMELT 3 MEGA. XLSM software for primary magma calculation: peridotite primary magma MgO contents from the liquidus to the solidus. *Geochemistry, Geophysics, Geosystems*, 16(2):563–578, 2015.

[83] Marc M Hirschmann and Edward M Stolper. A possible role for garnet pyroxenite in the origin of the "garnet signature" in MORB. *Contributions to Mineralogy and Petrology*, 124(2):185–208, 1996.

[84] A W Hofmann. Sampling mantle heterogeneity through oceanic basalts: Isotopes and trace elements. In Richard W Carlson, editor, *The Mantle and Core*, volume 3 of *Treatise on Geochemistry (Second Edition)* of *Treatise on Geochemistry (Second Edition)*, chapter 3, pages 67–101. Elsevier, Oxford, 2014. Editors-in-chief H. D. Holland and K. K. Turekian.

[85] Albrecht W Hofmann, KP Jochum, M Seufert, and William M White. Nb and Pb in oceanic basalts: new constraints on mantle evolution. *Earth and Planetary science letters*, 79(1-2):33–45, 1986.

[86] Albrecht W Hofmann and William M White. Mantle plumes from ancient oceanic crust. *Earth and Planetary Science Letters*, 57(2):421–436, 1982.

[87] Anne Horne, Ulf Litzén, and Sveneric Johansson. *Spectrophysics: principles and applications*. Springer Science & Business Media, 1999.

[88] Alan R Hoskinson, Jeffrey Hopwood, Neil W Bostrom, Jeffrey A Crank, and Christopher Harrison. Low-power microwave-generated helium microplasma for molecular and atomic spectrometry. *Journal of Analytical Atomic Spectrometry*, 26(6):1258–1264, 2011.

[89] R S Houk. Elemental and Isotopic Analysis by Inductively Coupled Plasma Mass Spectrometry. *Accounts of Chemical Research*, 27(11):333–339, 1994.

[90] Yu Huang, Viacheslav Chubakov, Fabio Mantovani, Roberta L Rudnick, and William F McDonough. A reference Earth model for the heat-producing elements and associated geoneutrino flux. *Geochemistry, Geophysics, Geosystems*, 14(6):2003–2029, 2013.

[91] Debra M Hurwitz and David A Kring. Differentiation of the South Pole–Aitken basin impact melt sheet: Implications for lunar exploration. *Journal of Geophysical Research: Planets*, 119(6):1110–1133, 2014.

[92] I H Hutchinson. Principles of Plasma Diagnosis. *Plasma Physics and Controlled Fusion*, 44(2603):2603, 2002.

[93] Yoshiaki Ishihara, Sander Goossens, Koji Matsumoto, Hirotomo Noda, Hiroshi Araki, Noriyuki Namiki, Hideo Hanada, Takahiro Iwata, Seiichi Tazawa, and Sho Sasaki. Crustal thickness of the Moon: Implications for farside basin structures. *Geophysical Research Letters*, 36(19), 2009.

[94] Frances E Jenner and Hugh St C O'Neill. Analysis of 60 elements in 616 ocean floor basaltic glasses. *Geochemistry, Geophysics, Geosystems*, 13(2), 2012.

[95] KP Jochum, AW Hofmann, E Ito, H Mi Seufert, and WM White. K, U and Th in mid-ocean ridge basalt glasses and heat production, K/U and K/Rb in the mantle. *Nature*, 306(5942):431–436, 1983.

[96] Bradley L Jolliff, Jeffrey J Gillis, Larry A Haskin, Randy L Korotev, and Mark A Wieczorek. Major lunar crustal terranes: Surface expressions and crust-mantle origins. *Journal of Geophysical Research: Planets*, 105(E2):4197–4216, 2000.

[97] John H Jones and Herbert Palme. Geochemical constraints on the origin of the earth and moon. *Origin of the Earth and Moon*, 30:197, 2000.

[98] William M Kaula, Gerald Schubert, Richard E Lingenfelter, WL Sjogren, and WR Wollenhaupt. Apollo laser altimetry and inferences as to lunar structure. In *Lunar and Planetary Science Conference Proceedings*, volume 5, pages 3049–3058, 1974.

[99] Goestar Klingelhöfer, J Brückner, C D'uston, R Gellert, and R Rieder. The rosetta alpha particle x-ray spectrometer (apxs). *Space science reviews*, 128(1-4):383–396, 2007.

[100] Randy L Korotev. Lunar geochemistry as told by lunar meteorites. *Chemie der Erde*, 65(4):297–346, 2005.

[101] A. Kramida, Yu. Ralchenko, and J. Reader. NIST Atomic Spectra Database (version 5.6.1), 2018.

[102] OL Kuskov and VA Kronrod. Constitution of the moon: 5. constraints on composition, density, temperature, and radius of a core. *Physics of the Earth and Planetary Interiors*, 107(4):285–306, 1998.

[103] M Laneuville, J Taylor, and M Wieczorek. Distribution of radioactive heat sources and thermal history of the Moon. *Journal of Geophysical Research: Planets*, 123(12):3144–3166, 2018.

[104] Matthieu Laneuville, MA Wieczorek, Doris Breuer, and Nicola Tosi. Asymmetric thermal evolution of the moon. *Journal of Geophysical Research: Planets*, 118(7):1435–1452, 2013.

[105] Thomas J Lapen, Minako Righter, Rasmus Andreasen, Anthony J Irving, Aaron M Satkoski, Brian L Beard, Kunihiko Nishiizumi, A J Timothy Jull, and Marc W Caffee. Two billion years of magmatism recorded from a single Mars meteorite ejection site. *Science Advances*, 3(2):1–7, 2017.

[106] Lenox Laser. Fluid flow through small calibrated orifices, 2015.

[107] John C Lassiter. Role of recycled oceanic crust in the potassium and argon budget of the Earth: Toward a resolution of the "missing argon" problem. *Geochemistry, Geophysics, Geosystems*, 5(11), 2004.

[108] B Le Neindre, Y Garrabos, and R Tufeu. Thermal conductivity of dense noble gases. *Physica A: Statistical Mechanics and its Applications*, 156(1):512–521, 1989.

[109] V Le Roux, R Dasgupta, and C-TA Lee. Mineralogical heterogeneities in the earth's mantle: Constraints from mn, co, ni and zn partitioning during partial melting. *Earth and Planetary Science Letters*, 307(3-4):395–408, 2011.

[110] LA Leshin, PR Mahaffy, CR Webster, Michel Cabane, Patrice Coll, PG Conrad, PD Archer, SK Atreya, AE Brunner, A Buch, et al. Volatile, isotope, and organic analysis of martian fines with the mars curiosity rover. *Science*, 341(6153):1238937, 2013.

[111] K N Leung, S Walther, and H W Owren. A compact microwave ion source. *IEEE Transactions on Nuclear Science*, 32(5):1803–1805, 1985.

[112] G Livadiotis. Collision frequency and mean free path for plasmas described by kappa distributions. *AIP Advances*, 9(10):105307, 2019.

[113] R Gordon Livesey. Flow of gases through tubes and orifices, 1998.

[114] Katharina Lodders. Solar system abundances and condensation temperatures of the elements. *The Astrophysical Journal*, 591(2):1220, 2003.

[115] Katharina Lodders. Solar elemental abundances. *arXiv preprint arXiv:1912.00844*, 2019.

[116] Henry P Longerich, Simon E Jackson, and Detlef Günther. Inter-laboratory note. laser ablation inductively coupled plasma mass spectrometric transient signal data acquisition and analyte concentration calculation. *Journal of analytical atomic spectrometry*, 11(9):899–904, 1996.

[117] J Longhi. Liquidus equilibria of lunar analogs at high pressure. In *Lunar and Planetary Science Conference*, volume 24, 1993.

[118] J Longhi. Liquidus equilibria of some primary lunar and terrestrial melts in the garnet stability field. *Geochimica et Cosmochimica Acta*, 59(11):2375–2386, 1995.

[119] J Longhi. Petrogenesis of picritic mare magmas: constraints on the extent of early lunar differentiation. *Geochimica et Cosmochimica Acta*, 70(24):5919–5934, 2006.

[120] John Longhi. Experimental petrology and petrogenesis of mare volcanics. *Geochimica et Cosmochimica Acta*, 56(6):2235–2251, 1992.

[121] John Longhi, Sedelia R Durand, and David Walker. The pattern of ni and co abundances in lunar olivines. *Geochimica et Cosmochimica Acta*, 74(2):784–798, 2010.

[122] Tanya Lyubetskaya and Jun Korenaga. Chemical composition of Earth's primitive mantle and its variance: 1. method and results. *Journal of Geophysical Research: Solid Earth*, 112(B3), 2007.

[123] Paul R Mahaffy, Christopher R Webster, Michel Cabane, Pamela G Conrad, Patrice Coll, Sushil K Atreya, Robert Arvey, Michael Barciniak, Mehdi Benna, Lora Bleacher, et al. The sample analysis at Mars investigation and instrument suite. *Space Science Reviews*, 170(1-4):401–478, 2012.

[124] PR Mahaffy and K Lai. An electrostatic quadrupole deflector for mass spectrometer applications. *Journal of Vacuum Science & Technology A: Vacuum, Surfaces, and Films*, 8(4):3244–3246, 1990.

[125] Alessandro Maltese and Klaus Mezger. The pb isotope evolution of bulk silicate earth: Constraints from its accretion and early differentiation history. *Geochimica et cosmochimica acta*, 271:179–193, 2020.

[126] Sandra Martinez-Jarquin and Robert Winkler. Low-temperature plasma (ltp) jets for mass spectrometry (ms): Ion processes, instrumental set-ups, and application examples. *TrAC Trends in Analytical Chemistry*, 89:133–145, 2017.

[127] Andrew K Matzen, Bernard J Wood, Michael B Baker, and Edward M Stolper. The roles of pyroxenite and peridotite in the mantle sources of oceanic basalts. *Nature Geoscience*, 10(7):530–535, 2017.

[128] M Maurice, N Tosi, S Schwinger, D Breuer, and T Kleine. A long-lived magma ocean on a young moon. *Science advances*, 6(28):eaba8949, 2020.

[129] W F McDonough and S S Sun. The composition of the Earth. *Chemical Geology*, 120(3-4):223–253, 1995.

[130] William F McDonough and S-S Sun. The composition of the earth. *Chemical geology*, 120(3-4):223–253, 1995.

[131] DAN Mckenzie and MJ Bickle. The volume and composition of melt generated by extension of the lithosphere. *Journal of petrology*, 29(3):625–679, 1988.

[132] Robert L Merlino. Understanding Langmuir probe current-voltage characteristics. *American Journal of Physics*, 75(12):1078–1085, 2007.

[133] Akbar Montaser. *Inductively coupled plasma mass spectrometry*. John Wiley & Sons, 1998.

[134] Raffaella Montelli, G Nolet, F A Dahlen, and G Masters. A catalogue of deep mantle plumes: New results from finite- frequency tomography. *Geochemistry, Geophysics, Geosystems*, (January), 2006.

[135] John W. Morgan. Convection Plumes in the Lower Mantle. *Nature*, 230:42–43, 1971.

[136] John W Morgan, Jan Hertogen, and Edward Anders. The Moon: Composition determined by nebular processes. *The moon and the planets*, 18(4):465–478, 1978.

[137] DP Moriarty III and CM Pieters. The character of South Pole-Aitken basin: patterns of surface and subsurface composition. *Journal of Geophysical Research: Planets*, 123(3):729–747, 2018.

[138] Na Na, Yu Xia, Zhenli Zhu, Xinrong Zhang, and R Graham Cooks. Birch reduction of benzene in a low-temperature plasma. *Angewandte Chemie International Edition*, 48(11):2017–2019, 2009.

[139] M Y Naz, A Ghaffar, N U Rehman, S Naseer, and M Zakaullah. Double and triple Langmuir probe measurements in inductively coupled nitrogen plasma. *Progress in Electromagnetic Research*, 114:113–128, 2011.

[140] Clive R Neal. Interior of the Moon: The presence of garnet in the primitive deep lunar mantle. *Journal of Geophysical Research: Planets*, 106(E11):27865–27885, 2001.

[141] H Nekvasil, A Dondolini, J Horn, J Filiberto, H Long, and D H Lindsley. The Origin and Evolution of Silica-saturated Alkalic Suites : an Experimental Study. *Journal of Petrology*, 45(4):693–721, 2004.

[142] H Nekvasil, A Dondolini, J Horn, J Filiberto, H Long, and DH Lindsley. The origin and evolution of silica-saturated alkalic suites: an experimental study. *Journal of Petrology*, 45(4):693–721, 2004.

[143] Hanna Nekvasil, Justin Filiberto, Francis M M C Cubbin, and Donald H Lindsley. Alkalic parental magmas for chassignites ? 992(6):979–992, 2007.

[144] Hanna Nekvasil, Justin Filiberto, Francis M McCubbin, and Donald H Lindsley. Alkalic parental magmas for chassignites? *Meteoritics & Planetary Science*, 42(6):979–992, 2007.

[145] Alexander Nemchin, N Timms, Robert Pidgeon, T Geisler, Steven Reddy, and C Meyer. Timing of crystallization of the lunar magma ocean constrained by the oldest zircon. *Nature Geoscience*, 2(2):133–136, 2009.

[146] Maike Brigitte Neuland, Stefan Meyer, Klaus Mezger, Andreas Riedo, Marek Tulej, and Peter Wurz. Probing the allende meteorite with a miniature laser-ablation mass analyser for space application. *Planetary and space science*, 101:196–209, 2014.

[147] Hongsen Niu and R S Houk. Fundamental aspects of ion extraction in inductively coupled plasma mass spectrometry. *Spectrochemica Acta*, 51:779–815, 1996.

[148] Hongsen Niu and RS Houk. Fundamental aspects of ion extraction in inductively coupled plasma mass spectrometry. *Spectrochimica Acta Part B: Atomic Spectroscopy*, 51(8):779–815, 1996.

[149] Makiko Ohtake, Tsuneo Matsunaga, Junichi Haruyama, Yasuhiro Yokota, Tomokatsu Morota, Chikatoshi Honda, Yoshiko Ogawa, Masaya Torii, Hideaki Miyamoto, Tomoko Arai, et al. The global distribution of pure anorthosite on the moon. *Nature*, 461(7261):236–240, 2009.

[150] Makiko Ohtake, Hiroshi Takeda, Tsuneo Matsunaga, Yasuhiro Yokota, Junichi Haruyama, Tomokatsu Morota, Satoru Yamamoto, Yoshiko Ogawa, Takahiro Hiroi, Yuzuru Karouji, et al. Asymmetric crustal growth on the Moon indicated by primitive farside highland materials. *Nature Geoscience*, 5(6):384–388, 2012.

[151] Patricia J Ohtake, Marcilene Lazarus, Rebecca Schillo, and Michael Rosen. Simulation experience enhances physical therapist student confidence in managing a patient in the critical care environment. *Physical therapy*, 93(2):216–228, 2013.

[152] Hugh St C O'Neill, Andrew J Berry, and Guilherme Mallmann. The oxidation state of iron in Mid-Ocean Ridge Basaltic (MORB) glasses: Implications for their petrogenesis and oxygen fugacities. *Earth and Planetary Science Letters*, 504:152–162, 2018.

[153] Hugh St C O'Neill and Frances E Jenner. The global pattern of trace-element distributions in ocean floor basalts. *Nature*, 491(7426):698–704, 2012.

[154] Hugh St C O'Neill and Frances E Jenner. Causes of the compositional variability among ocean floor basalts. *Journal of Petrology*, 57(11-12):2163–2194, 2016.

[155] Herbert Palme and H St C O'Neill. Cosmochemical estimates of mantle composition. In Richard W Carlson, editor, *The Mantle and Core*, volume 3 of *Treatise on Geochemistry (Second Edition)* of *Treatise on Geochemistry (Second Edition)*, page 568. Elsevier, Oxford, 2014. Editors-in-chief H. D. Holland and K. K. Turekian.

[156] James H Patterson, Ernest J Franzgrote, Anthony L Turkevich, Wayne A Anderson, Thanasis E Economou, Harry E Griffin, Stanley L Grotch, and Kenneth P Sowinski. Alpha-scattering experiment on surveyor 7: Comparison with surveyors 5 and 6. *Journal of Geophysical Research*, 74(25):6120–6148, 1969.

[157] Patrick N Peplowski, Larry G Evans, Steven A Hauck, Timothy J McCoy, William V Boynton, Jeffery J Gillis-Davis, Denton S Ebel, John O Goldsten, David K Hamara, David J Lawrence, et al. Radioactive elements on Mercury's surface from MESSENGER: Implications for the planet's formation and evolution. *Science*, 333(6051):1850–1852, 2011.

[158] Carle M Pieters, Joseph Boardman, Bonnie Buratti, Alok Chatterjee, Roger Clark, Tom Glavich, Robert Green, James Head III, Peter Isaacson, Erick Malaret, et al. The moon mineralogy mapper (m^3) on chandrayaan-1. *Current Science*, pages 500–505, 2009.

[159] Thomas H Prettyman, William C Feldman, Frank P Ameduri, Bruce L Barraclough, Ethan W Cascio, Kenneth R Fuller, Herbert O Funsten, David J Lawrence, Gregg W McKinney, Christopher T Russell, et al. Gamma-ray and neutron spectrometer for the dawn mission to 1 ceres and 4 vesta. *IEEE Transactions on Nuclear Science*, 50(4):1190–1197, 2003.

[160] Thomas H Prettyman, JJ Hagerty, RC Elphic, WC Feldman, DJ Lawrence, GW McKinney, and DT Vaniman. Elemental composition of the lunar surface: Analysis of gamma ray spectroscopy data from lunar prospector. *Journal of Geophysical Research: Planets*, 111(E12), 2006.

[161] K Putirka. Melting depths and mantle heterogeneity beneath Hawaii and the East Pacific Rise: Constraints from Na/Ti and rare earth element ratios. *Journal of Geophysical Research: Solid Earth*, 104(B2):2817–2829, 1999.

[162] K Putirka, Michael Perfit, FJ Ryerson, and Matthew G Jackson. Ambient and excess mantle temperatures, olivine thermometry, and active vs. passive upwelling. *Chemical Geology*, 241(3-4):177–206, 2007.

[163] Keith Putirka. Excess temperatures at ocean islands : Implications for mantle layering and convection. (4):283–286, 2008.

[164] Lucy V Ratcliffe, Frank JM Rutten, David A Barrett, Terry Whitmore, David Seymour, Claire Greenwood, Yolanda Aranda-Gonzalvo, Steven Robinson, and Martin McCoustra. Surface analysis under ambient conditions using plasma-assisted desorption/ionization mass spectrometry. *Analytical chemistry*, 79(16):6094–6101, 2007.

[165] R Rejoub, BG Lindsay, and RF Stebbings. Determination of the absolute partial and total cross sections for electron-impact ionization of the rare gases. *Physical Review A*, 65(4):042713, 2002.

[166] R Rieder, R Gellert, J Brückner, G Klingelhöfer, G Dreibus, A Yen, and SW Squyres. The new athena alpha particle x-ray spectrometer for the mars exploration rovers. *Journal of Geophysical Research: Planets*, 108(E12), 2003.

[167] P. L. Roeder and R. F. Emslie. Olivine-Liquid Equilibrium. 29:275–289, 1970.

[168] PL Roeder and RFl Emslie. Olivine-liquid equilibrium. *Contributions to mineralogy and petrology*, 29(4):275–289, 1970.

[169] R. L. Rudnick and S. Gao. Composition of the continental crust. In R. L. Rudnick, editor, *The Crust*, volume 4 of *Treatise on Geochemistry (Second Edition)*, pages 1–51. Elsevier, Oxford, 2014. Editors-in-chief H. D. Holland and K. K. Turekian.

[170] RL Rudnick and S Gao. The crust. treatise on geochemistry. *Treatise on geochemistry*, 3:1–64, 2003.

[171] A Salaün, B Villemant, M P Semet, and T Staudacher. Cannibalism of olivine-rich cumulate xenoliths during the 1998 eruption of Piton de la Fournaise (La Réunion hotspot): Implications for the generation of magma diversity. *Journal of Volcanology and Geothermal Research*, 198(1-2):187–204, 2010.

[172] Vincent JM Salters, John E Longhi, and M Bizimis. Near mantle solidus trace element partitioning at pressures up to 3.4 GPa. *Geochemistry, Geophysics, Geosystems*, 3(7):1–23, 2002.

[173] Charles K Shearer and JJ Papike. Early crustal building processes on the moon: Models for the petrogenesis of the magnesian suite. *Geochimica et Cosmochimica Acta*, 69(13):3445–3461, 2005.

[174] CK Shearer, PC Hess, MA Wieczorek, ME Pritchard, EM Parmentier, LE Borg, J Longhi, LT Elkins-Tanton, CR Neal, and I Antonenko. New views of the Moon. *Rev. Mineral. Geochem*, 60:365–518, 2006.

[175] DN Shirley and JT Wasson. Mechanism for the extrusion of kreep. In *Lunar and Planetary Science Conference Proceedings*, volume 12, pages 965–978, 1982.

[176] Kenneth WW Sims and Donald J DePaolo. Inferences about mantle magma sources from incompatible element concentration ratios in oceanic basalts. *Geochimica et Cosmochimica Acta*, 61(4):765–784, 1997.

[177] Alexander V Sobolev, Albrecht W Hofmann, Stephan V Sobolev, and Igor K Nikogosian. An olivine-free mantle source of hawaiian shield basalts. *Nature*, 434(7033):590–597, 2005.

[178] Dave R Stegman, A Mark Jellinek, Stephen A Zatman, John R Baumgardner, and Mark A Richards. An early lunar core dynamo driven by thermochemical mantle convection. *Nature*, 421(6919):143–146, 2003.

[179] Andreas Stracke, Felix Genske, Jasper Berndt, and Janne M Koornneef. Ubiquitous ultra-depleted domains in Earth's mantle. *Nature Geoscience*, 12(10):851–855, 2019.

[180] S-S Sun and William F McDonough. Chemical and isotopic systematics of oceanic basalts: implications for mantle composition and processes. *Geological Society, London, Special Publications*, 42(1):313–345, 1989.

[181] Yong-ik Sung, H B Lim, and R S Houk. Diagnostic studies of a low-pressure inductively coupled plasma in argon using a double Langmuir probe. *Journal of analytical atomic spectroscopy*, 17:565–569, 2002.

[182] Yu A Surkov, VL Barsukov, LP Moskalyeva, VP Kharyukova, and AL Kemurdzhian. New data on the composition, structure, and properties of venus rock obtained by Venera 13 and Venera 14. *Journal of Geophysical Research: Solid Earth*, 89(S02):B393–B402, 1984.

[183] Mazdak Taghioskoui and Mona Zaghloul. Plasma ionization under simulated ambient Mars conditions for quantification of methane by mass spectrometry. *The Analyst*, 141(7):2270–2277, 2016.

[184] Mitsunobu Tatsumoto, Roy J Knight, and Claude J Allegre. Time differences in the formation of meteorites as determined from the ratio of lead-207 to lead-206. *Science*, 180(4092):1279–1283, 1973.

[185] Mitsunobu Tatsumoto, Wayne R Premo, and Daniel M Unruh. Origin of lead from green glass of apollo 15426: A search for primitive lunar lead. *Journal of Geophysical Research: Solid Earth*, 92(B4):E361–E371, 1987.

[186] Jeffrey Taylor and Mark Wieczorek. Lunar bulk chemical composition: a post-Gravity Recovery and Interior Laboratory reassessment. *Philosophical Transactions of the Royal Society A: Mathematical, Physical and Engineering Sciences*, 372(2024):20130242, 2014.

[187] R Taylor. *Planetary science: A lunar perspective*, volume 3303. Lunar and Planetary Institute Houston, 1982.

[188] Ross Taylor, Jeffrey Taylor, and August Taylor. The moon: a Taylor perspective. *Geochimica et Cosmochimica Acta*, 70(24):5904–5918, 2006.

[189] SR Taylor. Abundance of chemical elements in the continental crust: a new table. *Geochimica et cosmochimica acta*, 28(8):1273–1285, 1964.

[190] SR Taylor. The moon in encyclopedia of the solar system, ed. by pr weissman, l.-a. mcfadden, and tv johnson, 1999.

[191] Kevin G Thaisen, James W Head, Lawrence A Taylor, Georgiana Y Kramer, Peter Isaacson, Jeff Nettles, Noah Petro, and Carle M Pieters. Geology of the Moscoviense basin. *Journal of Geophysical Research: Planets*, 116(E6), 2011.

[192] Maxwell M Thiemens, Peter Sprung, Raúl OC Fonseca, Felipe P Leitzke, and Carsten Münker. Early moon formation inferred from hafnium–tungsten systematics. *Nature Geoscience*, 12(9):696–700, 2019.

[193] K Tokiguchi, N Sakudo, and H Koike. Energy analysis of microwave ion sources. *Journal of Vacuum Science and Technology A*, 2(1):29–34, 1984.

[194] Allan H Treiman, Justin Filiberto, and Edgard G Rivera-Valentín. How good is "good enough?" major element chemical analyses of planetary basalts by spacecraft instruments. *The Planetary Science Journal*, 1(3):65, 2020.

[195] Jarek Trela, Esteban Gazel, Alexander V Sobolev, Lowell Moore, Michael Bizimis, Brian Jicha, and Valentina G Batanova. The hottest lavas of the Phanerozoic and the survival of deep Archaean reservoirs. *Nature Geoscience*, 10(June), 2017.

[196] KK Turekian. The terrestrial economy of helium and argon. *Geochimica et Cosmochimica Acta*, 17(1-2):37–43, 1959.

[197] J Uebbing, A Ciocan, and K Niemax. Optical emission spectrometry of a microwave induced plasma used with laser ablation of solid samples. *Spectrochimica Acta Part B: Atomic Spectroscopy*, 47(5):601–610, 1992.

[198] Harold C Urey. The cosmic abundances of potassium, uranium, and thorium and the heat balances of the Earth, the Moon, and Mars. *Proceedings of the National Academy of Sciences of the United States of America*, 41(3):127, 1955.

[199] Zhihuan Wan, Laurence Coogan, and Dante Canil. Experimental calibration of aluminum partitioning between olivine and spinel as a Geothermometer Experimental calibration of aluminum partitioning between olivine and spinel as a geothermometer. *American Mineralogist*, (March), 2008.

[200] Zhihuan Wan, Laurence A Coogan, and Dante Canil. Experimental calibration of aluminum partitioning between olivine and spinel as a geothermometer. *American Mineralogist*, 93(7):1142–1147, 2008.

[201] Zhengrong Wang and Glenn A Gaetani. Partitioning of Ni between olivine and siliceous eclogite partial melt: experimental constraints on the mantle source of hawaiian basalts. *Contributions to Mineralogy and Petrology*, 156(5):661–678, 2008.

[202] H Wänke and G Dreibus. Chemical and isotopic evidence for the early history of the earth-moon system. In *Tidal friction and the Earth's rotation II*, pages 322–344. Springer, 1982.

[203] Paul H Warren. "new" lunar meteorites: Implications for composition of the global lunar surface, lunar crust, and the bulk moon. *Meteoritics & Planetary Science*, 40(3):477–506, 2005.

[204] PH Warren and GJ Taylor. The Moon. 1 of *Treatise on Geochemistry (Second Edition)*:559–599, 2014. Editors-in-chief H. D. Holland and K. K. Turekian.

[205] GJ Wasserburg, Gordon JF MacDonald, Fred Hoyle, and William A Fowler. Relative contributions of uranium, thorium, and potassium to heat production in the Earth. *Science*, 143(3605):465–467, 1964.

[206] Mark A Wieczorek, Bradley L Jolliff, Amir Khan, Matthew E Pritchard, Benjamin P Weiss, James G Williams, Lon L Hood, Kevin Righter, Clive R Neal, Charles K Shearer, et al. The constitution and structure of the lunar interior. *Reviews in mineralogy and geochemistry*, 60(1):221–364, 2006.

[207] Mark A Wieczorek, Gregory A Neumann, Francis Nimmo, Walter S Kiefer, G Jeffrey Taylor, H Jay Melosh, Roger J Phillips, Sean C Solomon, Jeffrey C Andrews-Hanna, Sami W Asmar, et al. The crust of the Moon as seen by GRAIL. *Science*, 339(6120):671–675, 2013.

[208] RC Wiens, S Maurice, J Lasue, O Forni, RB Anderson, S Clegg, S Bender, D Blaney, BL Barraclough, A Cousin, et al. Pre-flight calibration and initial data processing for the ChemCam laser-induced breakdown spectroscopy instrument on the Mars Science Laboratory rover. *Spectrochimica Acta Part B: Atomic Spectroscopy*, 82:1–27, 2013.

[209] RC Wiens, R Newell, S Clegg, SK Sharma, A Misra, P Bernardi, S Maurice, K McCabe, and Ph Cais. The supercam remote raman spectrometer for mars 2020. In *Proceedings of the 48th Lunar and Planetary Science Conference (LPSC XLVIII)*, 2017.

[210] Roger C Wiens, Sylvestre Maurice, Bruce Barraclough, Muriel Saccoccio, Walter C Barkley, James F Bell, Steve Bender, John Bernardin, Diana Blaney, Jennifer Blank, et al. The chemcam instrument suite on the mars science laboratory (msl) rover: Body unit and combined system tests. *Space science reviews*, 170(1-4):167–227, 2012.

[211] Lionel Wilson and James W Head. Ascent and eruption of basaltic magma on the Earth and Moon. *Journal of Geophysical Research: Solid Earth*, 86(B4):2971–3001, 1981.

[212] Rainer Wolf and Edward Anders. Moon and earth: compositional differences inferred from siderophiles, volatiles, and alkalis in basalts. *Geochimica et Cosmochimica Acta*, 44(12):2111–2124, 1980.

[213] Rhea K Workman and Stanley R Hart. Major and trace element composition of the depleted MORB mantle (DMM). *Earth and Planetary Science Letters*, 231(1-2):53–72, 2005.

[214] Shuying Yang, Munir Humayun, and Vincent JM Salters. Elemental constraints on the amount of recycled crust in the generation of mid-oceanic ridge basalts (MORBs). *Science advances*, 6(26):eaba2923, 2020.

[215] Meng-Hua Zhu, Tao Ma, Jin Chang, ZeSheng Tang, Wing-Huen Ip, and AoAo Xu. Lunar potassium distribution: Results from Chang'E-1 gamma ray spectrometer. *Science China Physics, Mechanics and Astronomy*, 54(11):2083, 2011.

[216] Alan Zindler and Stan Hart. Chemical geodynamics. *Annual review of earth and planetary sciences*, 14(1):493–571, 1986.